Engineered Proteins for Studying and Controlling Cellular Recognition

A DISSERTATION
SUBMITTED TO THE FACULTY OF THE
UNIVERSITY OF MINNESOTA
BY

Clifford Michael Csizmar

IN PARTIAL FULFILLMENT OF THE REQUIREMENTS
FOR THE DEGREE OF
DOCTOR OF PHILOSOPHY

Advisor: Carston R. Wagner, Ph.D.

August 2018

ACKNOWLEDGEMENTS

There are many people I need to thank for helping me reach this stage in my career. Foremost, I thank my advisor, Rick Wagner, for his constant support of my work and goals over the past several years. He provided me with the tools, both physical and abstract, necessary to pursue my graduate studies. Rick consistently pushed me to expand my skillset and knowledgebase, showed patience with my many mistakes and shortcomings, and challenged me to think openly and critically. Not only has his tutelage fostered my scientific development, but it will also serve as the foundation for my continued career in science and academia.

I am also immensely grateful to Ben Hackel for playing a highly active role in my training. He integrated me into his lab, co-sponsored my pre-doctoral fellowship, and supported my foray into engineering, all without hesitation. Ben has an infectious enthusiasm for discovery, and I thoroughly enjoyed our engaging and motivating conversations. Likewise, thank you to Dan Harki and Courtney Aldrich for their longitudinal mentorship throughout my tenure in the Department of Medicinal Chemistry. Both exhibited a vested interest in my development as a physician scientist, providing an abundance of education, encouragement, support, and critiques that were instrumental in my learning.

Also instrumental was the support of my colleagues. We learned from each other, trading ideas and skills. We commiserated in our frustration and failures, and celebrated our milestones and accomplishments. Perhaps most importantly, we shared libations, never too few and only rarely too many. So, thank you to Jacob Petersburg, Trent West, Lakmal Rozumalski, Sid Kumarapperuma, Alex Strom, TJ Perry, Larry Stern, Danny Woldring, Brett Case, Max Kruziki, Kellen Passow, John Widen, Joe Buonomo, and the numerous others who contributed to this experience.

I thank my undergraduate advisor, Don Warner (Boise State University), for instilling in me a passion for research and education. In many ways, Don's mentorship was the most influential factor in my decision to pursue MD/PhD training, and I am forever grateful for his guidance and friendship. I also thank the late Jeff Peloquin (Boise State University) for recruiting me into my very first research experience all those years ago.

The Medical Scientist Training Program has provided me with incredible opportunities. I'm especially grateful to Yoji Shimizu, Bryce Binstadt, and Peter Bitterman for their direction, advice, and advocacy during my path through the program. I also thank Susan Shurson and Nick Berg, without whom the dual degree training would not be possible. I offer a special thank you to Zohar Sachs for her clinical and academic mentorship, and for solidifying my career interests in hematology. She is a compassionate physician and a brilliant scientist, and I am fortunate to have her as a role model. Thank you to all of my colleagues in the MSTP; especially to Balvindar Singh, for helping me trade toiling at the desk for suffering in the saddle whenever I needed perspective.

Finally, I thank my parents, Caren Bays and Mike Csizmar, for their unyielding support and encouragement throughout my life. Furthermore, I cannot fully express my gratitude for my wife, Jennilee Csizmar, for she makes me into a better person every day. And to Sofie and Ranger, you are the most needy and wonderful dogs I could have asked for.

It would not have been possible to pursue or complete this work without the assistance of these individuals and groups, all of whom have my sincerest gratitude.

DEDICATION

To my wife, Jennilee, for your overflowing support, joy, energy, and love. Inside and out, you are truly beautiful (I only say that word for you).

ABSTRACT

The ability to direct cell-cell interactions has tremendous value in several therapeutic fields. While genetically-encoded artificial receptors have proven efficacious, their scope is limited by the genetic engineering that underlies the approach. To circumvent some of these limitations, our group has developed a non-genetic method to modify any cell surface with a targeted protein scaffold. First, we engineered a protein ligand based upon the human tenth type III fibronectin domain (Fn3) that binds to epithelial cell adhesion molecule (EpCAM), an overexpressed tumor antigen. Using yeast surface display, mammalian cell panning, and a novel titratable avidity-reduction selection technique, we evolved Fn3 clones exhibiting high affinity and robust selectivity for cellular EpCAM. We then incorporated these Fn3s into a multivalent chemically self-assembled nanoring (CSAN). EpCAM-targeted CSANs were anchored to cell membranes through the hydrophobic insertion of phospholipids into the lipid bilayer. The targeting elements were subsequently removed from the cell surface by disassembling the CSAN with the antibiotic, trimethoprim. Using this system, we successfully directed and reversed targeted intercellular interactions *in vitro*. Finally, the modular CSANs were used to study how avidity impacts the apparent affinity of a multivalent scaffold. By tuning the number of Fn3 domains on the CSAN, we quantitatively described how the apparent affinity changes as a function of ligand affinity, domain valency, and antigen expression density. These results informed the development of a CSAN capable of discriminating between cells expressing different quantities of EpCAM both *in vitro* and *in vivo*. In conclusion, we developed a diverse toolkit for directing and studying cell-cell interactions. The CSAN platform is applicable to several therapeutic arenas and, by balancing affinity and avidity, may offer advantages over current cell-directing methods.

TABLE OF CONTENTS

LIST OF TABLES

Chapter II

Chapter IV

LIST OF FIGURES

Chapter I

Chapter II

Chapter III

Chapter IV

LIST OF ABBREVIATIONS

Abbreviation	Definition
%ID/g	Percent Injected Dose Per Gram
^{64}Cu	Copper-64
Ac_4GalNAz	Peracetylated *N*-Azidoacetylgalactosamine
ADC	Antibody Drug Conjugate
Aga1p	Agglutinin 1 Protein
Aga2p	Agglutinin 2 Protein
ATCC	American Type Culture Collection
Bio-PE	1,2-Dioleoyl-*sn*-Glycero-3-Phosphoethanolamine-*N*-(Biotinyl)
bisMTX	*Bis*-Methotrexate
BiTE	Bispecific T Cell Engager
BLAST	Basic Local Alignment Search Tool
CAIX	Carbonic Anhydrase IX
CAR	Chimeric Antigen Receptor
CD	Circular Dichroism
CEA	Carcinoembryonic Antigen
CFSE	Carboxyfluorescein Succinimidyl Ester
Ci	Curie
CMSP	Center for Mass Spectroscopy and Proteomics
Cryo-EM	Cryo Electron Microscopy
CSAN	Chemically Self-Assembled Nanoring
CT	Computed Tomography
CTV	CellTrace Violet
CuAAC	Copper(I)-Catalyzed Azide-Alkyne Cycloaddition
DARPin	Designed Ankyrin Protein Repeat
DHFR	Dihydrofolate Reductase
DIFO	Difluorinated Cyclooctyne
DMEM	Dulbecco's Modified Eagle's Medium
DNA	Deoxyribose Nucleic Acid
DOTA	1,4,7,10-Tetraazacyclododecane-1,4,7,10-Tetraacetic Acid
DOTAP	1,2-Dioleoyl-3-Trimethylammonium-Propane
DPAC	DNA-Programmed Assembly of Cells

dsDNA	Double-Stranded Deoxyribose Nucleic Acid
DSPE	1,2-Distearoyl-*sn*-Glycero-3-Phosphoethanolamine
DTT	Dithiothreitol
E. coli	Escherichia coli
EDTA	Ethylenediaminetetraacetic Acid
EGFR	Epithelial Growth Factor Receptor
EpCAM	Epithelial Cell Adhesion Molecule
EU	European Union
FACS	Fluorescence Activated Cell Sorting
FBS	Fetal Bovine Serum
FDA	Food and Drug Administration
FITC	Fluorescein Isothiocyanate
Fn3	Human Tenth Type III Fibronectin Domain
Gp2	T7 Phage Gene 2 Protein
GPI	Glycophosphatidylinositol
GPS	Glyosyltransferase-Programmed Stereosubstitution
HPLC	High Performance Liquid Chromatography
HSC	Hematopoietic Stem Cell
HUVEC	Human Ubmilical Vein Endothelial Cell
IACUC	Institutional Animal Care and Use Committee
IBD	Inflammatory Bowel Disease
IC_{50}	Half-Maximal Inhibitory Concentration
ICAM-1	Intercellular Adhesion Molecule 1
IDT	Integrated DNA Technologies
IgG	Immunoglobulin G
IHC	Immunohistochemistry
IL-2	Interleukin 2
IMAC	Immobilized Metal Affinity Chromatography
iPSC	Induced Pluripotent Stem Cell
IPTG	Isopropyl β-D-1-Thiogalactopyranoside
LB	Lysogeny Broth
MALDI-MS	Matrix-Assisted Laser Desorption/Ionization Mass Spectroscopy
ManNAc	Methacryloyl-*N*-Acetyl-Mannosamine
ManNAz	*N*-Azidoacetylmannosamine

MBq	Megabecquerel
MEC	Mammary Epithelial Cell
MFI	Mean or Median Fluorescence Intensity
MHC	Major Histocompatibility Complex
MI	Myocardial Infarction
MMAF	Monomethyl Auristatin F
MPS	Mononuclear Phagocytic System
MRSEC	Materials Research Science and Engineering Center
mSA	Monovalent Streptavidin
MSC	Mesenchymal Stem Cell
MUC1	Mucin 1
NEB	New England Biolabs
NHS	*N*-Hydroxysuccinimide
NIH	National Institutes of Health
NODAGA	1,4,7-Triazacyclononane-1-Glutaric Acid-4,7-Diacetic Acid
NSC	Neural Stem Cell
NSF	National Science Foundation
NSG	NOD.Cg-*Prkdc*^{scid} *Il2rg*^{tm1Wjl}/SzJ
OD_{600}	Optical Density at 600 nm
PBMC	Peripheral Blood Mononuclear Cell
PBS	Phosphate Buffered Saline
PBSA	Phosphate Buffered Saline with Albumin
PBSACM	Phosphate Buffered Saline with Albumin, Calcium, and Magnesium
PCR	Polymerase Chain Reaction
PE	Phycoerythrin
PEG	Polyethylene Glycol
PET	Positron Emission Tomography
POPC	Palmitoyl-Oleoyl-Phosphatidylcholine
PPG	Palmitated Protein G
PSGL-1	P-Selectin Glycoprotein Ligand 1
PTK7	Protein Tyrosine Kinase 7
RBC	Red Blood Cell
RPMI	Roswell Park Memorial Institute
scFv	Single Chain Variable Fragment

SDS-PAGE	Sodium Dodecyl Sulfate Polyacrylamide Gel Electrophoresis
SEC	Size Exclusion Chromatography
SiaNAz	Azido Sialic Acid
SIRM	Stress-Induced Rolling Membrane
sLe^X	Sialyl $Lewis^X$
SPAAC	Strain Promoted Alkyne/Azide Cycloaddition
ssDNA	Single Stranded Deoxyribose Nucleic Acid
T:NT	Targeted to Non-Targeted Ratio
TCEP	Tris(2-Carboxyethyl)-Phosphine HCl
TLR	Toll-Like Receptor
TMP	Trimethoprim
UV	Ultraviolet
vNAR	Variable New Antigen Receptor
β-CD	Beta-Cyclodextrin

DISCLOSURE OF PUBLICATION

Parts of the work presented in this dissertation comprise previously published manuscripts, manuscripts currently under peer-review, and manuscripts that will be submitted for publication. Chapters and subsections of this dissertation have been adapted from the following manuscripts. Finalized versions of the published works, if available, can be referenced at the proceeding citations:

1 Stern LA, **Csizmar CM**, Woldring DR, Wagner CR, Hackel BJ. Titratable Avidity Reduction Enhances Affinity Discrimination in Mammalian Cellular Selections of Yeast-Displayed Ligands. *ACS Combinatorial Science.* **2017**, *19*, 315-323.

2 **Csizmar CM**, Petersburg JR, Hendricks A, Stern LA, Hackel BJ, Wagner CR. Engineering Reversible Cell-Cell Interactions with Lipid Anchored Prosthetic Receptors. *Bioconjugate Chemistry*. **2018**, *29*, 1291-1301.

3 **Csizmar CM**, Petersburg JR, Wagner CR. Programming Cell-Cell Interactions Through Non-Genetic Membrane Engineering. *Cell Chemical Biology*. **2018**, *25*, 931-940.

4 **Csizmar CM**, Petersburg JR, Perry TJ, Rozumalski L, Hackel BJ, Wagner CR. Assessing the Role of Avidity on Multivalent Ligand Binding to Cell Membrane Antigens. [*Manuscript In Preparation*]

CHAPTER I

Introduction to Programming Cell-Cell Interactions through Non-Genetic Membrane Engineering

INTRODUCTION

Cell therapy has rapidly emerged as an invaluable tool in translational medicine and has led to significant advances in several diverse fields, including tissue engineering, regenerative medicine, and immunotherapy. Stem cells – in particular mesenchymal stem cells (MSCs), hematopoietic stem cells (HSCs), and, more recently, induced pluripotent stem cells (iPSCs) – have emerged as both a cornerstone of regenerative medicine and a versatile therapy for immune disorders. Meanwhile, T cells have been at the forefront of cancer immunotherapy for over a decade. However, the efficacy of these cellular therapies is ultimately contingent upon the ability to appropriately control the fate and function of the therapeutic cells. Specifically, cells must be successfully directed to engage in the cell-cell interactions required for a productive outcome. For example, systemic infusion of MSCs following a myocardial infarction results in less than 1% accumulation of cells in the ischemic myocardium.[1] In contrast, MSCs induced to upregulate chemotactic receptors prior to infusion exhibit more than a 2-fold increase in ischemic tissue homing.[2] For this reason, cellular engineering has become a crucial area of interest in cell therapy research.

Initial efforts in cellular engineering involved either preconditioning cells *ex vivo* via exposure to various stimuli (such as pharmacological agents, soluble cytokines, or stimulatory ligands) or the simultaneous administration of supportive adjuvant therapies. The goals of these approaches were to enhance the *in vivo* function of the infused cells, generate longer cell lifetimes, and promote self-renewal mechanisms to combat the inherent variability of cell biodistribution. While these strategies increased overall *in vivo* cell retention, they did little to directly influence the desired cell-cell interactions.

Over the past decade, genetic engineering has emerged as the most utilized and clinically efficacious cellular engineering approach. Indeed, genetically-engineered chimeric antigen receptor (CAR) T cells were recently approved by the United States Food and Drug Administration (FDA) for certain B cell malignancies.[3] In this approach, exogenous genetic material is incorporated into the T cell's genome where it encodes an artificial cell surface receptor that targets an antigen of interest.[4, 5] While genetic engineering is a robust strategy, it is associated with a number of significant drawbacks. For instance, the process is time consuming and produces results with variable and often unpredictable efficiency. Furthermore, not all cell types are amenable to such genetic alteration without deleterious effects – stem cells in particular. Finally, the genetic modification is typically permanent and irreversible, yielding significant adverse events in patients and raising long-term safety concerns for clinical applications.[6]

An alternative to genetic engineering is the use of bispecific ligands (e.g., bispecific antibodies, bispecific T cell engagers, etc.) designed to interface between two antigen expressing cells[7]. This approach has also demonstrated clinical efficacy, particularly in the context of T cell tumor targeting.[8] However, these ligands are not tethered to the cell surface, and because they generally rely on monovalent interactions with known membrane antigens, their cell-directing abilities are both dynamic and transient; coupled with their rapid clearance, this necessitates constant exposure to free bispecific ligand and makes them cumbersome to administer to patients.[9]

In an attempt to circumvent the limitations associated with genetic modifications and small bispecific ligands, effort has been made to develop non-genetic strategies to engineer cell surfaces with targeting elements capable of directing specific cell-cell interactions. Typically, these approaches are more transient (or reversible) and

applicable to numerous cell types, including stem cells. Furthermore, non-genetic approaches have been developed around lipid-, glycan-, and protein-based modifications, which is in contrast to genetic engineering methodologies focusing primarily on protein expression.

This introductory chapter summarizes the non-genetic membrane engineering approaches used in directing specific cell-cell interactions and discusses their current applications, both *in vitro* and *in vivo*. The most ideal features of these systems are described with emphasis on how these modifications can be applied to achieve the greatest translational benefit. Finally, the most promising strategies to date are outlined, and perspective is provided on future trends in this rapidly growing field.

NON-GENETIC APPROACHES TO MEMBRANE ENGINEERING

Several diverse, non-genetic approaches to cell membrane engineering have been developed. Typically, they fall into one of five broad categories: (1) the insertion of hydrophobic moieties into the lipid bilayer; (2) the direct chemical modification of cell surface constituents; (3) the membranous fusion of functionalized liposomes; (4) the use of functionalized sugar analogs to metabolically label surface glycoproteins; and (5) the enzymatic remodeling of membrane proteins (**Figure 1**).

Hydrophobic Insertion

Integral cell surface proteins are anchored into the membrane through hydrophobic transmembrane domains that interact with the hydrophobic interior of the lipid bilayer.[10] The hydrophobic effect dictates both the incorporation and orientation of integrated proteins and locks them on the cell surface, barring cell membrane internalization.[11] These same principles have been utilized for cellular engineering, where the desired

ligand or chemical moiety is conjugated to a hydrophobic anchor and then incubated with the to-be-labeled cell population. As a thermodynamically favored process,[12-14] the hydrophobic anchor will spontaneously insert into the lipid bilayer and effectively tether the attached species to the membrane (**Figure 1A**).

Such membrane insertion has been accomplished with a variety of hydrophobic tags, including alkyl chains,[12] lipid moieties,[15] and glycophosphatidylinositol (GPI) anchors.[16] Multiple methods for attaching these tags to the desired cargo have also been developed. Perhaps the most common approach is the chemical ligation of the tag by peptide couplings with activated esters,[17] sulfhydryl-based Michael additions,[18] or click ligations between azide groups and various alkynes. [19] In contrast, others have devised methods to produce hydrophobically-tagged ligands recombinantly, thereby omitting the additional conjugation step.[16, 20]

The relative ease with which cell surfaces can be "painted" with these hydrophobically-tagged species has made it a popular approach for the attachment of a wide variety of cargo. Targeting elements – including aptamers,[21, 22] antibody-derived single chain variable fragments (scFvs), [20] and peptides[15, 23] – are commonly installed on the cell membrane in this fashion. By first anchoring proteins A and G, several laboratories have functionalized cells with full antibodies[17, 24] and Fc-tagged fusion proteins.[25] Oligonucleotides have been installed as well, enabling the clustering of cells functionalized with complimentary sequences.[26, 27] Finally, some have attached larger cell-targeting scaffolds, including nanoparticles[12, 28, 29] and polymers.[30] Notably, these methods were further developed into synthetic targeting systems used to direct artificial cell-cell interactions *in vitro*.

Chemical Modification

A straightforward membrane engineering strategy is the direct chemical conjugation of small molecules and tethered cargo to functional groups that preexist on the cell surface (**Figure 1B**). These natural functional groups (such as free amines present on lysine side chains) are attractive targets for the covalent conjugation of various ligands since they require no preconditioning of the cell, chemical or otherwise. Furthermore, this approach can be used to modify essentially any cell membrane component – including proteins, lipids, carbohydrates, and glycans – albeit in a largely non-specific manner.

The use of *N*-hydroxysuccinimide (NHS)-activated esters to modify lysine residues and other surface amines is by far the most common strategy for chemical modification. This approach has long been used to non-specifically biotinylate cell surfaces for a host of applications, and several groups have since applied this scheme to the induction of intercellular interactions. In a typical workflow, cells are first biotinylated with an NHS-biotin conjugate before incubating them with tetravalent streptavidin. The streptavidin binds to the biotin moieties on the cell surface where it serves as a "bridge" to connect biotinylated ligands to the cell (**Figure 1B**). This streptavidin bridging approach has been used to functionalize cell surfaces with P-selectin binding aptamers,[31] sialyl Lewis^X (sLe^X) motifs,[32] and antibodies recognizing epithelial growth factor receptor (EGFR).[33] These membrane-engineered cells were then capable of interacting with selectin-expressing endothelial cells (*in vitro*[31] and *in vivo*[32]) and with EGFR-expressing HEK 293T and HeLa cells,[33] respectively. Finally, streptavidin has been used to bridge directly between biotinylated cells to generate cell clusters and layers.[34]

Of course, NHS-esters can be used to conjugate species other than biotin to the cell surface, including various bioorthogonal functional groups. This approach was used to

install reactive maleimide groups on the surface of MSCs which, through the Michael addition of a sulfhydryl group, were subsequently labeled with thiolated peptides targeting E-selectin.[35]

Few groups have used chemistries other than NHS-activated esters to functionalize cell surfaces for the purpose of directing cell-cell interactions. Early work demonstrated that erythrocytes could be labeled with anti-CD90.2 (Thy-1.2) antibodies via chromic chloride coupling.[36] More recently, polymers composed of *N*-vinylpyrrolidone and 3-(acrylamide)phenylboronic acid, the latter of which binds cell membrane glycoproteins through covalent boronate ester bonds, were able to cross-link cells to form non-specific aggregates in culture media.[37]

Liposome Fusion

Lipid membrane fusion is a critical process in normal cell biology and has been the subject of intense investigation. Not surprisingly, membrane fusion has been readily adapted for several applications, including membrane engineering. When incubated with cells, functional group-containing liposomes spontaneously fuse with the cell membrane to present the respective functional groups on the cell surface (**Figure 1C**). Such liposomes can be readily formed by dissolving the desired lipid species in a volatile solvent (e.g., chloroform), concentrating/drying them under high vacuum, resuspending them in the desired aqueous buffer, and finally applying an agitating stimulus (commonly sonication) to drive the formation of unilamellar vesicles.[38, 39]

This approach was used to from vesicles composed of the biotinylated lipid 1,2-dioleoyl-sn-glycero-3-phosphoethanolamine-N-(biotinyl) (Bio-PE), which were subsequently

fused with MSC membranes to functionalize the cell surface with biotin.[38] Streptavidin was then used as a bridge (see above) to tether biotinylated sLe^X motifs to the surface.

The Yousaf group has extensively advanced liposome fusion technology, and their work provides the most robust examples of forming targeted intercellular interactions via this approach. In their system, liposomes composed of POPC (palmitoyl-oleoyl phosphatidylcholine), DOTAP (1,2-dioleoyl-3-trimethylammonium-propane), and either dodecanone or *O*-dodecyloxyamine are spontaneously fused to cell membranes to present ketone or oxyamine groups, respectively, on the cell surface.[39] Cells bearing the complementary ketone and oxyamine moieties were then linked to one another via a covalent oxime ligation. When applied to multiple cell types, the Yousaf group has been able to form multicellular sheets,[40] spheroids,[41] and microtissues.[42]

Metabolic Modification

The technique of metabolically introducing novel functional groups to the plasma membrane was first pioneered in 1992[43] and capitalized upon the promiscuity of natural carbohydrate biosynthesis pathways to metabolically incorporate non-physiologic amino sugar analogues into membrane glycoconjugates (**Figure 1D**).

Expanding upon this approach, Jurkat cells were metabolically labeled with the azide-functionalized mannose derivative, *N*-azidoacetylmannosamine (ManNAz), affording the incorporation of azido sialic acid (SiaNAz) residues on the surface.[44] The SiaNAz residues were then reacted with phosphine-conjugated ssDNA oligonucleotides via Staudinger Ligation or with difluorinated cyclooctyne (DIFO)-conjugated ssDNA oligonucleotides via copper-free click chemistry. Cells bearing complementary oligonucleotide sequences were able to assemble into aggregates.

A similar strategy was used to metabolically label cells with peracetylated N-azidoacetylgalactosamine (Ac_4GalNAz), introducing azido groups into cell surface glycoconjugates.[45] Copper(I)-catalyzed azide-alkyne cycloaddition (CuAAC) was then used to install a pegylated β-cyclodextrin (β-CD). The β-CD subsequently bound homobifunctional azobenzene species that bridged between β-CD-functionalized cells. Similarly, azobenzene-conjugated aptamers targeting mucin 1 (MUC1) were installed on the metabolically-engineered cells, enabling the recognition of MUC1+ targets.

In addition to azido sugar moieties, a synthetic methacryloyl-modified analog of *N*-acetyl mannosamine (ManNAc), termed ManM, was used to install methacryloyl groups in surface sialic acid residues.[46] The ManM groups were then coupled to thiol-terminated aptamers targeting protein tyrosine kinase-7 (PTK7) via a light-assisted (505 nm) thiol-ene reaction utilizing eosin Y as a photosensitizer. Ultimately, aptamer-functionalized macrophages were able to recognize and bind to PTK7+ human T lymphoblasts *in vitro*.

Enzymatic Remodeling

A less common approach to cell-surface engineering involves the use of enzymes to modify naturally-present proteins and glycans (**Figure 1E**).[47] One method takes advantage of the popular "sortagging" technique. Here, the *Staphylococcus aureus* enzyme sortase A is used to conjugate appropriately tagged ligands to the cell surface. Notably, this approach has been used to conjugate antibodies onto naturally exposed *N*-terminal glycine residues on T cells.[48]

Additionally, a process known as glycosyltransferase-programmed stereosubstitution (GPS) has been employed to convert CD44 on the surface of neural stem cells (NSCs) into an isoform capable of binding to E-selectin.[49] Specifically, the α(1,3)-linkage specific fucosyltransferase VI was used to install a fucose group onto terminal 2-lactosamine units. When those lactosamines were then capped with an α(2,3)-linked sialic acid, sLe^x epitopes capable of being recognized by P- and E-selectin residues were created. NSCs modified in this manner were then able to interact with E-selectin expressing endothelial cells and demonstrated increased transendothelial extravasation *in vitro*.

APPLICATIONS FOR ENGINEERED CELL-CELL INTERACTIONS

Though membrane-engineered cells have been explored in numerous contexts,[50] their use to direct cell-cell interactions has been most frequently applied to four fields – tissue engineering, cell-based immunotherapy, targeted cell adhesion, and regenerative medicine (**Figure 2**).

Tissue Engineering

The ability to generate fully functional tissues and organs *in vitro* has been a long-standing goal of biomedical science. Requisite to this aim is the capacity to direct the constituent cell types to interact with one another in a manner that recapitulates the parent tissue's usual *in vivo* development. To this end, several groups have used membrane-engineered cells to direct the formation of ordered microtissues composed of different cell types. For example, Yousaf and coworkers have long used a liposome fusion approach to functionalize cell surfaces with bioorthogonal ketone and oxyamine groups. Taking advantage of the oxime ligation, they first formed directed cell clusters of complimentarily-labeled cells, including murine fibroblasts,[39] which could be further

assembled into ordered cellular spheroids and sheets.[40] Additional control over the order and cellular hierarchy of these microtissues was achieved using a microfluidic chamber to regulate the addition and ligation of ketone and oxyamine-labeled cells.[41] Ultimately, they were able to use this methodology to assemble fibroblasts, cardiomyocytes, and HUVECs into a functional three-dimensional (3D) cardiac tissue that was able to beat spontaneously and synchronously. Importantly, neighboring cells in this tissue both developed physiologic intercellular junctions – including the gap-junction protein connexin 43 – and produced extracellular matrix, suggesting a more accurate recapitulation of the normal cardiac environment *in vivo*.[42] Furthermore, the induced cell-cell interactions could be reversed by UV irradiation when a photocleavable group was incorporated into the oxyamine component.[51] This approach was then applied to fibroblasts, adipocytes, and hMSCs to generate 3D microtissues *in vitro*.[51] Similarly, when hMSCs and fibroblasts were modified with hydroquinone and oxyamine groups, respectively, the formation of cell clusters could be induced by chemical or electrochemical oxidation of the hydroquinone to a reactive quinone moiety, which then coupled to oxyamine-labeled cells. The cell clustering could then be reversed via reduction of the quinone back to a hydroxyquinone.[52] Unfortunately, neither of these reversal mechanisms – photocleavage or electrochemical reduction – are currently applicable to *in vivo* applications.

Rather than covalently couple cell types together, the liposome-fusion approach can also be used to functionalize cell surfaces with targeting elements. Fibroblasts were first modified with a hydrazone-coupled ligand, and then that ligand was exchanged *in situ* for an oxyamine-conjugated RGD peptide. These RGD-functionalized fibroblasts were then able to recognize and adhere to other integrin-expressing fibroblasts, enabling the formation of tissue microlayers *in vitro*.[53]

Another approach to assembling cells for tissue engineering involves cross-linking biotinylated cells with a tetravalent streptavidin moiety. In one example, cell surfaces are non-specifically labeled at primary amines with a reactive NHS-biotin; labeled cells are then clustered together by the addition of streptavidin, whose multiple biotin binding domains enable the formation of a "bridge" between labeled cells. The Jiang group used this technique to assemble layers of Jurkat cells on top of HUVEC cells and, separately, HUVEC cells on top of fibroblasts *in vitro*. Using fabricated two-dimensional (2D) stress-induced rolling membranes (SIRMs), they were able to pattern HUVECs on top of smooth muscle cells, and then roll the 2D substrate into a 3D tube resembling a blood vessel.[34] Similarly, a hexagonal microarray assembled from biotinylated ssDNA oligonucleotides was able to attach to biotinylated Jurkat cells via streptavidin bridges.[33] When biotinylated anti-EGFR antibodies were attached to the microarray, EGFR-expressing HEK 293T and HeLa cells could be captured. In this manner, the microarrays were also able to form intercellular bridges between EGFR-expressing cells, enabling the formation of cell pairs and clusters.[33]

Gartner and Bertozzi have used oligonucleotides to assemble metabolically engineered cells. SiaNAz-functionalized Jurkat cells were labeled with ssDNA oligonucleotides, and cells bearing complementary sequences assembled into aggregates.[44] The order of cells in these aggregates could be controlled stoichiometrically. Furthermore, these cellular interactions could be reversed by two strategies: (1) melting of the hybridized ssDNA sequences at 37 ºC, and (2) degradation by DNase. This DNA-programmed assembly of cells (DPAC) has further been used to form specific 3D arrangements of cells and microtissues.[26] In this approach, phospholipid-conjugated ssDNA oligonucleotides are

hydrophobically inserted into cell membranes. Cells labeled with complimentary ssDNA sequences could then patterned into microtissues in a Matrigel matrix.

Cell-Based Immunotherapy

The therapeutic potential of cell-directed immunotherapies is underscored by the clinical successes of CAR T cells.[3] However, the limitations of the CAR platform have driven many groups to seek non-genetic methods to introduce targeting elements to the T cell surface. For instance, early work by the Al-Katib group sought to deliver cytotoxic payloads directly to CD20-expressing tumor cells through targeted erythrocytes. They developed and expressed a glycosylphosphatidylinositol (GPI)-fused anti-CD20 single chain variable fragment (scFv) that was hydrophobically inserted into red blood cell (RBC) membranes. These anti-CD20 RBCs were then able to recognize and bind to B cells *in vitro*, forming visible rosettes.[16]

Using metabolic engineering, Qu and coworkers sought to target peripheral blood mononuclear cells (PBMCs) to breast adenocarcinoma cells. PBMCs were labeled with Ac_4GalNAz to yield cell surface azide groups that were subsequently conjugated to a β-CD. Azobenzene-conjugated anti-MUC1 aptamers were then installed on the PBMCs, enabling them to target the MUC 1+ breast adenocarcinoma MCF-7 cell line *in vitro*.[45]

The Wagner group has utilized a chemically self-assembled nanoring (CSAN) to non-covalently introduce targeting elements to T cell surfaces. CSANs incorporating anti-epithelial cell adhesion molecule (EpCAM) scFvs and phospholipids hydrophobically inserted into T cell membranes, enabling them to selectively recognize and eradicate EpCAM-expressing MCF-7 cells in co-culture with EpCAM-negative U87 cells.[28]

Using the "sortagging" approach, Swee and coworkers installed anti-mouse class-II MHC antibodies onto activated CD8+ T cells. These T cells were then able to selectively recognize and kill antigen-expressing splenocytes *in vitro*.[48]

Macrophages have also been explored as immunotherapeutic mediators. Logtenberg *et al*. sought to enhance the anti-tumor response of cancer vaccines by targeting irradiated tumor cells to antigen presenting macrophages. They expressed and purified lipid-fusions of scFvs targeting CD14, CD32, and CD64. When these lipid-scFv fusions were hydrophobically inserted into the membrane of Jurkat cells, the cells targeted to and were phagocytosed by macrophages.[20] Finally, metabolically functionalized murine macrophage-like cells (RAW264.7) have been labeled with aptamers targeting the circulating cancer cell marker PTK7. These aptamer-targeted macrophages were able to recognize and phagocytose PTK7+ CCRF-CEM (T lymphoblast) cells *in vitro.*[46]

Unlike most approaches that drive immune cells to eradicate a particular target, Ko *et al.* took advantage of the immunosuppressive capabilities of MSCs to design a targeted cellular therapy for inflammatory bowel disease (IBD). Palmitated protein G (PPG)-painted MSCs were armed with antibodies to target them to the inflamed endothelium within the colon and draining mesenteric lymph nodes. Following intravenous infusion in a murine model of IBD, the functionalized MSCs exhibited increased localization within the inflamed tissues, reduced inflammation (assessed by colon length and histology), an increase in the percentage of regulatory T cells, and improved overall survival.[54]

Enhanced Cell Delivery

A major barrier to the targeted delivery of stem cells is the inefficiency with which they extravasate from the vasculature and accumulate within the target tissue.[55, 56] To

address this, many groups have sought to surface engineer stem cells with targeting elements designed to promote their adhesion to, rolling along, and extravasation through the vascular endothelium. The Karp laboratory has had a longstanding interest in modifying MSCs to bind to selectin-expressing surfaces. In one approach, MSCs were non-specifically biotinylated with NHS-biotin; then, streptavidin was used to tether biotinylated sLe^X motifs to the MSCs. These sLe^X-labeled MSCs then exhibited a robust rolling response on inflamed endothelium *in vivo* and homed to inflamed tissue with higher efficiency than native MSCs.[32] Rather than tether sLe^X motifs to biotinylated MSCs, the group has also tethered biotinylated selectin-binding aptamers to the MSCs through the streptavidin bridge. Similar to before, these aptamer-modified MSCs were able to recognized selectin-expressing HUVECs and neutrophils.[31]

The Dennis group has also shown interest in this area, having labeled protein G with NHS-conjugated palmitic acids and hydrophobically inserting them into MSC membranes. The PPG modified MSCs were further labeled with antibodies targeting intercellular adhesion molecule 1 (ICAM-1), enabling their recognition of HUVEC cells *in vitro*, even under physiologic flow conditions.[17] Neelamegham and coworkers similarly inserted PPG into MSC membranes, but rather than use it to bind a pre-existing antibody, they bound a custom fusion protein consisting of the first 19 amino acids of PSGL-1 (the pan-selectin binder "P-selectin glycoprotein ligand-1") fused to a human IgG tail. A core-2 sLe^X motif is also engineered at the *N*-terminus to confer "leukocyte-like" tethering and rolling properties. Ultimately, MSCs functionalized with protein G and this fusion protein interacted with P- and E-selectin expressing HUVECs and exhibited tethering and rolling properties similar to leukocytes *in vitro*.[25]

Beyond selectins, some groups have used lipid-anchored glycan mimetics to modulate the bulk properties of a cell's native glycocalyx. The insertion of long glycoprotein mimetics into the cell membrane drove the reorganization of cell surface receptors and, specifically, the clustering of integrins.[57] This enhanced the adhesion of mammary epithelial cells (MECs) to the extracellular matrix, and identified a potential mechanism for promoting metastasis of malignant cells. Likewise, cells adorned with longer glycoprotein mimetics exhibited enhanced metastatic potential *in vivo* and increased cell proliferation within the metastatic niche.[58] Thus, these techniques can be used as tools to elucidate fundamental cell biology and explore how cell interact with their environments through both cellular contacts and membrane milieus.

Regenerative Medicine

Targeting stem cells to sites of tissue injury is an attractive approach to regenerative medicine. Few groups have applied non-genetic cell surface engineering approaches to this problem. Dennis and coworkers used phage display to identify peptides that selectively recognize ischemic myocardium in a mouse model of myocardial infarction (MI). They then synthesized these MI-targeting peptides with a palmitic acid tail, enabling their hydrophobic insertion into MSC membranes. In a mouse model of MI, targeted MSCs injected into the tail vein homed to and accumulated within ischemic myocardium to a greater extent than non-targeted MSCs.[15]

The Sackstein group used enzymatic glycoengineering to generate neural stem cells (NSCs) capable of binding E-selectins. These engineered NSCs were shown to interact with E-selectin expressing HUVECs *in vitro*, and in a mouse model of experimental autoimmune encephalitis, were able to undergo transendothelial extravasation to accumulate in the brain, spleen, and liver parenchyma.[49]

PERSPECTIVE

Given the diverse applications of surface-engineered cells – and the multitude of approaches to generating such cells – it is unlikely that a single engineering system will prove sufficient for all applications. Still, results from both the bench and clinic offer insights into what features of the membrane-engineering system may be beneficial for a given application. For example, while genetically-engineered CAR T cells have proven efficacious for the treatment of certain hematologic malignancies, their success in treating solid tumors has been hampered by both "on-target off-tumor" toxicities and an inability to provide functional replacements for the damaged tissues (e.g., B cell aplasia can be partly overcome by regular infusions of intravenous immunoglobulins).[4, 6, 59] This highlights the notion that, while permanent, genetically-encoded modifications may be beneficial in some instances, a temporary or reversible cell-targeting modification may prove superior under other circumstances.

Based upon such examples and the current literature at large, we propose a short list of "ideal" features for non-genetic membrane engineering approaches as they relate to the formation of targeted cell-cell interactions. We postulate that fulfillment of most of these criteria will facilitate both preclinical success and clinical adoption of these technologies. Specifically, such systems should be: (1) stable under physiologic conditions; (2) universally applicable to all cell types; (3) phenotypically innocuous to the modified cell; and (4) reversible upon administration of a controlled stimulus.

Stability

In vivo stability is a potential limiting factor for certain approaches, particularly lipid- and oligonucleotide-based modifications. For instance, the half-life of lipid-tagged scFv

fragments on cell surfaces in culture media at 37 ºC was reported to range from mere minutes to only several hours.[20] Similarly, targeted peptides synthesized with palmitic acid tails exhibited a cell surface half-life of less than one hour in culture media at 37 ºC.[15] The reason for this is likely multifaceted. Many lipid-anchored constructs can diffuse out of the plasma membrane and partition between the cell surface and the aqueous phase.[60] The extent of this partitioning can be modulated by varying the hydrophobicity of the anchor, where an increase in net hydrophobicity serves to more stably anchor ligands to the membrane.[61] Additionally, some lipid-conjugated agents undergo rapid endocytosis.[47, 62] Once internalized, the species may be degraded, become trapped within endosomes, or incorporated into intracellular membranes, making them inaccessible for mediating cell-cell interactions.[39, 63]

In contrast, approaches using more than one lipid anchor have demonstrated prolonged stability on the cell surface. Protein G, when non-specifically coupled to a palmitic acid moiety, remained ≥25% incorporated into to the cell membrane at 48 h.[25] Similarly, when eight diacyl phospholipids were incorporated into a self-assembling nanoring, the construct remained stably bound (≥20%) to the cell surface for over 72 h.[28, 29] On these longer time-scales, cell division serves to dilute the concentration of the surface modification as well. Furthermore, physiologic membrane recycling can return certain hydrophobic ligands to the cell surface, prolonging their overall display and propagating the modification to daughter cells.[63] These results indicate that hydrophobically inserted modifications can persist on cell surfaces for meaningful periods of time, provided appropriate anchoring or recycling mechanisms.

Aside from the stability of the membrane-anchoring component of the system, the cell-targeting component is also subject to scrutiny. Certain aptamers used in this context will

denature and lose their binding efficacy at 37 ºC, limiting their use *in vivo*.[21] Similarly, complementary oligonucleotides have been used to form targeted cell associations,[44] but these early double-stranded DNA (dsDNA) constructs melted at 37 ºC, dissociating the cells and restricting this approach to *ex vitro* applications. Thermal stability could be increased using chemically modified oligonucleotides or by increasing the GC content of the strands. While this could enable *in vivo* use, enzymatic degradation and toll-like receptor (TLR) activation remain potential barriers.

Universality

Another important aspect of membrane engineering approaches is the degree to which they can be generalized to different cell types. This is especially true for tissue engineering applications where a key goal is to drive interactions between the numerous cell lineages comprising a functional tissue or organ. Fortunately, many of the non-genetic approaches discussed here have each been applied to a wide array of cell types – including lymphocytes,[28] MSCs,[15] cardiomyocytes,[42] and vascular endothelial cells[34] – suggesting that non-genetic alterations relying solely upon membrane modification may be uniquely flexible and thus find use in a variety of applications.

Nevertheless, some approaches have been shown to have a more limited scope or variable degrees of efficacy. For example, the enzymatic glycoengineering approach described by Merzaban *et al.* requires that the target cell express the protein substrate (CD44) of the modifying enzyme (fucosyltransferase VI).[49] Meanwhile, the hydrophobic insertion of fluorescently labeled phospholipid conjugates sometimes has variable efficacy amongst different cell types,[23] suggesting that the insertion kinetics may differ based upon cell size, morphology, or the local cell membrane constituency.

Innocuity

In order for a membrane modification to be universal it must also be innocuous. This is especially important for stem cells, as the modification should neither drive the differentiation of the cell nor reduce its multipotency. Genetically encoded modifications have met little success in the arena of stem cells, as the genetic manipulation typically causes a decrease in pluripotency.[64] However, non-genetic approaches – including hydrophobic insertion,[17, 65] chemical modification,[35] liposome fusion,[52] metabolic engineering,[66] and enzymatic remodeling[49] – have been successfully applied to stem and progenitor cell populations without altering their multi-lineage differentiation capabilities. Consequently, these non-genetic approaches, which don't typically rely upon the engagement of a physiologic receptor on the cell membrane, may be uniquely suited to directed stem cell therapies. Still, innocuity is not guaranteed for these techniques, as the hydrophobic insertion of bulky glycopeptide mimetics has profound effects on the ECM adherence and metastatic potential of cells.[57, 58] Thus, the degree to which these surface modifications alter the cell's phenotype likely need to be defined on an individual basis and in a context-dependent manner.

Reversibility

Temporospatial control over the cell surface modification is highly desirable, as it has the potential to reduce the incidence and severity of adverse clinical events and thereby increase the scope of amenable applications. For example, the inability to remove CARs from T cells leads to both persistent B cell aplasia and immense difficulty translating the CAR platform to solid tumors. In this context, a reversible cell surface modification might enable the rapid removal of targeting capability from engineered lymphocytes, enabling the recovery of healthy B and plasma cells or reducing off-tumor toxicities.

While the short half-life of some methods can be viewed as an inherent reversibility, the inability to specifically trigger the removal of such ligands from the cell membrane is a disadvantage. To this end, many groups have incorporated temporospatial control mechanisms into their surface modification approaches. For example, the introduction of photoisomerizable[45] and photocleavable[51] groups into the modifications has allowing their removal upon UV irradiation. Electrochemical reversibility has also been demonstrated, with the formation and cleavage of oxime linkages reliant upon oxidation and reduction, respectively.[52] Additionally, several groups have utilized temperature as a stimulus via thermally-reversible polymers,[37] oligonucleotides,[44] and aptamers.[21] Enzymatic reversibility has been shown, with exposure to DNase triggering the degradation of oligonucleotides responsible for cell-cell adhesion.[22, 44] Aside from the systemic administration of human DNase to degrade DNA-based interactions, however, few of these reversal mechanisms are directly applicable to *in vivo* applications.

Thus far, the Wagner group has demonstrated the most readily translatable mechanism for reversal. In their approach, phospholipid-functionalized nanorings incorporating an EpCAM-targeting scFv were hydrophobically inserted into cell membranes. The nanorings could be disassembled in the presence of clinically-relevant concentrations of the orally bioavailable and FDA-approved antibiotic, trimethoprim, driving the dissociation of the targeting construct and providing a pharmacologic trigger for reversing the cell-cell interactions.[28, 29]

Clinical Translatability

While many of these non-genetic membrane modifications have demonstrated preclinical success at directing cell-cell interactions, none have been successfully translated into the clinic to date. While the barriers to clinical translation are both steep

and somewhat application specific, incorporating the “ideal” features previously discussed may help overcome these difficulties. For example, tissue engineering modifications should be both applicable to multiple cell types to facilitate organ construction and readily removable to reduce the potential immunogenicity of the implanted tissue. Immunotherapy modifications ought to be rapidly and specifically reversible, providing an “off switch” should cellular toxicities arise. Cell delivery modifications should be stable enough to persist on the membrane throughout extended circulation, vessel adhesion/rolling, and extravasation through the endothelium. Finally, regenerative medicine modifications intended to enhance stem cell homing should be innocuous and not alter the stem cell’s pluripotency prematurely.

ROLE OF DOCTORAL THESIS IN THE CURRENT FIELD

Non-genetic membrane engineering is a powerful tool for directing targeted cell-cell interactions. A variety of approaches have been developed for this purpose, including hydrophobic insertion, chemical modification, liposome fusion, metabolic engineering, and enzymatic remodeling. Collectively, these techniques have demonstrated significant preclinical results in the fields of tissue engineering, cell-based immunotherapy, targeted cell delivery, and regenerative medicine. Still, significant barriers to clinical translation still exist for these methodologies. To that end, work is underway to make these systems more rapid, stable, universal, innocuous, and reversible – features which may help overcome the adverse events noted with other cell surface engineering modalities.

Accordingly, the experiments and results presented in this thesis expand upon the field of non-genetically engineered cell-cell interactions by describing a new system that meets these desired criteria. Notably, the achievement of all five criteria within a single

system distinguishes this approach from previously developed membrane-engineering technologies.

This was accomplished by first developing a targeting ligand based upon the human tenth type III fibronectin domain (Fn3) that binds to our model antigen, EpCAM (*Chapter II*). These Fn3 domains were then incorporated into a multivalent chemically self-assembled nanoring (CSAN) that was subsequently installed on cell surfaces via hydrophobic insertion; the membrane-anchored CSAN was able to direct targeted cell-cell interactions that were pharmacologically reversible (*Chapter III*). Finally, the effects of scaffold valency, ligand affinity, and antigen expression density on cellular recognition were quantitatively defined, and this analysis informed the development of targeted CSANs capable of discriminating between cell populations expressing different quantities of EpCAM both *in vitro* and *in vivo* (*Chapter IV*).

Ultimately, these non-genetic membrane-engineering systems – including the methods disclosed here – are poised to broadly enable and expand the use of cell-based therapies across multiple basic science and clinical disciplines.

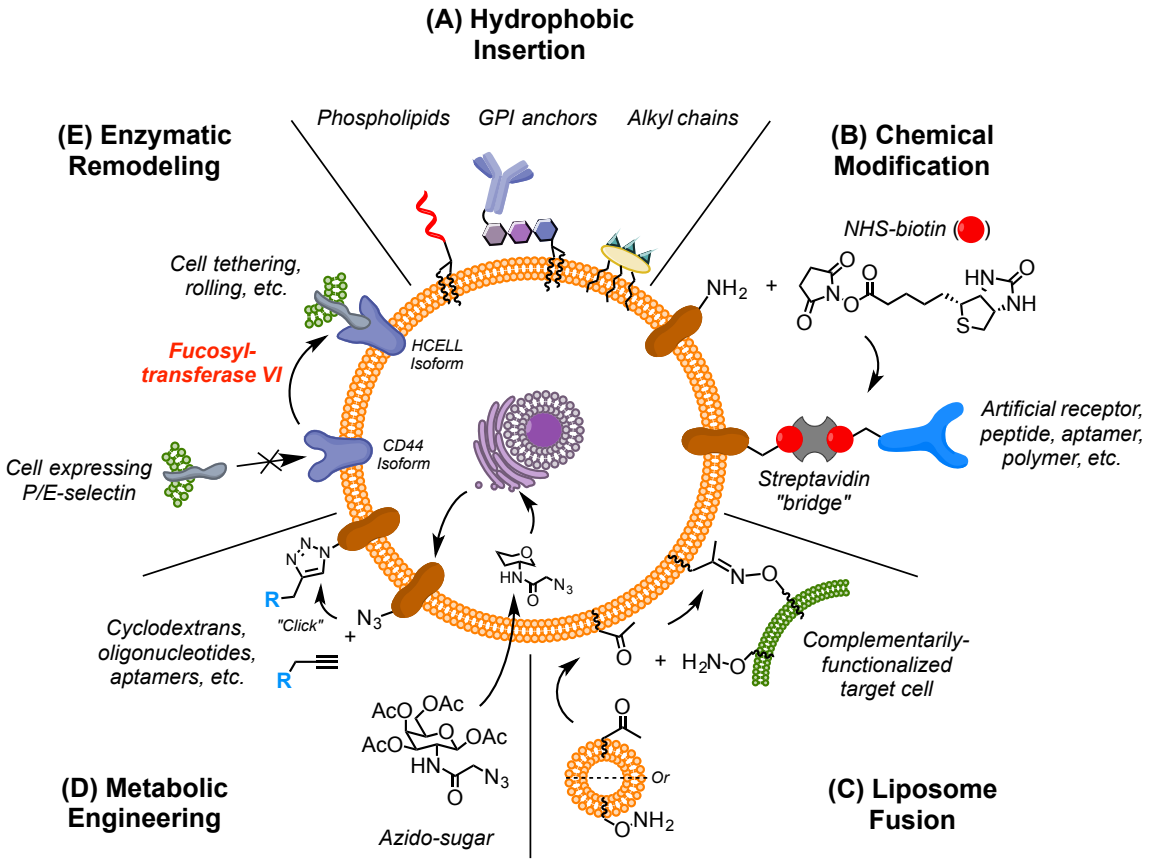

Figure 1. Non-Genetic Membrane Engineering Approaches to Direct Intercellular Interactions. Several non-genetic methods for cell membrane modification have been used to direct cell-cell interactions. (A) Hydrophobic groups spontaneously insert into the lipid bilayer, tethering conjugated cargo or ligands to the surface. (B) Functional groups naturally present on the cell surface can be reacted with chemical moieties to covalently tether a variety of species; in many cases, biotin is installed and streptavidin is used as a “bridge” to link other ligands. (C) Liposomes bearing various functional groups spontaneously fuse with the cell membrane, decorating the surface with the respective modifications. (D) Bioorthogonal groups are incorporated into surface glycoproteins by growing cells in media supplemented with functionalized sugar analogs; these groups can then be conjugated to exogenous ligands. (E) Enzymes can be used to modify

naturally-existing proteins and glycans on the cell surface, creating divergent isoforms or tethering synthetic targeting elements.

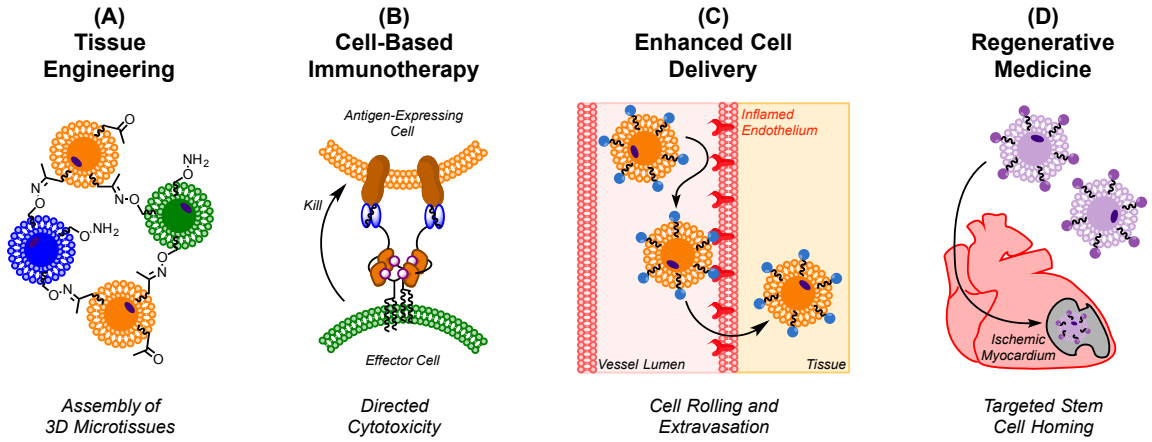

Figure 2. Applications of Engineered Cell-Cell Interactions. Non-genetically engineered cell-cell interactions are broadly applicable to a variety of fields. (A) The linking of multiple tissue types in vitro can be applied to tissue engineering. (B) Cytotoxic T cells can be directed to – and subsequently kill – antigen expressing cells for immunotherapy. Alternatively, engineered antigen presenting cells can be used to prime T cells against a particular target. (C) Therapeutic cells can be modified to more efficiently tether, roll, and extravasate through the vasculature, improving their delivery to target tissues. (D) Regenerative stem and progenitor cells can be functionalized with targeting ligands that enhance their accumulation within sites of injury.

CHAPTER II

Development and Application of Fibronectin Domains with Engineered Specificity for Epithelial Cell Adhesion Molecule

INTRODUCTION

Targeted molecular agents have become a cornerstone of contemporary therapeutics and diagnostics.[67] While antibodies and their derivatives are the most common protein scaffolds used in these contexts, the biophysical properties of antibodies make them less than ideal for a variety of applications. For instance, their large size contributes to a long serum-half life (undesirable for imaging applications), their structural reliance upon disulfide bonds preempts rapid, soluble production in bacterial cytosol (requiring time-consuming and expensive periplasmic or mammalian expression systems), and their complex assembly hinders further downstream engineering (such as site-specific conjugation to various cargo).[68, 69] To overcome some of these limitations, there is an intense interest in developing non-immunoglobulin protein scaffolds capable of binding to targets of interest with high affinity and specificity.

To that end, a large number of protein domains have been evaluated as suitable binding ligands, including the Z-domain of staphylococcal protein A (affibodies), the tenth type III fibronectin domain (monobodies), designed ankyrin protein repeats (DARPins), lipocalins (anticalins), cysteine knots (knottins), and the T7 phage gene 2 protein (Gp2).[69-71] In order to obtain specific binders derived from these ligands, a combinatorial library of the scaffold is created at the DNA level using degenerate codons to randomize appropriate amino acid positions.[68] Clones exhibiting the desired properties must then be selected from the library through one of several methodologies, including phage display,[72] ribosome display,[73] mRNA display,[74] bacterial surface display,[75] or yeast surface display.[76] In this manner, these domains have been engineered into high-affinity and highly specific binders to a wide array of cellular antigens.[68, 70, 77]

Epithelial cell adhesion molecule (EpCAM, CD326) is a type I transmembrane glycoprotein that, true to its name, is expressed only on cells of epithelial differentiation.[78] EpCAM has a physiologic role in assembly and maintenance of adhesive cell-cell contacts.[79-82] Accordingly, it is typically expressed in low levels on the basolateral surface of epithelial cells where it can interface neighboring tissue.[78] In contrast, various epithelial malignancies (i.e., carcinomas) – including those of the breast, pancreas, colon, and prostate – have been shown to grossly overexpress EpCAM and aberrantly display it across the cell surface where it is more accessible.[78, 83] This differential in expression made it an early carcinoma marker and target for therapeutic intervention.[84] More recently, EpCAM has been identified as a marker of cancer stem cells, further fostering clinical interest in this antigen.[85, 86] Indeed, an anti-EpCAM/anti-CD3 bispecific antibody, Catumaxomab, has been approved for the treatment of malignant ascites in the European Union (EU),[87] and a multitude of additional EpCAM-directed therapeutics are currently under clinical investigation.[88]

Likewise, several protein scaffolds have been engineered to bind to EpCAM, including antibodies and their fragments[87, 88], shark variable new antigen receptors (vNARs),[89, 90] DARPins,[91, 92] and small cyclic peptides.[93] However, detriments with these established ligands – including disulfide linkages, non-human origin, and low affinity – created an opportunity to design superior EpCAM binders. The fibronectin scaffold is based upon the human tenth type III fibronectin domain (Fn3).[94, 95] It is composed of seven antiparallel beta sheets, each connected by a flexible loop region (**Figure 1**). Three of these loops are particularly amenable to randomization and diversification, enabling the selection of ligands with an engineered binding paratope for a target of interest.[96-99] Fibronectin domains had never been applied to EpCAM binding; however, we maintained that their ability to evolved for high affinity and specificity, small size, ease of

production, and amenability to downstream engineering could provide an advantage over these previously established ligands. Therefore, we sought to engineer Fn3 domains with high affinity and specificity for cellular EpCAM using yeast surface display. This study details the inception of these ligands and their further development toward a variety of fundamental, diagnostic, and therapeutic applications.

RESULTS AND DISCUSSION

Affinity Maturation Of EpCAM-Binding Fibronectin Domains

A naïve library of hydrophilic Fn3 sequences[98] was displayed on the surface of yeast and subject to directed evolution via iterative rounds of phenotypic selection and mutagenic diversification.[96] The library used in this campaign incorporated a sitewise constraint of diversity, a strategy that had been recently shown to enhance the efficient selection of high-affinity binders.[100] In addition to the loop length diversity incorporated into the initial library, selected populations were further diversified using error-prone polymerase chain reaction (PCR) and paratope loop shuffling via homologous recombination.[97]

A population of EpCAM-selective Fn3 domains was initially selected through a combination of magnetic bead sorting and fluorescence activated cell sorting (FACS) using soluble EpCAM extracellular domains. While clones isolated via this approach bound well to the recombinant target, they exhibited little affinity for EpCAM-expressing cells (**Figure 2**). In an effort to isolate clones whose binding efficacy translated to cellular protein, an early sub-library that had been partially enriched against the soluble EpCAM domains was panned against adherent monolayers of EpCAM-expressing mammalian cell lines (MCF-7 and LNCaP).[101] An EpCAM-negative cell line, U87-MG, was used as an internal control for non-specific enrichment. After several rounds of panning, clones

that bound selectively to the EpCAM-positive cell lines were isolated. Despite two rounds of mutagenic affinity maturation, the cell-binding clones exhibited only modest binding constants in screens against the soluble EpCAM extracellular domains (K_d values ranging from 130 – 190 nM) and very weak binding to EpCAM-expressing cell lines (**Figure 3**). We hypothesized that the continual enrichment/persistence of clones with only moderate EpCAM affinity was due to the high avidity between the Fn3-displaying yeast cells and the EpCAM-overexpressing mammalian cells. Therefore, we sought to isolate higher affinity clones from the population using a recently developed approach for avidity reduction in the context of mammalian cell panning.[102]

Ligands are tethered to the yeast surface through a pair of disulfide bonds between the yeast mating proteins agglutinin 1 (Aga1p) and agglutinin 2 (Aga2p). Our collaborators hypothesized and demonstrated that, by treating the yeast with the reducing agent dithiothreitol (DTT), they could reduce a proportion of these disulfide linkages and reduce the valency of the displayed Fn3 domains in a controllable and titratable fashion (**Figure 4**).[102] In a model system of EGFR-binding Fn3 domains,[101] they were able to selectively enrich a high-affinity (K_d = 2 nM) clone from a population composed primarily of medium (K_d = 17 nM) and low (K_d >600 nM) affinity clones by reducing the yeast valency to between 6,000 – 3,000 Fn3s per yeast cell prior to panning against the mammalian cell monolayers.[102] Based upon these encouraging results, we then applied this methodology to our EpCAM-expressing cellular selections in an attempt to isolate higher-affinity clones. To test whether the avidity reduction approach would work outside of the model system, the sub-library was also panned against the EpCAM-positive cells under standard conditions in parallel.

Ultimately, three rounds of mutagenesis and selection were carried out to seek improved affinity. At this stage, three populations of EpCAM-binding Fn3 domains were compared: (1) an enriched pool of Fn3s obtained after three rounds of selection with avidity reduction (matured population with DTT); (2) a population from the same round of directed evolution sorted by standard cell panning methods (matured population without DTT); and, (3) the population from the previous round of directed evolution (unmatured population). Soluble Fn3 domains from each population were produced as a polyclonal mixture (**Figure 5A**) and tested for binding to EpCAM positive MCF-7 cells (**Figure 6A**). For analysis of this data, binding is considered detectable for all events with fluorescence above the 95th percentile of the negative control. Binding is considered strong for events lying 2-fold above the 95th percentile of the negative control (**Figure 6B**). The unmatured population contains 15 ± 3% detectable binding events and 3 ± 1% strongly binding events. Upon mutagenesis and additional cell panning, the matured population distribution shifts to include more variants with stronger binding to MCF-7 cells, with 91 ± 4% of events detectable and 55 ± 11% appearing strong. When the mutated population is instead panned using yeast valency reduction with DTT, the resulting variants essentially all bind (99 ± 0.2% of events detectable) and are predominantly strong binders (89 ± 6%). Significantly more strong binders are found in the matured population panned using yeast valency reduction than the matured population panned without DTT treatment ($p = 0.02$).

To further examine this difference in affinity, individual clones from each population were selected based on differences observed in individual sequences obtained from Sanger sequencing of random clones. A subset of these clones were produced as soluble, monoclonal domains and purified (**Figure 5B**). Affinities of these clones were determined by flow cytometry (**Figure 6C**). As shown, the affinities of clones isolated

from the matured population with DTT (median: 24 nM) were significantly higher ($p = 0.04$) than those of clones isolated from the matured population without DTT (median: 1,600 nM). Furthermore, these higher affinity clones are comparable to a commercially available monoclonal antibody known to target EpCAM (clone 9C4) when tested in parallel in a flow cytometry based cell binding assay (**Figure 7**). Importantly, none of the tested clones bind appreciably to EpCAM-negative U87 cells (**Figure 6D**). While all isolated clones appear to be from the same family based on upstream convergence of the lead polypeptide, four out of five of the clones tested from the matured population with DTT show a P87L/S mutation that may be beneficial for stronger binding (**Figure 8**). This mutation could allow for increased flexibility directly C-terminal to the engineered FG loop, enabling a more favorable conformation of the loop. Alternatively, the L/S residue itself may directly contribute as part of the binding paratope as loop-adjacent residues have been shown to in the past.[97, 103, 104] This structure/function determination is an outstanding point for further study.

Designed Single Cysteine Mutants of EpCAM-Binding Fibronectin Domains

Having developed the EpCAM-binding Fn3 domains, we sought to marry them with a number of downstream applications via direct conjugation to a variety of small molecule cargo (e.g., radiochelators, biotin, etc.). Though many options for conjugating proteins to substrates exist,[105] the lack of any natural cysteine residues in the Fn3 scaffold creates a unique opportunity for facile bioconjugation. We hypothesized that, by introducing a single cysteine mutation at a strategic location in the Fn3 framework, we could site-specifically conjugate a variety of cargo to the protein through sulfhydryl reactive chemistry without significantly affecting the ligand's stability or binding affinity.

Single cysteine mutants of non-antibody protein scaffolds have been explored extensively.[106-111] Most notably, Goldberg, *et al.* of Janssen R&D recently performed a "cysteine scan" of their fibronectin-based Centyrin scaffold, wherein they individually mutated each position in the Centyrin to a cysteine and evaluated the resulting ligands in terms of expression yield, target binding, and conjugation capabilities.[111] Ultimately, they identified 26 positions deemed suitable for cysteine mutation and subsequent conjugation.

However, the backbone of the Centyrin scaffold differs slightly from the hydrophilic Fn3 framework we utilized.[98] In order to identify which of the 26 mutatable positions may be applicable to our scaffold, we aligned the Centyrin sequence to that of anti-EpCAM Fn3 clone C5[102] (**Figure 8**). As shown, the alignment identified two homologous amino acid regions: LTVPGS and GLKPG. The LTVPGS sequence extends into the paratopic BC loop; because this loop is suspected to be highly important for binding,[94] cysteine mutation and conjugation within this region was likely to be detrimental. The GLKPG motif, however, is located within the EF loop, which is positioned on the opposite face of the Fn3 relative to the binding paratope (**Figure 1**).

Of the five amino acids in the GLKPG motif, Goldberg and colleagues identified both of the glycine residues (called G61 and G65 based upon their position in the Centyrin scaffold) as sites amenable for cysteine mutation.[111] Relative to a mutant with a cysteine residue added to the C-terminus of the Centyrin, these mutations: (1) did not reduce protein expression in *E. coli*; (2) did not reduce the affinity of the ligand for the target protein; (3) demonstrated >80% conjugation efficiency to the tubulin inhibitor monomethyl auristatin F (MMAF); (4) possessed melting temperatures ≥66 ºC; (5) exhibited reversible denaturation; and (6) demonstrated *in vitro* efficacy in cytotoxicity

assays (IC_{50} values ranged from 0.5 – 1.5 nM). Colloquially, the K63 residue in this motif is also amenable to mutation; however, this position was not identified in the Janssen R&D screen and we did not evaluate it further.

Based upon these results, we hypothesized that there are at least three potential positions for cysteine mutation in our Fn3 clone C5 – G61C, G65C, and the C-terminus. Of the two glycine mutations, the data by Goldberg, *et al.* suggested that G65C was superior to G61C in every category.[111] Therefore, G65C was prioritized over G61C, and we proceeded to produce G65C and C-terminal cysteine mutants of Fn3 clone C5.

Site-directed mutagenesis was used to perform the cysteine substitution (G65C) and insertion (C-terminus) at the desired locations. PCR using mutagenic primers (**Table 1**) and Fn3 clone C5 in the Novagen pET28a(+) vector as the template yielded the desired sequences. Plasmids encoding each of the mutant sequences were transformed into *E. coli* and expressed. Notably, both the G65C and C-terminal mutants were successfully expressed in the soluble fraction of bacterial cell lysates in yields comparable to the parent clone; however, the Fn3 C5 G65C ligand was prioritized at this stage and only this clone was further purified as a soluble, monomeric ligand (**Figure 10A**). To serve as a relevant control ligand in future studies, a non-targeted Fn3 domain (clone NT) housing the same G65C mutation was also expressed and purified in an analogous fashion (**Figure 10B**).

EpCAM-Binding Fibronectin Domains for Diagnostic Cancer Imaging

Compared to antibodies, alternative protein scaffolds are uniquely suited for diagnostic imaging of solid malignancies as their small size facilitates tumor penetration and rapid renal clearance, both of which contribute to an improved signal-to-background ratio.[112]

Accordingly, we sought to evaluate the ability of the EpCAM-binding Fn3 domains to selectively localize within EpCAM-expressing xenograft tumors using positron emission tomography (PET) imaging.

The radiochelator NODAGA (1,4,7-triazacyclononane-1-glutaric acid-4,7-diacetic acid) was chosen for these studies as it had been shown to chelate copper-64 (^{64}Cu) at room temperature[113] and exhibit less *in vivo* leeching of the chelated ^{64}Cu *in vivo*[114] compared to the popular radiochelator, DOTA (1,4,7,10-tetraazacyclododecane-1,4,7,10-tetraacetic acid). NODAGA was site-specifically conjugated to the lone cysteine residue in Fn3 clone C5 and the non-targeted control clone Fn3 NT using sulfhydryl/maleimide chemistry (**Figure 11**). Purified reaction products were analyzed by SEC (**Figure 12**), and conjugation was verified using matrix-assisted laser desorption/ionization mass spectroscopy (MALDI-MS) with efficiencies of up to 93% (**Figure 13**).

To assess whether conjugation to the cysteine had impacted the scaffold's EpCAM-binding affinity and specificity, the NODAGA-conjugated ligands were titrated against EpCAM-expressing MCF-7 cells and EpCAM-negative U87-MG cells via flow cytometry. The NODAGA-C5 conjugate retained its affinity for EpCAM with a K_d value of 14 ± 3 nM (compared to 17 ± 1 nM reported for the parent clone[102]) and exhibited no off-target binding to the U87-MG cells (**Figure 14**). Importantly, the NODAGA-NT control ligand bound to neither cell line (**Figure 14**). Furthermore, the impact of NODAGA conjugation on the folded protein structure was assessed by circular dichroism (CD). Consistent with the binding data, conjugation did not alter the β-sheet composition of the folded Fn3 scaffolds, with the CD spectra for the conjugated ligands closely matching those for the unlabeled parent clones (**Figure 15**).

Having developed the cysteine mutants and characterized the NODAGA-Fn3 conjugates, we then assessed the ability of these ligands to accumulate within EpCAM-positive xenograft tumors. Eight-week-old female NSG (NOD.Cg-*Prkdc*^{scid} *Il2rg*^{tm1Wjl}/SzJ) mice were inoculated with two shoulder tumors each, an EpCAM-expressing MCF-7 xenograft on the left and an EpCAM-negative U87-MG xenograft on the right. Following a two-week engraftment period, mice received a tail vein injection of 40 – 60 μCi NODAGA-Fn3 conjugate chelated to ^{64}Cu in 100 mM sodium acetate buffer. Mice were imaged via combined PET/CT (computed tomography) at 45 min and 120 min post-injection. Mice were euthanized immediately after the 120 min imaging session, and ligand biodistribution was assessed by *ex vivo* tissue gamma counting.

Unfortunately, the EpCAM-binding Fn3 domain failed to significantly accumulate within the MCF-7 xenograft (**Figure 16**). Rather, the majority of the ligand accumulated within the kidneys, liver, and spleen. In contrast, the non-targeted Fn3 domain was nearly entirely localized to the kidney, consistent with the predominant renal clearance of these small (~12 kDa), non-antibody scaffolds.[112] When the experiment was repeated using freshly produced batch of protein conjugates, similar results were obtained.

The observed differences between the EpCAM-targeted and non-targeted ligands may be explained by several factors. First, directed evolution to yield high-affinity binders is often associated with a decrease in ligand stability.[103] It is possible that the more highly evolved, EpCAM-binding Fn3 is less stable to *in vivo* conditions than the nearly wild-type non-targeted Fn3, causing it to aggregate into higher ordered species upon injection. This could explain the observed shift away from renal distribution toward the liver and spleen, as these organs are members of the mononuclear phagocytic system (MPS; also known as the reticuloendothelial system) and play a role in the metabolic clearance

of species too large to be filtered by the renal glomerular apparatus.[115] An alternative hypothesis is that the EpCAM-binding Fn3 clones exhibit some degree of cross-reactivity with murine EpCAM or another antigen with a serendipitously similar epitope. However, a multivalent scaffold incorporating these anti-EpCAM Fn3 domains failed to bind to the murine EpCAM-expressing mammary epithelial cell line, HC11, arguing against human/mouse EpCAM cross-reactivity (**Figure 17**). Lastly, it is possible that a yet unidentified ligand expressed *in vivo* is capable of binding to the anti-EpCAM Fn3 domains, sequestering them in certain tissues. Though the targeted and non-targeted Fn3 domains share 80% identity by sequence alignment, the mutations in the evolved ligand could have created a unique epitope that accounts for the disparate distribution between the scaffolds. This possibility is currently being evaluated using immunohistochemistry (IHC), exposing Fn3 clone C5 to a macroarray of mouse tissues.

CONCLUSIONS

Non-immunoglobulin scaffolds are attractive alternatives to antibodies due to their distinct biophysical properties. We developed the first Fn3 domains that bind to the carcinoma and cancer stem cell marker, EpCAM. A combination of magnetic-associated recombinant antigen sorting and mammalian cell panning were used to select desirable clones from a yeast-displayed library. High-affinity ligands were enriched in the late cell panning selections using a recently developed avidity-reduction technique[102], enabling the isolation of Fn3 domains with K_d values of 11-30 nM and robust selectively for cellular EpCAM. Notably, the sub-population that yielded these clones was never subject to an additional round of mutagenic affinity maturation, suggesting that ligands with even lower K_d values could be obtained through further directed evolution.

The epitope recognized by these domains remains unknown, as it does not compete for EpCAM binding with either the MOC31 or 9C4 monoclonal antibodies by flow cytometry. Epitope elucidation remains a point for further study, and could be assessed through crystallography or high-throughput screening against a panel of characterized monoclonal antibodies using biolayer interferometry.

The EpCAM-binding Fn3s were further developed as potential PET imaging agents for carcinomas. A single cysteine residue was substituted for glycine 65 without detrimental effects on protein expression. The lone sulfhydryl group was subsequently used for site-specific labeling with a NODAGA-maleimide species, and this conjugation had no impact on protein folding or EpCAM binding. Despite favorable *in vitro* characterization, the NODAGA-Fn3 conjugates failed to accumulate within EpCAM-expressing xenograft tumors in mice. Explanations for this paradoxical behavior are being explored.

Peripheral work in the Wagner laboratory has explored the use of these Fn3 ligands in other contexts. In one embodiment, the Fn3 C5 G65C mutant was site-specifically conjugated to biotin-maleimide and loaded onto a chemically self-assembled nanoring (CSAN) displaying both monovalent streptavidin (mSA^{116}) domains and anti-CD3 scFvs. T cells armed with these EpCAM/CD3 bispecific CSANs were selectively activated in the presence of EpCAM-expressing target cells, as measured by the release of the cytokine, interleukin 2 (IL-2). This data indicates that, while the epitope recognized by the Fn3 domains is yet unknown, the binding site is suitable to trigger T cell signaling; therefore, these may be useful for creating T cell directing immunotherapies. In a second application, several parent Fn3 clones were non-specific biotinylated using NHS chemistry with no significant change in their measured K_d values. As non-specific conjugation is often more convenient that site-specific labeling endeavors, these results

may increase the accessibility of these Fn3 ligands for a wide variety of applications, including fluorescent labeling, surface functionalization, and *in vitro* pull down assays.

MATERIALS AND METHODS

Cells and Cell Culture

MCF-7, LNCaP, and U87-MG cell lines were purchased from ATCC. MCF-7 and U87-MG cells were grown at 37 °C in a humidified atmosphere with 5% CO_2 in Dulbecco's modified Eagle's medium (DMEM) with 4.5 g/L glucose, sodium pyruvate, and glutamine supplemented with 10% (v/v) fetal bovine serum (FBS) and 1% (v/v) penicillin streptomycin. LNCaP cells were grown at 37 ºC in a humidified atmosphere with 5% CO_2 in Roswell Park Memorial Institute (RPMI) medium supplemented identically.

Yeast surface display was performed essentially as described.[96] EBY100 yeast harboring expression plasmids were grown in SD-CAA medium (16.8 g/L sodium citrate dihydrate, 3.9 g/L citric acid, 20.0 g/L dextrose, 6.7 g/L yeast nitrogen base, 5.0 g/L casamino acids) at 30 °C with shaking at 250 rpm. Protein expression was induced by transferring yeast cells in logarithmic phase ($OD_{600} < 6$) into SG-CAA medium (10.2 g/L sodium phosphate dibasic heptahydrate, 8.6 g/L sodium phosphate monobasic monohydrate, 19.0 g/L galactose, 1.0 g/L dextrose, 6.7 g/L yeast nitrogen base, 5.0 g/L casamino acids) and growing at 30 °C with shaking at 250 rpm for at least 8 h. EBY100 without plasmid were grown in YPD medium (10.0 g/L yeast extract, 20.0 g/L peptone, 20.0 g/L dextrose) at 30 °C with shaking at 250 rpm.

Expression Plasmids

The pCT-40 plasmid[101] was used as the expression vector for yeast surface display. This vector encodes for Aga2p followed by an 80-amino acid linker – including a factor Xa

cleavage site, a hemagglutinin (HA) epitope, a 40-mer linker with two repeats of the PAS#1 peptide,[117] and a glycine-rich peptide – followed by the fibronectin domain with a C-terminal MYC epitope.

Ligand Reduction with DTT Titration

$5x10^6$ yeast displaying fibronectin clones in pCT-40 vector were pelleted at 8,000g and washed twice with 10 mM Tris buffer pH 7.5 (1.24 g/L Tris-HCl, 0.26 g/L Tris base). DTT was diluted to 0.5, 5, 10, 15, and 20 mM in 10 mM Tris buffer pH 7.5. Yeast were resuspended in 20 µL DTT solution and incubated at 30 °C for 20 min without shaking. Yeast were then pelleted at 8,000g and washed twice with PBSACM (PBS with 1 g/L bovine serum albumin, 1 mM $CaCl_2$, 0.5 mM $MgCl_2$). To quantify relative ligand expression, yeast were labeled with 20 µL anti-MYC primary antibody (9E10, BioLegend, Cat: 626802, 5 µg/mL) for 20 min at room temperature, then washed once with PBSACM and pelleted at 8,000g for 1 min. Yeast were then labeled with 20 µL goat anti-mouse Alexa Fluor 647 conjugate (Thermo Fisher Scientific, Cat: A-21235, 10 µg/mL) and analyzed by flow cytometry using a BD Accuri C6. The average fluorescence of 10,000 events from each sample was compared to an untreated control.

To fully quantify the absolute expression of each ligand without DTT treatment, labeled yeast fluorescence was compared to a calibration curve prepared from anti-mouse IgG beads (Bangs Laboratories, Inc., Cat: 815). Polystyrene beads with known quantities of immobilized monoclonal anti-mouse IgG were labeled with 20 µL mouse anti-MYC antibody (9E10, BioLegend, Cat: 626802, 5 µg/mL) and incubated for 20 min at room temperature. Beads were washed once with PBSACM and pelleted at 2,500g for 2.5 min. The beads were then labeled with 20 µL goat anti-mouse Alexa Fluor 647 conjugate (10 µg/mL) for 20 min at room temperature. Beads were again washed with PBSACM

and pelleted at 2,500g for 2.5 min. Concurrently, yeast expressing fibronectin clones in pCT-40 vector were labeled equivalently with mouse anti-MYC and goat anti-mouse Alexa Fluor 647 conjugate as described above. Yeast were labeled concurrently with 20 µL goat anti-MYC FITC conjugate (Bethyl Laboratories, Cat: A190-104F, 2 µg/mL for 20 min at room temperature. Yeast were washed and pelleted at 8,000g for 1 min. Fluorescence was analyzed with a BD Accuri C6. The standard curve was compared to the fluorescence of the yeast that were labeled with the same mouse anti-MYC antibody and goat anti-mouse Alexa Fluor 647 conjugate.

Yeast Surface Display Cell Panning with Avidity Reduction

Yeast populations were washed twice with 10 mM Tris pH 7.5 and pelleted at 8,000g for 1 min. Yeast were resuspended in 800 µL 10 mM Tris buffer pH 7.5 with 0, 2.5, 5, 10, or 15 mM DTT and incubated at 30 °C for 20 min without shaking, then washed twice with PBSACM and pelleted at 8,000g for 1 min.

Target mammalian cells were grown to approximately 80% confluence in 12-well plates. Culture medium was removed via aspiration and cells were washed three times with 500 µL ice cold PBSACM. Then, $5x10^7$ yeast in 500 µL ice cold PBSACM were applied to the mammalian cell monolayers dropwise and incubated at 4 °C static for 2 hours. Cells were washed 5 times with 500 µL PBSACM as described.[101] Briefly, cells were tilted 25 times and rotated 5 times for the first four washes and rotated 10 times only for the fifth wash. SD-CAA media (500 µL) was added dropwise to each washed well, and cells were recovered by scraping. Recovered yeast were grown overnight in 5 mL SD-CAA at 30 °C with shaking at 250 rpm and protein expression was induced by transferring yeast into SG-CAA media and incubating for at least 8 hours at 30 °C, 250 rpm. Clone composition is not expected to change due to propagation under non-induced

conditions, as previously shown for this vector family.[118] Final mixture compositions were determined by flow cytometry analysis using a BD Accuri C6, as described above.

Affinity Selection of EpCAM-Binding Engineered Fibronectin Domains

EpCAM-binding fibronectin domains were selected via yeast surface display essentially as described.[96] Details regarding yeast cell growth and induction of ligand surface display are given above. Briefly, a yeast-display library of fibronectin domains[100] was subjected to negative selection against avidin-coated magnetic beads followed by magnetic beads functionalized with the irrelevant protein lysozyme to remove any non-specific binding interactions. Remaining yeast were then exposed to magnetic beads functionalized with biotinylated recombinant human EpCAM (Acro Biosystems, Cat: EPM-H8223) and bound yeast were selected. Incubations were performed at 4 ºC and recovered beads were washed once in PBSA (PBS with 1 g/L bovine serum albumin) prior to culture in SD-CAA media at 30 ºC, 250 rpm for at least 12 hours. Protein induction was then induced as described above.

After three rounds of magnetic selection, full-length (MYC positive) fibronectin clones were selected via FACS using mouse anti-MYC antibody (9E10, BioLegend, Cat: 626802, 5 µg/mL) and goat anti-mouse Alexa Fluor 647 conjugate (Thermo Fisher Scientific, Cat: A-21235, 10 µg/mL). Isolated clones were subject to whole-gene and loop-focused error-prone PCR using mutagenic nucleotide analogs[119] and genetic loop shuffling between sequences.[97] After transformation of the mutants into EBY100 yeast, the resulting population was subject to one additional round of magnetic selection at 4 ºC; recovered beads were washed twice with PBSA prior to culture in SD-CAA media at 30 ºC, 250 rpm for at least 12 hours. Ligand expression was induced as above. Yeast were then subject to two rounds of mammalian cell selections against adherent

monolayers of the EpCAM-overexpressing cell lines MCF-7 and LNCaP, as previously described.[101] Full length clones that bound biotinylated target, detected with a streptavidin Alexa Fluor 488 conjugate (Thermo Fisher Scientific, Cat: S-11223, 10 μg/mL), were then isolated via FACS and diversified as before.

After three additional rounds of panning against MCF-7 and LNCaP cell lines, target binding yeast were again isolated by FACS and diversified before panning against the same cell lines once more. This population was then subjected to three rounds of cell panning against MCF-7 cells in two parallel strategies: via the standard approach outlined above or with yeast valency reduction. In the case of the standard approach, yeast were panned against MCF-7 cells without DTT treatment. For yeast valency reduction, yeast were treated with 2.5, 5, 7, and 9 mM DTT and washed as previously described. Valency was assessed by flow cytometry analysis with comparison to fluorescence bead standards, as described above. The DTT treatment yielding a population with between 3,000 and 6,000 ligands per yeast cell (often 2.5-5 mM, depending on the untreated level of protein expression) was used for selection.

Protein Production and Characterization

BL21(DE3) *Escherichia coli* (New England Biolabs, Cat: C2566I) were transformed with plasmid and grown overnight (37 ºC, 250 rpm) in lysogeny broth (LB) medium with kanamycin (50 μg/mL). Approximately 4 mL of overnight culture was added to 100 mL LB medium without antibiotics, grown at 37 ºC, 250 rpm until the optical density at 600 nm (OD_{600}) reached 0.65 – 1.0 (approximately 2 h), and induced with 1.0 mM isopropyl β-D-1-thiogalactopyranoside (IPTG) for 3 h at 30 ºC, 250 rpm. Cells were pelleted (3,500g, 15 min, 4 ºC), frozen in a dry ice/ethanol bath, and resuspended in 8 mL SoluLyse protein extraction reagent (Genlantis Inc., Cat: L100125) supplemented with

EDTA-free protease inhibitor (Thermo Fisher Scientific, Cat: 88266). Cell lysates were centrifuged (27,000g, 15 min, 4 ºC) to separate soluble and insoluble protein fractions, and the supernatant was filtered through a 0.22 µm membrane. Fibronectin domains were purified by immobilized metal affinity chromatography on a gravity column packed with HisPur cobalt resin (Thermo Fisher Scientific, Cat: 89964) following the manufacturer's protocol, and eluted fractions were analyzed by SDS-PAGE. Fractions containing visibly pure fibronectin domains were pooled and buffer exchanged into phosphate buffered saline (PBS), pH 7.4, with Zeba spin desalting columns (Thermo Fisher Scientific, Cat: 89893). Protein concentration was determined via Bradford Protein Assay (Bio-Rad Laboratories, Cat: 500-0201). Purified protein was analyzed by size-exclusion chromatography (SEC) on a Superdex 200 Increase 10/300 gel filtration column (GE Healthcare Life Sciences, Cat: 28990944) in PBS running buffer. Retention times of fibronectin domains were compared to those of commercial molecular weight standards (Sigma Aldrich, Cat: C7150 and C7025, respectively) cytochrome C (14.6 kDa) and carbonic anhydrase (29 kDa) and found to be ≥80% monomeric.

Affinity Determination of Fibronectin Domains

MCF-7 cells were cultured to approximately 80% confluence, as described above. Detached MCF-7 cells were counted using a Countess II Automated Cell Counter. Aliquots of 40,000 cells were washed and labeled with varying concentrations of each fibronectin clone for 90 min at 4 °C with rotation. Cells were pelleted at 300g for 3 min and washed with 1 mL ice cold PBSACM, then labeled with 20 µL anti-His^6 FITC conjugate (Abcam, Cat: ab1206, 13 µg/mL) for 20 min at 4 °C in the dark. Cells were again pelleted and washed with 1 mL ice cold PBSACM. Fluorescence was analyzed using a BD Accuri C6 or BD LSRII.

Quantification of EpCAM Expression for Mammalian Cell Lines

Cells were grown to approximately 80% confluence as described above and detached with non-enzymatic cell dissociation buffer (Thermo Fisher Scientific, Cat: 13151014). Cells were aliquoted to $1x10^6$ cells/sample, pelleted (300 g, 5 min), and washed with 1 mL ice cold PBSA. Cells were labeled with 50 µL mouse anti-human EpCAM monoclonal antibody (clone MOC31, Abnova, Cat: MAB13332, resuspended to 1 µM in PBSA) on ice for 30 min, washed once in 1 mL PBSA, and then labeled with 50 µL goat anti-mouse Alexa Fluor 647 conjugate (1:200 dilution) in the dark on ice for 20 min. Cells were then washed three times with 1 mL PBSA before immediate analysis on a BD LSR II. EpCAM expression was quantified by comparing the mean fluorescence intensity to a calibration curve from concurrently analyzed anti-mouse IgG beads (Bangs Laboratories, Inc.) prepared as described above.

Affinity Estimation for Yeast Displayed Ligands

Clones isolated from a population matured without DTT were grown overnight in SG-CAA media at 30 ºC to induce fibronectin display. After induction, $1x10^6$ yeast were pelleted (2,000 rcf, 2 min), washed with 1 mL PBSA, and resuspended in 50 µL of biotinylated antigen in PBSA at various concentrations (0-1,000 nM) plus 1 µL 9E10 (1:4 dilution, BioLegend). Yeast were labeled at 4 ºC for ≥18 h, pelleted, washed with 1 mL PBSA, and labeled with 50 µL streptavidin Alexa Fluor 488 conjugate plus goat anti-mouse Alexa Fluor 647 conjugate (1:200 dilution each, Thermo Fisher Scientific) for 20 minutes at 4 ºC in the dark. After a final wash in 1 mL PBSA, samples were analyzed on a BD LSR II. Mean fluorescence intensities were fitted to a nonlinear regression binding model assuming a single binding site (GraphPad Prism).

Comparison of Anti-EpCAM Fibronectin Clones and Monoclonal Antibody 9C4

Soluble anti-EpCAM fibronectin domains were produced and purified as described above. Detached MCF-7 cells ($1x10^5$ cells/sample) were washed with ice cold PBSA, pelleted at 500 g for 5 min, and then resuspended in 100 µL of either 100 nM soluble fibronectin clone or PBSA (for 9C4 samples and negative control samples). Samples were incubated at 4 ºC for 30 min before pelleting at 500 g for 5 min and discarding the supernatant. Cells were then resuspended in either: (1) 100 µL anti-polyhistidine monoclonal antibody conjugated to Alexa Fluor 647 (Invitrogen, Cat: MA1-135-A647) for fibronectin clone samples and negative control samples, or (2) 100 µL anti-EpCAM monoclonal antibody 9C4 conjugated to Alexa Fluor 647 (BioLegend, Cat: 324212). Samples were incubated at 4 ºC in the dark for 30 min, pelleted at 500 g for 5 min, and then washed twice with 1 mL PBSA. Pellets were finally resuspended in 500 µL PBSA and analyzed on a BD LSR II flow cytometer.

Site Directed Mutagenesis

Site directed was performed using the New England Biolabs (NEB) Q5 Site-Directed Mutagenesis Kit (Cat: E0554S) according to the manufacturer's protocol. Briefly, designed mutagenic primers (**Table 1**) were used to either insert a *TGT* codon at the C-terminus or perform a *G* to *T* transversion mutation in codon 65 via PCR. EpCAM-binding Fn3 clone C5 in the Novagen pET28a(+) vector (Millipore Sigma, Cat: 69864) was used as the template. PCR was performed using the included Q5 Hot Start High Fidelity Master Mix, 20 ng of template DNA, and 0.5 µM of each 5' and 3' primer. After an initial 30 sec denaturation at 98 ºC, 30 cycles of denaturation (98 ºC for 10 sec), annealing (64 ºC for 30 sec), and extension (72 ºC for 180 sec) were performed. Following a final extension at 72 ºC for 2 min, PCR products were subject to a kinase, ligase, and *DpnI* treatment to circularize the newly synthesized plasmids and digest the

methylated templates (per manufacturer protocol). Plasmids were transformed into competent *E. coli,* and DNA from single colonies was Sanger sequenced to identify correct mutants.

Site-Specific Conjugation of Fibronectin Domains

Tris(2-carboxyethyl)-phosphine HCl (TCEP; 35 mM in PBS, 100 eq) was added to a solution of purified Fn3 domain in PBS (pH 7.4), and the mixture was incubated at room temperature for 1 h with rotation. Then, NODAGA (1,4,7-triazacyclononane-1-glutaric acid-4,7-diacetic acid)-maleimide (CheMatech, Cat: C099) (20 mM in PBS, 100 eq) was added and the mixture was incubated at 4 ºC overnight with rotation. The completed reaction was purified on a PD-10 desalting column (GE Healthcare, Cat: 17085101) in 100 mM sodium acetate buffer (pH 6.0). Site-specific conjugation of biotin-maleimide was performed analogously, using EZ-Link Maleimide-PEG2-Biotin (Thermo Fisher Scientific, Cat: 21901BID) instead of NODAGA-maleimide and purifying in PBS (pH 7.4) instead of sodium acetate buffer. Conjugation was confirmed by matrix-assisted laser desorption/ionization mass spectroscopy (MALDI-MS) performed by the University of Minnesota Center for Mass Spectroscopy and Proteomics (CMSP).

Circular Dichroism

Circular dichroism was performed on a Jasco J-815 Spectropolarimeter. Briefly, 300 µL of 0.5 – 2.0 µM protein sample in PBS was loaded in a quartz cuvette and analyzed at 20 ºC. Data was collected in continuous scanning mode with a rate of 50 nm/min across the range of 260 – 200 nm with a 0.1 nm pitch. Each spectrum is the composite average of ≥5 independent scans.

Copper Chelation and Purification

$^{64}CuCl_2$ (University of Wisconsin, Madison) was diluted with 100 µL of 100 µM sodium acetate buffer, pH 7.0 and pH adjusted using 1M HCl/NaOH. Approximately 3.2 mCi of the ^{64}Cu solution was added to 120 µL of 15-25 µM NODAGA-Fn3 in 100 mM sodium acetate buffer, pH 6.0. The mixture was allowed to incubate at room temperature for 1 h and then purified using a PD-10 column equilibrated with 10 mM sodium acetate buffer, pH 6.0, in order to remove unchelated copper.

Tumor Inoculation

All procedures performed in studies involving animals were in accordance with the ethical standards of the University of Minnesota and approved by the Institutional Animal Care and Use Committee (IACUC). Eight-week-old female NSG (NOD.Cg-*Prkdc*^{scid} *Il2rg*^{tm1Wjl}/SzJ) mice (Jackson Laboratory) were anesthetized with isofluorane (induced at 5% and maintained at 2% in 1 mL/min O_2) and inoculated with $2x10^6$ EpCAM-expressing MCF-7 cells on the left shoulder and $1x10^6$ EpCAM-negative U87-MG cells on the right shoulder, each as a 50% v/v suspension in Matrigel Matrix (Corning, Cat: 354248). Xenografts were allowed to grow for two weeks, yielding tumors of 8-16 mm in diameter. To support MCF-7 cell growth, the mice's water supply was supplemented with 500 µM 17-β-estradiol valerate.

PET Imaging and Biodistribution Analysis

All procedures performed in studies involving animals were in accordance with the ethical standards of the University of Minnesota and approved by the Institutional Animal Care and Use Committee (IACUC). Static PET/CT imaging was performed as previously described.[120] Briefly, mice were anesthetized with isofluorane (induced at 5% and maintained at 2% in 1 mL/min O_2) and tail vein injected with approximately 40-60 µCi of

NODAGA-Fn3 conjugate chelated to ^{64}Cu, as measured by an Atomlab 100 Dosimeter with a setting of 50.2. Five-minute static PET scans were performed at 45 min and 2 h after injection using an Inveon micro-PET/CT (Siemens). The PET energy cutoffs were 350−650 keV with a timing window of 3.438 ns. The PET images were reconstructed with an OSEM2D method using four iterations of Fourier re-binning. PET images were smoothed with a 1x1x1 voxel Gaussian filter. The CT used 340 projections of 80 kV at 500 μA with 200 ms exposure over 384 s of total scan time with an effective pixel size of 98.3 μm. The CT was reconstructed using the Feldkamp algorithm with a Shepp-Logan filter. The preceding methods are included in the Inveon Acquisition Workplace software (Siemens). After imaging, mice were euthanized via cervical dislocation under isofluorane anesthesia. Blood, bone, brain, heart, large intestine, kidneys, liver, lungs, muscle, pancreas, skin, spleen, stomach, tail and tumors were resected, weighed, and had their radioactivity measured by a CRC-25W (Capintec, Inc.) gamma counter averaged over 60 sec.

ACKNOWLEDGEMENTS

This work was funded by the National Institutes of Health R21 EB019518 (BJH), R21 CA185627 (CRW), F30 CA210345 (CMC), T32 GM008244 (CMC), and the University of Minnesota.

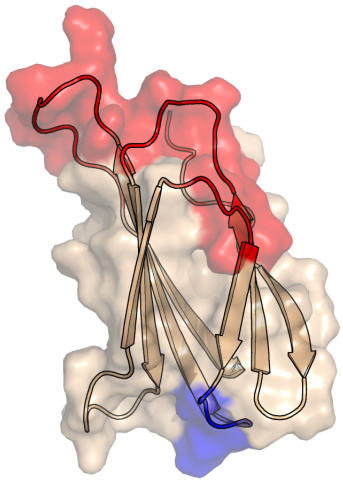

Figure 1. Structure of the Human Tenth Type III Fibronectin Domain (Fn3). Fn3 domains are composed of seven anti-parallel β-sheets (named A through G), each connected by a flexible loop region. Three of these loops – the BC, DE, and FG loops (named for the β-sheets they connect and depicted in red) – form a congruous surface on one face of the protein. The amino acid residues comprising this region can be mutated or evolved to form a binding paratope for a target of interest without significantly affecting the overall structure and stability of the scaffold. Additionally, the EF loop (blue) is located on the opposite face of the protein and contains an amino acid motif (GLKPG) that has also been demonstrated (in this work and others[111]) to be amenable to minor mutations, primarily single-residue substitutions to cysteine.

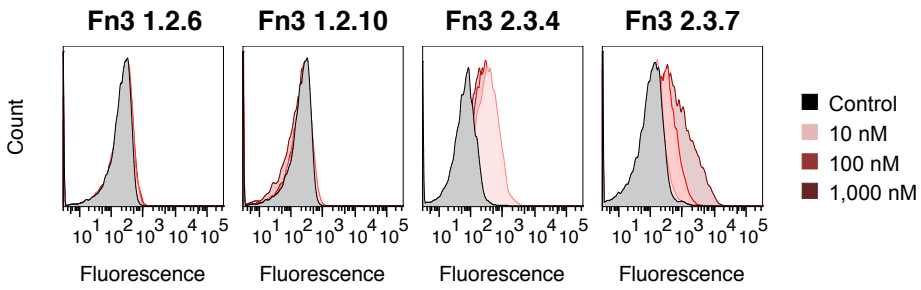

Figure 2. Fibronectin Clones Selected Against Recombinant EpCAM Extracellular Domains Bind Poorly to EpCAM-Expressing Mammalian Cells. Four Fn3 clones from two populations selected against the recombinantly-produced, biotinylated EpCAM extracellular domains were expressed and purified as soluble, monomeric ligands. They were then assessed for their ability to bind to EpCAM-positive MCF-7 cells via flow cytometry, as described above. (A & B) Clones from an early population subject to only a single round of affinity maturation are incapable of binding to EpCAM-positive cells. (C & D) An additional round of affinity maturation yields detectable but modest binding events.

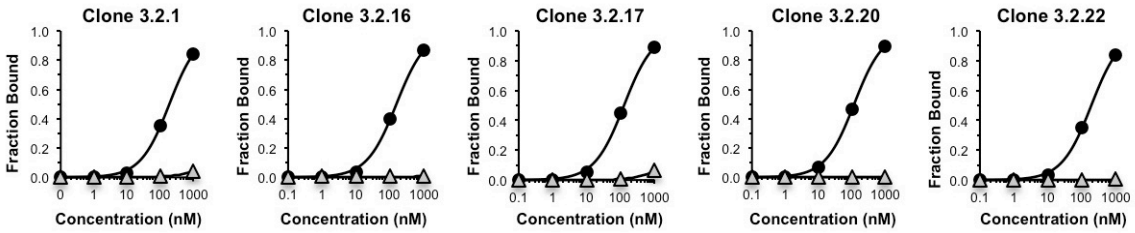

Figure 3. Affinity Estimations for Intermediate EpCAM-Binding Fibronectin Clones. The affinity of yeast-displayed clones from the population matured without DTT towards soluble EpCAM ectodomain (black circles) was assessed via flow cytometry, as described above. Dissociation constants (K_d) were obtained by fitting the mean fluorescence intensity values to a nonlinear regression model assuming a single binding site. For this scouting experiment, all clones were titrated only once and are portrayed as estimates without error. Estimated K_d values ranged from 120 nM to 190 nM. Notably, no clones possessed measurable affinity for the irrelevant soluble CD3 ectodomain (gray triangles).

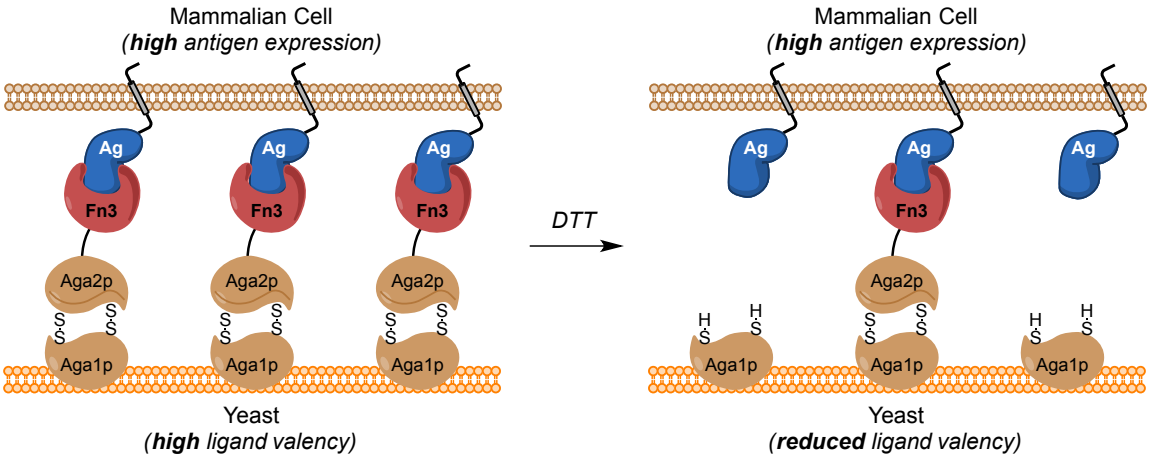

Figure 4. Schematic of Yeast Valency Reduction with Dithiothreitol. Yeast populations typically express 8,000 – 10,000 ligands per cell.[102] When panned against mammalian cell monolayers that overexpress an antigen of interest, the high avidity between the yeast and mammalian cell enables ligands with only a modest affinity for the antigen to survive the selection process, hindering the isolation of high-affinity clones. Reducing the disulfide linkages that tether the Fn3 domains to the yeast surface using DTT lowers the avidity of the cellular interactions, and hinders the ability of weaker clones to persist throughout the cell panning selection. Ultimately, this facilitates the isolation of clones with higher affinity for the target antigen.

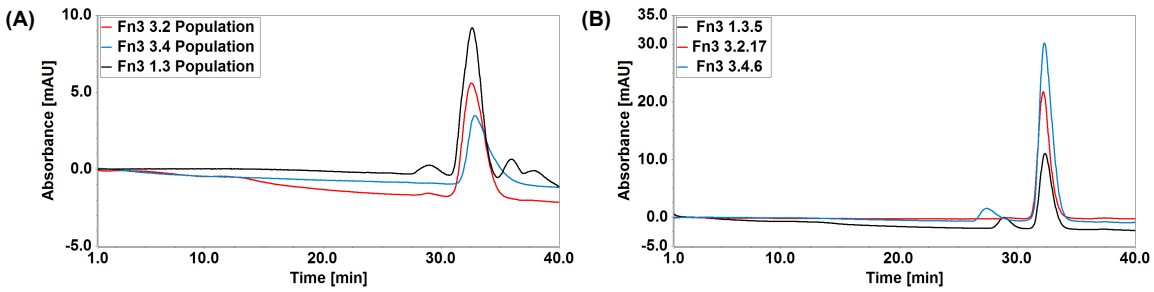

Figure 5. SEC Characterization of Soluble EpCAM-Binding Fibronectin Domains. Soluble Fn3 domains were expressed, purified, and analyzed via SEC as described above. (A) The three soluble fibronectin populations are compared (unmatured in black; matured without DTT in red; matured with DTT in blue). (B) One representative clone from each population (unmatured in black; matured without DTT in red; matured with DTT in blue) is compared. All retention times were compared to the commercial molecular weight standards cytochrome C (14.6 kDa) and carbonic anhydrase (29.0 kDa), and peak integration confirmed that all clones/populations are ≥80% monomeric.

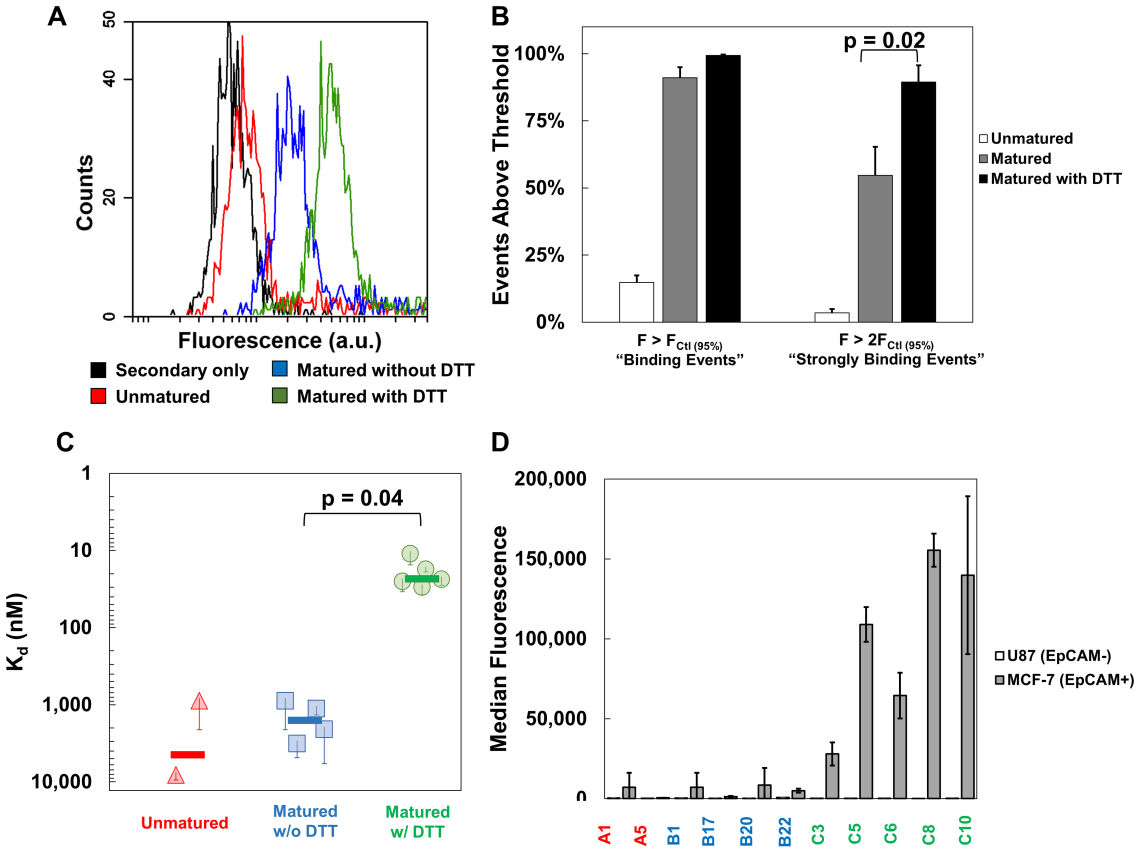

Figure 6. Characterization of EpCAM-Binding Fibronectin Populations and Individual Clones. (A) Polyclonal populations of soluble EpCAM-binding fibronectin domains were assessed for relative affinity against EpCAM-expressing MCF-7 cells at 10 nM via flow cytometry. (B) Quantitative analysis of the flow cytometry experiments was performed. For this analysis, the percentage of fluorescent events appearing above the 95th percentile ("binding events") and 2-fold above the 95th percentile ("strongly binding events") of the negative control were quantified as mean ± standard error of 8 trials. (C) Individual fibronectin clones were produced solubly, and their affinity towards EpCAM-expressing MCF-7 cells was determined by flow cytometry. Affinities are presented as mean ± standard error of 2-5 trials (instances where only two trials were performed are presented as mean ± range). (D) The same soluble fibronectin clones were assessed for binding against EpCAM-negative U87 cells at 100 nM via flow

cytometry to determine the specificity of these clones. Clones are named with letters corresponding to the population from which they were isolated: “A” denotes clones isolated from the unmatured population, “B” denotes clones isolated from the population matured without DTT, and “C” denotes clones isolated from the population matured with DTT. The coloring of clone names further represents their parent population, akin to **Figures 6A and 6C**. Median fluorescence intensities are presented as mean ± standard error of 2-5 trials (instances where only two trails were performed are presented as mean ± range). All samples include U87 (EpCAM-negative) data, but most U87 bars (white) are not visible because of their near-zero fluorescence after background correction.

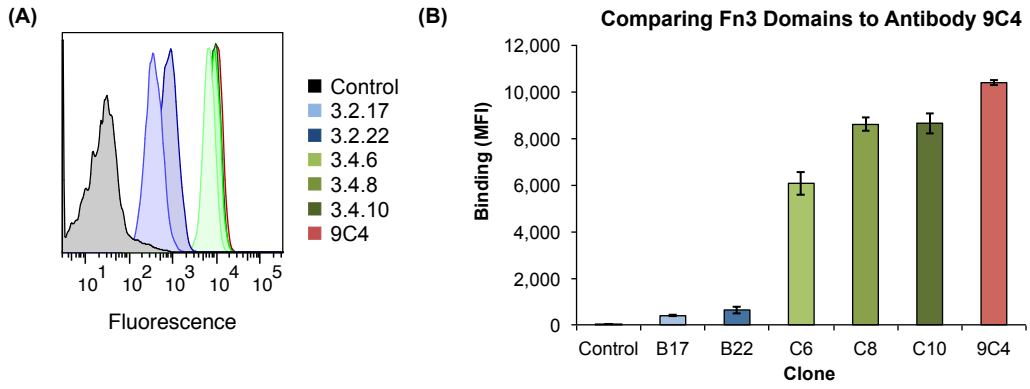

Figure 7. Comparison of EpCAM-Binding Fibronectin Clones and Monoclonal Antibody 9C4. Soluble anti-EpCAM fibronectin clones were evaluated for their ability to saturate EpCAM-positive MCF-7 cells via flow cytometry. As a positive control, an anti-EpCAM monoclonal antibody (clone 9C4) was evaluated simultaneously. (A) MCF-7 cells were saturated with either a soluble fibronectin clone or with 9C4 at 100 nM. Shown is a representative composite histogram of the fluorescence intensities produced by each sample in a single trial. (B) The analysis was performed in triplicate, and the mean fluorescence intensities produced by each clone are shown. Data is presented as the mean ± standard deviation of the three independent trials.

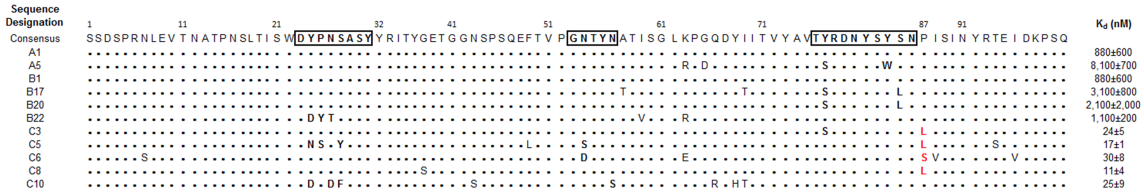

Figure 8. Sequences for EpCAM-Binding Fibronectin Domains. Sequences of EpCAM-binding fibronectin domains were compared by sequence alignment. Residues that match consensus are denoted by a ●. Engineered loop residues are shown in bold. P87L/S mutation is highlighted in red. Clones are labeled with letters corresponding to the population from which they were isolated: “A” denotes clones isolated from the unmatured population, “B” denotes clones isolated from the population matured without DTT, and “C” denotes clones isolated from the population matured with DTT.

```
Fn C5     SPRNLEVTNATPNSLTISWDNSNYASY--YRITYGETGGNSPSQELTVPGSTYNATISGLKPGQDYIITVYAV--TYRD
          +P+NL V+  T +S  +SWD+  +A Y  + I Y E+     +  LTVPGS  +  ++GLKPG +Y +++Y V   Y+D
Centyrin  APKNLVVSEVTEDSARLSWDDP-WAFYESFLIQYQESEKVGEAIVLTVPGSERSYDLTGLKPGTEYTVSIYGVHNVYKD
```

Figure 9. BLAST Alignment of Centyrin and Fibronectin Clone C5 Identifies Homologous Regions. To identify regions in the hydrophilic fibronectin scaffold that may be amenable to cysteine mutation analogous to the Centyrin platform,[111] the two protein domains were aligned using the Basic Local Alignment Search Tool (BLAST) available through the NIH. Two primary motifs were identified – LTVPGS and GLKPG.

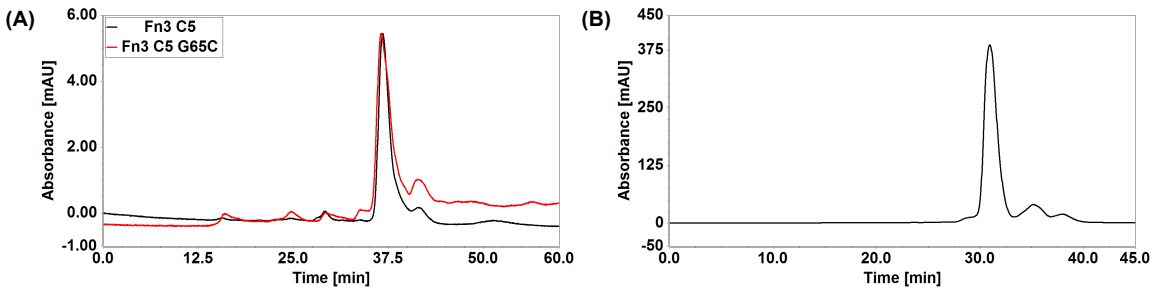

Figure 10. SEC Characterization of G65C-Mutant Fibronectin Domains. Fn3 domains containing the G65C mutation were expressed, purified, and analyzed via SEC as described above. (A) Fn3 C5 G65C (red) is purified as a monomer and compared to the parent clone Fn3 C5 (black). (B) Likewise, the non-targeted Fn3 NT G65C is purified as a monomer.

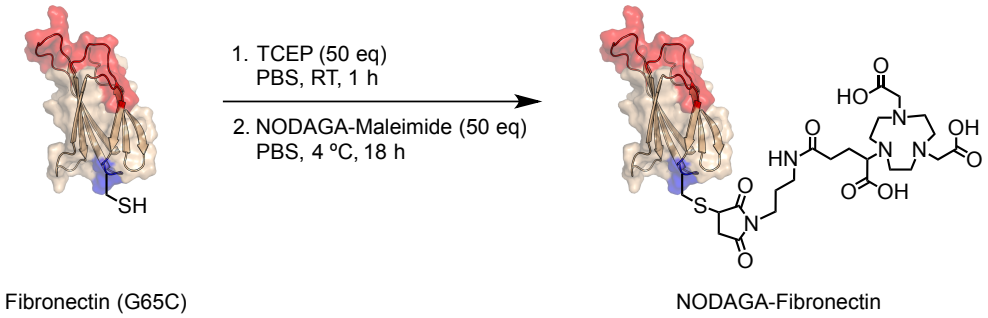

Figure 11. NODAGA Conjugation using Sulfhydryl/Maleimide Chemistry. Purified Fn3 domains containing the G65C mutation were site-specifically conjugated with the radiochelator NODAGA via a Michael addition reaction between the sulfhydryl group and the maleimide moiety, as shown.

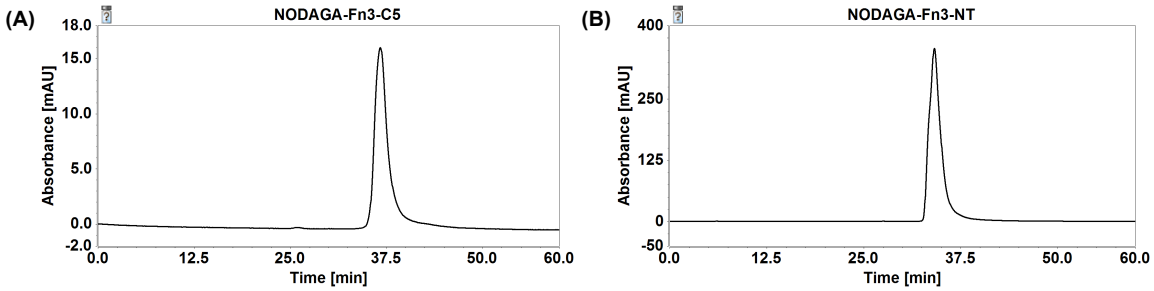

Figure 12. SEC Characterization of NODAGA-Fibronectin Conjugates. Fn3 domains containing the G65C mutation were conjugated to NODAGA, purified, and analyzed by SEC, as described above. Both the Fn3 C5 (A) and Fn3 NT (B) conjugates remain monomeric and free of aggregate species following conjugation. The retention times are essentially identical to the parent clones (not depicted), as the small difference in molecular weight due to the NODAGA conjugate is not resolvable on the SEC column used.

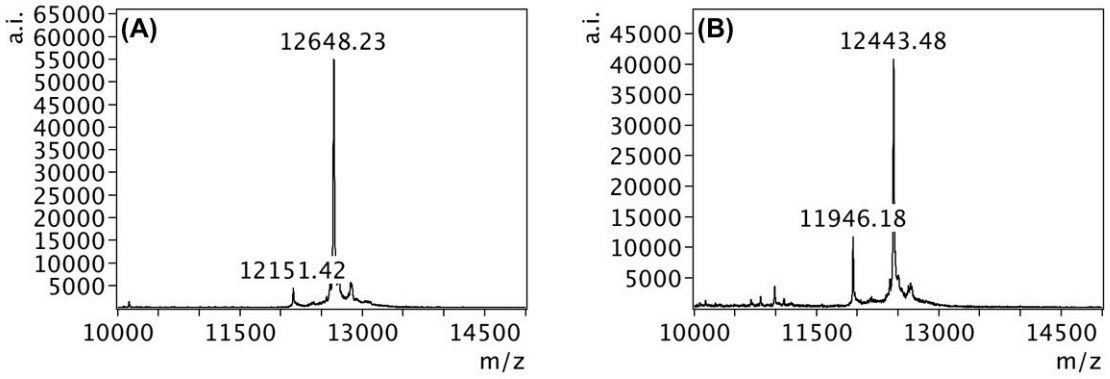

Figure 13. MALDI-MS Confirms NODAGA Conjugation. Successful conjugation of NODAGA-maleimide to (A) Fn3 C5 G65C, and (B) Fn3 NT G65C was verified by matrix-assisted laser desorption/ionization mass-spectroscopy (MALDI-MS). The mass shift between conjugated and unconjugated protein in each spectrum is ~497 amu, corresponding to the mass of the NODAGA-maleimide moiety. Coupling efficiency was ≥93% for NODAGA-C5 (A) and ≥78% for NODAGA-NT (B) by peak integration.

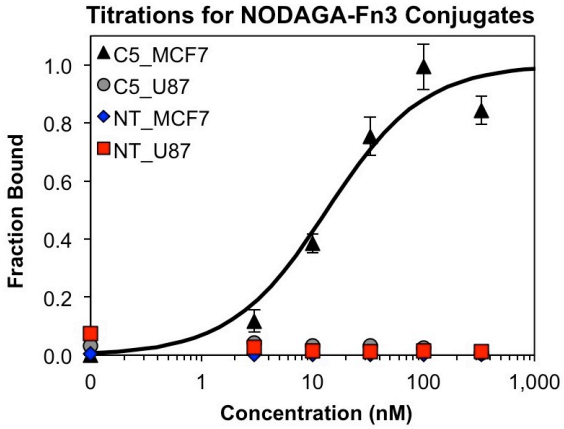

Figure 14. EpCAM Affinity and Selectivity of NODAGA-Fibronectin Conjugates. The NODAGA-Fn3 conjugates were titrated against EpCAM-expressing (MCF-7) and EpCAM-negative (U87-MG) cells, as described above. NODAGA-C5 exhibited a K_d value (14 ± 3 nM) similar to that of the parent clone, C5 (17 ± 1 nM) when assayed against MCF-7 cells (black triangles). Importantly, NODAGA-C5 does not bind to the U87-MG cells (grey circles). Likewise, the non-targeted NODAGA-NT scaffold binds to neither the MCF-7 cells (blue diamonds) nor the U87-MG cells (red squares).

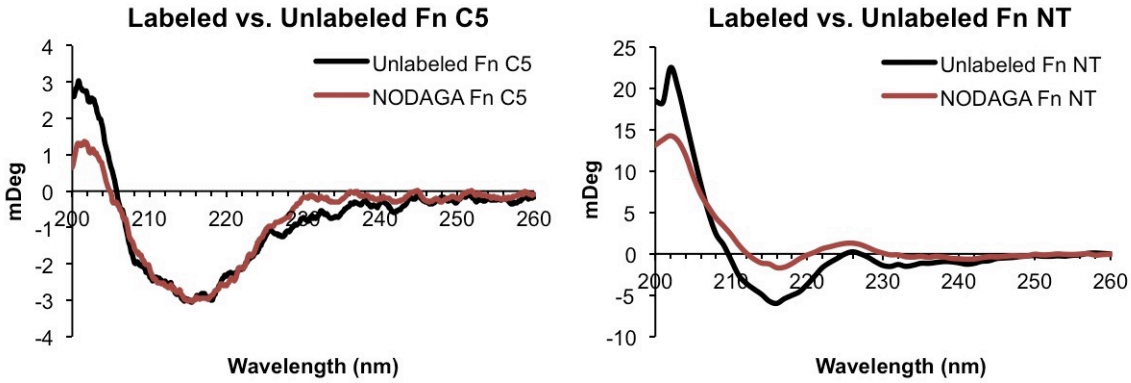

Figure 15. Circular Dichroism Spectra for NODAGA-Fibronectin Conjugates. The secondary structure of parent and NODAGA-conjugated Fn3 clones was evaluated by circular dichroism (CD), as described above. Neither the conjugation of NOGAGA-maleimide to (A) Fn3 clone C5 G65C, nor (B) Fn3 clone NT G65C had a detrimental effect on protein structure. This data is commensurate with the functional binding data observed in **Figure 14**.

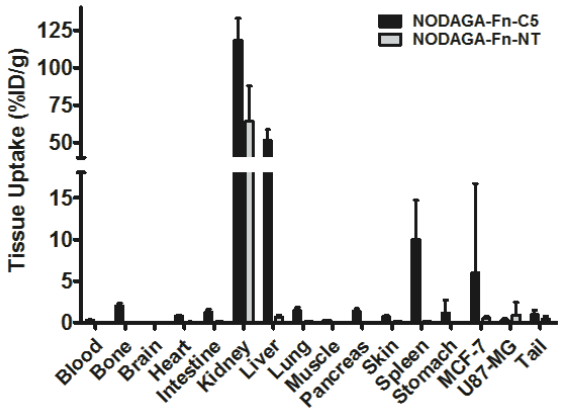

Figure 16. Biodistribution of NODAGA-Fibronectin Conjugates in a Murine Xenograft Model. After PET/CT imaging, the mice were euthanized and tissues were collected, weighed, and measured for radioactivity. The distributions of the EpCAM-targeted Fn3 C5 (black) and non-targeted Fn3 NT (gray) domains for the selected tissues are shown for 2 h post-injection. Data is presented as the mean ± standard deviation of the percent injected dose per gram of tissue (%ID/g) from four mice in each treatment group.

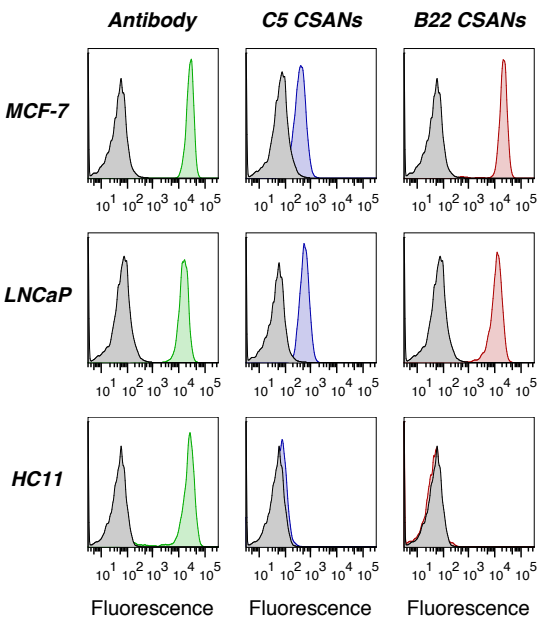

Figure 17. A Targeting Scaffold Utilizing EpCAM-Binding Fibronectin Domains Does Not Bind to Murine EpCAM-Expressing Cells. A chemically self-assembled nanoring (CSAN; see Chapters III and IV) utilizing either Fn3 clone C5 (blue) or B22 (red) was assessed for binding to two human cell lines (MCF-7 and LNCaP) and one mouse cell line (HC11) by flow cytometry. Briefly, cell lines were grown and detached, as described above. Cells ($5x10^4$) were resuspended in 20 µL of 500 nM EpCAM-targeted CSANs and incubated at 4 ºC for 1 h in the dark. Cells were washed with 1 mL PBSA and then resuspended in 50 µL of anti-His Alexa Fluor 647 conjugate or, in the case of the antibody control samples, either anti-EpCAM antibody clone 9C4 conjugated to Alexa Fluor 647 (human lines) or anti-EpCAM antibody clone G8.8 conjugated to Alexa Fluor 647 (mouse line). Samples were incubated at 4 ºC in the dark for 30 min before washing thrice with 1 mL PBSA, followed by immediate analysis on a BD LSR II flow cytometer. As indicated by the antibody controls (green), all cell lines express EpCAM. Both CSAN species bind to the human cell lines, whereas no binding to the mouse mammary epithelial cell line is observed.

Mutation	Direction	Sequence	Length (bp)	%GC	T_m (ºC)	T_a (ºC)
C-Terminal Insertion	Forward (5')	**TGT**GGATCCCACCATCACCAT	21	52	64	64
	Reverse (3')	CTGAGACGGTTTGTCGATTTC	21	48	63	
G65C	Forward (5')	GTCTGAAACCG**T**GCCAGGATTATATC	26	46	63	64
	Reverse (3')	CGCTGATGGTCGCATTATAA	20	45	63	

Table 1. Mutagenic Primer Sequences for Introducing Engineered Cysteine Residues. These oligonucleotide sequences were used as PCR primers to insert an C-terminal cysteine or perform a G65C substitution, as indicated, on the EpCAM-binding Fn3 clone C5 in the Novagen pET28a(+) vector. The modifications were made using site-directed mutagenesis via PCR, as described above.

CHAPTER III

Engineering Reversible Cell-Cell Interactions with Lipid-Anchored Prosthetic Receptors

INTRODUCTION

The ability to direct cell-cell interactions has tremendous value across numerous fields – including tissue engineering,[42, 44] regenerative medicine,[15, 32] and adoptive immunotherapy[28, 45] – and as a tool for elucidating fundamental biology.[31, 49] To this end, several approaches for modifying cell surfaces have been developed, perhaps the most notable being that of chimeric antigen receptor (CAR) T cells.[121] Though clinically efficacious, the genetic engineering underlying the CAR T cell platform makes it irreversible and yields several limitations that hinder its use for alternative applications.[122] Specifically, not all cell types – such as regenerative stem cells[123] – are readily amenable to such modification, and the permanence of the genetically encoded receptor has led to significant adverse events in the clinic, including B cell aplasia,[124] solid organ damage,[125] and neurotoxicity.[126]

To address these limitations and expand the use of cell-directing therapies, many groups have sought non-genetic approaches to introduce artificial receptors and targeting elements to the cell surface. Liposome fusion has been used to integrate bioorthogonal functional groups into the cell membrane, which can either be paired with complementarily modified cells or reacted with appropriately conjugated targeting ligands.[39, 53] Reactive groups can be introduced to the cell surface through metabolic engineering, wherein cells are grown in media supplemented with chemically functionalized sugar analogs that get incorporated into membrane glycoproteins; similarly, these functional groups can then be conjugated to antigen targeting elements.[44, 45] Others have taken advantage of naturally existing cell-surface amines (primarily lysine side chains) to bind activated esters tethered to a variety of species to the cell surface nonspecifically.[32, 35] Finally, various alkyl-, lipid-, and

glycophosphatidylinositol (GPI)-tagged species have been hydrophobically inserted and anchored into the cell membrane.[12, 16, 17, 26]

While many of these approaches have demonstrated the ability to direct specific cell-cell interactions, relatively few do so in a reversible fashion. Additionally, reversal mechanisms employed thus far – including irradiation with ultraviolet (UV) light,[45, 51] changes in electrochemical redox potential,[52] alterations in temperature,[21, 37] and enzymatic cleavage of the tethering species[22] – are largely unfit for *in vivo* applications, especially when surface-modified cells are distributed throughout an organism.

Expanding upon this body of prior work, we designed a cell membrane engineering methodology that would be broadly applicable to a variety of cell types and possess a reversal mechanism suitable for *in vivo* use. To accomplish this, we utilized a protein scaffold developed by our lab called the chemically self-assembled nanoring (CSAN; **Figure 1A**).[127] CSANs are formed when bivalent dihydrofolate reductase ($DHFR^2$) fusion proteins are spontaneously oligomerized by a chemical dimerizer, bis-methotrexate (bisMTX).[127] CSANs can be further functionalized by fusing various binding entities to the $DHFR^2$ subunits[128, 129] – in this case, either a monovalent streptavidin (mSA^{116}) unit or a fibronectin (Fn3) domain with engineered specificity for epithelial cell adhesion molecule (EpCAM) was fused.[102] Similarly, the bisMTX moiety can be chemically modified to incorporate a bioorthogonal ligation handle, such as an azide group.[129, 130] Using stoichiometric combinations of the fusion proteins and the bisMTX, one can form multivalent, heterobifunctional CSANs capable of targeting multiple distinct antigens.[131] Importantly, the CSAN scaffold can be disassembled through exposure to the FDA-approved antibiotic trimethoprim, providing a pharmacologic mechanism for removing the targeting ligands from the cell surface.[28, 130, 131]

Consistent with the aim to develop a surface engineering approach that would be applicable to multiple cell types, we devised a system based upon the spontaneous hydrophobic insertion of phospholipid conjugates (**Figures 1B-C**). Using either 1,2-distearoyl-sn-glycero-3-phosphoethanolamine-N-{biotinyl(polyethylene glycol)-2000} (DSPE-PEG_{2000}-biotin) or 1,2-distearoyl-sn-glycero-3-phosphoethanolamine-N-{dibenzocyclooctyl(polyethylene glycol)-2000} (DSPE-PEG_{2000}-DBCO), cell surfaces can be decorated with biotin and DBCO moieties, respectively. Targeted CSANs are then attached to the lipid-modified cells via a non-covalent biotin/mSA interaction or a copper-free, strain-promoted alkyne/azide cycloaddition (SPAAC) between the DBCO/azide groups, thereby functionalizing the cell with EpCAM-binding domains. As demonstrated herein, the CSAN-functionalized cells are capable of interacting with EpCAM+ target cells, and these intercellular interactions are readily reversed with trimethoprim.

As such, this study details a non-genetic, two-component strategy to functionalize cells with antigen-binding ligands capable of directing targeted cell-cell interactions in a pharmacologically reversible fashion.

RESULTS AND DISCUSSION

Functionalized Phospholipids Hydrophobically Insert Into Cell Membranes

The spontaneous membrane insertion of hydrophobic species – including alkyl chains, phospholipids, and GPI-conjugated proteins – has been demonstrated in numerous cell types,[20, 23, 61] including mesenchymal stem cells (MSCs).[15, 17, 25] These results have shown that this insertion is innocuous to the modified cell, having no effect on cell viability, proliferation, or differentiation. Furthermore, this approach is facile, requiring no specialized reagents or techniques, and is universally applicable to essentially any cell

type. Therefore, we decided to use hydrophobic insertion to tether our CSANs to the cell surface (**Figures 1B-C**).

The commercially available phospholipid conjugates DSPE-PEG_{2000}-biotin and DSPE-PEG_{2000}-DBCO were selected for this study. These species were chosen because we hypothesized that the hydrophobic lipid would enable membrane insertion while the long, flexible PEG linker would improve the accessibility of the biotin and DBCO groups. We also envisioned two approaches to labeling the cells with the phospholipids: (1) resuspending the cells *ex vitro* in buffer supplemented with the phospholipids; and (2) actively culturing the cells *in vitro* in phospholipid-supplemented media. Importantly, cell viability was not affected by either lipid-modification approach, even when concentrations of up to 100 μM of DSPE-PEG_{2000}-biotin or DSPE-PEG_{2000}-DBCO were used (**Figure 2**). This was true for both of the model cell lines, adherent MCF-7 and suspensive Raji cells.

To simultaneously assess the membrane insertion of phospholipids and ensure that the biotin and DBCO groups were accessible, cells were analyzed via flow cytometry using streptavidin- and azide-conjugated fluorophores, respectively. Both MCF-7 and Raji cells were modified with increasing concentrations of DSPE-PEG_{2000}-biotin or DSPE-PEG_{2000}-DBCO through both the buffer (*ex vitro*) and culture (*in vitro*) methods. In all instances, the biotin and DBCO moieties were readily detected on the cell surface after lipid modification, indicating both successful membrane insertion and availability of the functional groups for subsequent labeling (**Figures 3 and 4**). Furthermore, the extent of the modification could be easily modulated by varying the concentration of the phospholipid conjugate that was used.

Seemingly, the DSPE-PEG_{2000}-biotin species affords a more tunable modification than DSPE-PEG_{2000}-DBCO (**Figure 3**). However, this observation is likely an artifact of the short time (1 hour) and low temperature (4 ºC) for which the lipid-modified cells were incubated with the secondary reagent, as the biotin/streptavidin interaction forms more rapidly[132] than the slower azide/alkyne ligation[133] necessary to detect the DBCO species. Indeed, extending this incubation time to ≥3 h and raising the temperature to 37 ºC enhanced conjugation to surface DBCO groups (**Figure 5**). Thus, it is possible that both DSPE-PEG_{2000}-biotin and DSPE-PEG_{2000}-DBCO insert into the membrane to a similar extent, and that the discrepancies between the labeling observed in **Figures 3 and 4** are due to the differences between the subsequent binding and ligation efficiencies. Additionally, the hydrophobicity of the DBCO group itself may drive interactions with hydrophobic membrane components, further slowing the cycloaddition reaction.

Lastly, the Raji cells appear to become saturated with DSPE-PEG_{2000}-biotin following incubation with 10 μM of the phospholipid, as incubation with 100 μM does not afford an increase in the fluorescent signal. Across the concentration range tested, no such saturation was observed for the MCF-7 cells. This observation is most likely explained by the difference in size between the two cell types – the Raji cells are smaller and thus their membranes cannot support the same quantity of the DSPE-PEG_{2000}-biotin as the larger MCF-7 cells.

Collectively, this data shows that a variety of cell types can be effectively modified with phospholipid conjugates via hydrophobic insertion into the cell membrane without effecting cell viability. These results are consistent with those obtained by others performing similar hydrophobic insertions and further validates this approach as a universal method for cell surface modification.[15, 17, 20, 23, 25, 32, 61]

Production and Characterization of Cell-Binding CSANs

EpCAM is a cell surface antigen that is overexpressed by numerous carcinomas and several cancer stem cells.[78] We previously reported the development of EpCAM-binding Fn3 ligands, based upon the human tenth type III fibronectin domain.[102] To impart EpCAM-targeting capabilities to our CSANs, we fused Fn3 clone C5 (K_d = 17 ± 1 nM) to the *C*-terminus of our $DHFR^2$ fusion proteins. When these $DHFR^2$-Fn3 monomers were exposed to a molar excess of the chemical dimerizer, bisMTX, they rapidly and completely oligomerized into Fn3 CSANs, as demonstrated by size exclusion chromatography (SEC; **Figures 6A-B**). Importantly, the Fn3 CSANs continued to bind to EpCAM-expressing MCF-7 cells with high affinity (apparent K_d = 21 ± 6 nM) and selectivity (**Figures 7A-B**).

We next sought to develop methods for binding these Fn3 CSANs to cells that had been modified with DSPE-PEG_{2000}-biotin or DSPE-PEG_{2000}-DBCO. To recognize the biotin-decorated cells, we fused a monovalent streptavidin domain (mSA) to the *N*-terminus of the $DHFR^2$ fusion proteins. In the presence of bisMTX, these mSA-$DHFR^2$ monomers readily oligomerized into biotin-binding CSANs (**Figure 6C**). Furthermore, equimolar mixtures of the mSA- and Fn3-fused monomers could be co-assembled into CSANs with bispecificity for both biotin and cellular EpCAM (**Figure 6D**). Importantly, these bispecific mSA/Fn3 CSANs retained their apparent affinity for EpCAM+ cells (apparent K_d = 24 ± 6 nM; **Figure 7A**).

Our group has previously reported the synthesis and use of a bisMTX analog that incorporates a free amine suitable for further conjugation and additional functionalization.[129, 130] To produce CSANs capable of binding to the DBCO-decorated

cells, we coupled a PEG_4-azide moiety to this amine via *N*-hydroxysuccinimide (NHS) chemistry, generating an azide-bisMTX analog that contains a free azide group (**Figure 8**). As with the parent bisMTX dimerizer, $DHFR^2$-Fn3 fusion proteins exposed to azide-bisMTX oligomerized into azide/Fn3-CSANs (**Figure 6B**).

We further verified the formation of the mSA, Fn3, and mSA/Fn3 bispecific CSAN species via cryo-electron microscopy (cryo-EM). Nanoring structures were readily visualized for all three species (**Figures 9A-C**), and multiple analyses indicated similar sizes for the mSA (18 ± 3 nm), Fn3 (19 ± 4 nm), and mSA/Fn3 bispecific (19 ± 4 nm) CSANs (**Figure 9D**). These diameters are in close agreement to dynamic light scattering (DLS) measurements of the hydrodynamic radii of these species (**Figure 10**).

CSANs are Readily Installed on Cells Modified with Phospholipid Conjugates

After confirming the membrane insertion of the phospholipid conjugates, we sought to use the associated functional groups as handles for the attachment of our nanoring platform. Cells were first modified with DSPE-PEG_{2000}-biotin or DSPE-PEG_{2000}-DBCO *ex vitro*. They were subsequently incubated with CSANs of various functionalities at 4 ºC for 1 h, or in the case of the Fn3 CSANs oligomerized with azide-bisMTX, 37 ºC for 3 h. Specifically: (1) mSA CSANs were successfully bound to biotin-modified MCF-7 cells (**Figure 11A**); (2) Fn3 CSANs oligomerized with azide-bisMTX were conjugated to DBCO-modified Raji cells (**Figure 11B**); and (3) Fn3 CSANs were bound to EpCAM-expressing MCF-7 cells (**Figure 11C**). Additionally, mSA/Fn3 bispecific CSANs could be installed on both biotin-modified Raji cells (**Figure 11D**) and unmodified MCF-7 cells (**Figure 11E**), demonstrating the retained bifunctionality of these co-assembled CSANs. These experiments also verified the presence of both the mSA-$DHFR^2$ and $DHFR^2$-Fn3 subunits within a single CSAN, as the analyzed events were positive for both the FLAG

and MYC epitope tags present on the respective fusion proteins (**Figure 12A**). Finally, in preparation for future cell-targeting experiments, the optimal labeling concentration of mSA/Fn3 CSANs on Raji cells modified with DSPE-PEG_{2000}-biotin was assayed by flow cytometry and found to be 100 nM (**Figure 12B**).

Phospholipid-Anchored CSANs are Highly Stable In Vitro

While the insertion of hydrophobic anchors into the lipid bilayer is an energetically favorable process,[12] it is typically a transient modification with a half-life on the order of hours for cells in active culture.[15, 20] Additionally, because the lipids can insert into essentially any cell membrane, it was conceivable that a lipid-anchored species could dissociate from the membrane into which it was principally installed and subsequently label a neighboring cell, essentially "hopping" from the intended cell to a bystander cell. However, we hypothesized that by engaging multiple lipid anchors per nanoring, the multivalency of the CSAN would afford an improved surface stability relative to single lipid species and keep the CSANs localized to the principally modified cell.

To test both the surface stability of lipid-anchored CSANs and their potential to transfer amongst cells, two populations of Raji cells were differentially labeled. The first population was labeled only with CellTrace Violet (CTV) dye. The second population was modified with DSPE-PEG_{2000}-biotin *in vitro* and then labeled with "reduced valency" mSA CSANs. To more accurately recapitulate the valency of mSA domains that would be present in a bifunctional mSA/targeted CSAN, the CSANs used in this study were co-assembled with an equal ratio of mSA-$DHFR^2$ monomers and non-targeted $DHFR^2$ monomers. In this manner, the reduced valency CSANs used in this experiment serve as a surrogate for any bispecific mSA/targeted CSAN, including the mSA/Fn3 CSANs previously introduced.

The CTV-labeled and CSAN-labeled Raji cell populations were combined and co-cultured for 72 h; every 24 h, the culture media was refreshed (to partially simulate the effect of clearance) and a sample of the pooled population was analyzed for CTV and CSAN presence by flow cytometry. For comparison, the same analysis was performed for a mixed population of CTV-labeled Raji cells and Raji cells only modified with the DSPE-PEG_{2000}-biotin (no CSANs). As shown in **Figure 13A**, the lipid-anchored CSANs remained stably bound to the cell surface for ≥72 h. In contrast, significant loss of the monomeric phospholipid conjugates was observed over this same time frame ($p<0.0025$). This indicates that, through the engagement of multiple phospholipid conjugates, the multivalent CSANs possess an increased avidity for the cell surface and thus an enhanced surface stability relative to species that are anchored by only a single lipid. Furthermore, the CSANs exhibited a surface half-life of approximately 24 h when incubated in mouse plasma (**Figure 14**), making them considerably more stable than previously-reported phospholipid-anchored constructs and thus potentially useful for future *in vivo* applications. Furthermore, **Figure 13C** demonstrates that there is minimal migration of a lipid-anchored CSAN from one cell to another. Specifically, the percentage of CTV+/CSAN+ Raji cells in the population increases only marginally over the course of three days, from 0.9 ± 0.3% of the population on day zero to 2.9 ± 0.9% on day three; this correlates to a decrease in the number of CTV+/CSAN- Raji cells from 27.1 ± 0.9% to 24.5 ± 0.4% over the same time period. A similar effect is observed for the monomeric DSPE-PEG_{2000}-biotin moieties (**Figure 13D**), with an increase in the number of CTV+/lipid+ cells from 0.6 ± 0.6% to 4.1 ± 0.8% and a corresponding decrease in the number of CTV+/lipid- cells from 26.9 ± 0.5% to 23.3 ± 0.5% over three days. This data suggests that, while the phospholipid conjugates and their tethered cargo can dissociate from the cell surface, very few of the dissociated species re-insert themselves into the

membranes of neighboring cells. This is likely due to the low concentration of the dissociated species in the media and the frequent refreshing of the cell media (every 24 h), thus reducing the accumulation of free phospholipid conjugates.

Trimethoprim Removes Targeting Elements from the Cell Surface

To date, relatively few cell surface engineering approaches – either genetic or non-genetic in origin – possess mechanisms for removing the artificial receptors from the cell surface. Furthermore, many of those reversal stimuli are not currently suited for *in vivo* applications.[21, 22, 37, 51, 52] Accordingly, we sought to utilize the trimethoprim-induced disassembly of the CSAN scaffold as a pharmacologic mechanism for removing the targeting ligands from the surface of a CSAN-functionalized cell. To demonstrate this, Raji cells were sequentially modified with DSPE-PEG_{2000}-biotin *in vitro* and labeled with mSA/Fn3 bispecific CSANs. The CSAN-functionalized Raji cells were then resuspended in culture media supplemented with a clinically-relevant concentration of trimethoprim (2 μM; serum concentrations of trimethoprim have been shown to reach peak concentrations of ~6-15 μM within 2 h of oral dosing[134, 135]) and incubated at 37 ºC for up to 2 h. An aliquot of cells was analyzed by flow cytometry at 0, 1, and 2 h. As shown in **Figure 13B**, the targeting ligands were dissociated from the cell surface in a time-dependent manner, with 95% of the EpCAM-targeted Fn3 domains removed within 2 h.

CSANs Direct Reversible Cell-Cell Interactions In Vitro

The ability of CSANs to direct reversible intercellular interactions *in vitro* was assessed by fluorescence microscopy (**Figure 15A-C**). CFSE-labeled Raji cells were sequentially modified with DSPE-PEG_{2000}-biotin, labeled with mSA/Fn3 bispecific CSANs, and then incubated with a monolayer of EpCAM-expressing target cells (MCF-7) adhered to glass coverslips. The CSAN-functionalized Raji cells readily bound to the monolayer of target

cells (**Figure 15B**), and these cell-cell interactions were readily reversed via a brief (1 h) exposure to trimethoprim (**Figure 15C**). Importantly, phospholipid-modified cells that were not functionalized with the mSA/Fn3 CSANs were not able to interact with the target cells (**Figure 15A**), indicating that the observed interactions were induced by the CSANs and not non-specific adherence.

A similar experiment was conducted via flow cytometry. In this case, CTV-labeled Raji cells were again modified with DSPE-PEG_{2000}-biotin and labeled with mSA/Fn3 bispecific CSANs. They were then combined with detached, CFSE-labeled MCF-7 cells and incubated together on a rotating platform for 1 h. Samples were subsequently resuspended in either standard culture media or media supplemented with 2 μM trimethoprim. After another 1 h incubation with rotation, samples were thoroughly washed and analyzed on a flow cytometer. Similar to the microscopy results, very few non-specific cell-cell interactions are observed in the absence of the CSANs (**Figure 15D**). However, the CSAN-functionalized Raji cells were able to form targeted cell clusters with the MCF-7 cells (**Figure 15E**); again, nearly all of the targeted interactions were dissociated with trimethoprim treatment (**Figure 15F**). Even under the high-flow conditions of the cytometer (an instrument designed for single cell analyses), the CSAN-functionalized Raji cells were able to form significantly more interactions with the MCF-7 cells relative to the non-functionalized Raji cells (7.3 ± 1.1% vs. 0.8 ± 0.1%; $p<0.001$). Brief exposure to trimethoprim drove significant dissociation of these clusters ($p<0.01$), returning nearly the baseline number of non-specific interactions (1.9 ± 0.3%). As demonstrated above, the trimethoprim-induced dissociation of the CSAN scaffold is time-dependent; therefore, it is conceivable that prolonging the trimethoprim incubation in this experiment beyond 1 h would drive further reversal of the cell-cell interactions.

Bioorthogonal CSANs Enable Formation of Multicellular Interactions

Taking advantage of the modular nature of the CSAN platform, we sought to use a combination of multifunctional CSANs to induce controlled interactions between three different model cell populations (**Figure 16**). MCF-7 cells were again adhered to glass coverslips to form a monolayer of EpCAM-positive target cells. Then, CFSE-labeled Raji cells that had been sequentially modified with DSPE-PEG_{2000}-biotin and mSA/Fn3 CSANs were bound to the MCF-7 cells, as before. To introduce a third cell population, a separate aliquot of Raji cells was labeled with CellTrace Far Red, modified with DSPE-PEG_{2000}-DBCO, and functionalized with azide/mSA bispecific CSANs capable of targeting the unoccupied biotin moieties on the surface of the preceding CFSE-labeled Raji population. After washing the cell layer to remove unbound CFSE-Raji cells, the functionalized FarRed-Raji cell population was added and incubated in an analogous fashion. After washing, fixation, and mounting on glass slides using DAPI-containing mountant, the coverslips were analyzed by fluorescence microscopy. In the absence of CSANs, we again observed that the phospholipid-modified Raji cells were unable to interact with the MCF-7 cells (**Figure 16A**). However, the CSAN-functionalized Raji cells were able to form targeted cell arrangements, adhering to the monolayer of EpCAM-expressing cells and to each other (**Figure 16B**). Many of these interactions were reversed after a one hour incubation in trimethoprim-containing media (**Figure 16C**). Finally, when the FarRed-Raji cells that had been functionalized with the azide/mSA CSANs were incubated with just the primary MCF-7 cell layer, they were not able to adhere as these cells did not express the target “antigen”, in this case, biotin (**Figure 16D**). These results indicate that by exchanging the various targeting domains utilized in the CSAN platform, diverse cell populations can be driven to interact with one another in a controlled and pharmacologically reversible fashion.

CONCLUSIONS

In conclusion, the CSAN platform offers a modular approach for reversibly functionalizing cell membranes with targeting ligands. Through the spontaneous membrane insertion of phospholipids conjugated to biotin and DBCO groups, CSANs can be installed on essentially any cell surface and function as prosthetic receptors. In contrast to genetic engineering approaches, which require both manipulation of the target cell's genome and extensive culturing to expand the modified cells, the method described here is rapid, scalable to large cell numbers, and broadly applicable to diverse cell types.

Once installed on cell surfaces, EpCAM-targeting CSANs were capable of inducing specific intercellular interactions between the CSAN-functionalized cells and EpCAM-expressing target cells *in vitro*. Due to the modularity of the CSAN platform, this approach was further expanded to direct targeted interactions between three different cell populations. Additionally, these interactions were rapidly reversed through exposure to trimethoprim.

The capacity to remove CSAN-based surface modifications pharmacologically with trimethoprim makes them distinct from other reversal approaches developed thus far. While photoirradiation, enzymatic degradation, and changes in redox potential or temperature have all been demonstrated, none of these mechanisms are currently applicable in an *in vivo* setting, especially when the modified cells are broadly distributed throughout an organism (as would be the case for immunotherapy and some regenerative medicine applications). Because trimethoprim is an FDA-approved antibiotic that is used systemically, CSAN-directed cell-cell interactions could conceivably be readily reversed *in vivo* via trimethoprim administration, providing a safe

mechanism for deactivating the targeted cells in the case of adverse events or initiating processes dependent on the loss of intercellular interactions. Ultimately, this work demonstrates that lipid-anchored prosthetic receptors provide a broadly applicable approach to cell surface engineering that could be used to expand the formation of targeted, reversible cell-cell interactions across diverse fields.

MATERIALS & METHODS

Cells and Cell Culture

The MCF-7, U-87 MG, and Raji cell lines were previously purchased from the American Type Culture Collection (ATCC). MCF-7 and U-87 MG cells were grown at 37 ºC in a humidified atmosphere with 5% CO_2 in Dulbecco's Modified Eagle's Medium (DMEM) with 4.5 g/L glucose, L-glutamine, and supplemented with 10% fetal bovine serum (FBS), 100 U/mL penicillin, and 100 µg/mL streptomycin. Raji cells were grown at 37 ºC in a humidified atmosphere with 5% CO_2 in Roswell Park Memorial Institute (RPMI) media with L-glutamine and supplemented with 10% FBS, 100 U/mL penicillin, and 100 µg/mL streptomycin. For passaging, adherent cell lines MCF-7 and U-87 MG were detached via trypsin. Cell count and viability were determined via trypan blue exclusion using a Bio Rad TC20 automated cell counter (Bio Rad Laboratories, Inc.).

Expression Plasmids

gBlock Gene Fragments coding for the $DHFR^2$-Fn3 and mSA-$DHFR^2$ fusion proteins were ordered from Integrated DNA Technologies (IDT) and cloned into the Novagen pET28a(+) vector (EMD Millipore, Cat: 69864-3) via *NcoI* and *XhoI* restriction sites. Notably, the $DHFR^2$-Fn3 proteins contain an *N*-terminal MYC epitope tag and *C*-terminal polyhistidine tag to facilitate detection via flow cytometry and purification via immobilized

metal affinity chromatography (IMAC), respectively. Similarly, the mSA-DHFR^2 proteins contain a *C*-terminal FLAG epitope tag to enable flow cytometric detection.

Protein Expression and Purification

The DHFR^2-Fn3 fusion proteins were produced in *Escherichia coli* (*E. coli*) and purified from the soluble fraction of the cell lysates by IMAC according to the methods previously reported for the parent Fn3 clones.[102] The mSA-DHFR^2 fusion proteins were produced in *E. coli* and purified from the insoluble inclusion bodies of the cell lysates according to our previously reported refolding methods.[28, 136] Purified proteins were analyzed by SEC on a Superdex 200 Increase 10/300 gel filtration column (GE Healthcare Life Sciences, Cat: 28990944) in phosphate buffered saline (PBS, pH 7.4) running buffer (**Figure 6**). Fusion protein retention times were compared to those of commercial molecular weight standards (Sigma Aldrich, Cat: MWGF1000-1KT).

CSAN Formation and Characterization

CSANs were formed by adding a 3-fold molar excess of the desired chemical dimerizer to a solution of targeted DHFR^2 fusion protein monomers in PBS. Consistent with our previous studies, CSAN oligomerization occurred within minutes of adding the dimerizer.[127] Cryo-EM samples were prepared using a Vitrobot Mark IV (FEI). Briefly, 3 µL of CSANs in PBS was applied to a lacey formvar/carbon grid (Ted Pella, Inc.; Cat: 01883) in a humidified chamber, blotted, and plunged into liquid ethane for vitrification. Grids were imaged on a Tecnai Spirit G2 BioTWIN (FEI) equipped with an Eagle 2k CCD camera (FEI) under a high tension of 120 kV. Images were analyzed in ImageJ and, for the size distribution analysis, only nanoparticles with ≥70% circularity were included. For DLS, 60 µL of CSANs in PBS were loaded into a cuvette and analyzed on

a Punk DLS unit (Unchained Labs). Hydrodynamic diameter values represent the mean ± standard deviation of at least three measurements.

Affinity Determination of Fn3 and mSA/Fn3 CSANs

The apparent affinity and selectivity of the Fn3 and mSA/Fn3 CSANs were determined by flow cytometry, as previously described.[102] Briefly, EpCAM-expressing MCF-7 cells and EpCAM-negative U-87 MG cells were cultured to approximately 80% confluency, detached, and counted, as described above. Aliquots of $5x10^4$ cells were washed with PBSA (PBS with 0.1% w/v bovine serum albumin) and labeled with varying concentrations of Fn3 or mSA/Fn3 CSANs for ≥90 min at 4 ºC. Cells were then pelleted (500g, 5 min, 4 ºC) and resuspended in 50 µL anti-MYC (clone 9E10) Alexa Fluor 647 conjugate (Thermo Fisher Scientific, Cat: MA1-980-A647; 5 µg/mL in PBSA). After incubating at 4 ºC for ≥30 min in the dark, cells were washed thrice with 1 mL cold PBSA before the fluorescence was analyzed on an LSR II flow cytometer (BD Biosciences).

Hydrophobic Insertion of Phospholipid Conjugates

DSPE-PEG_{2000}-biotin and DSPE-PEG_{2000}-DBCO were purchased from Avanti Polar Lipids (Cat: 880129P and 880229P, respectively) and resuspended in PBS at pH 7.4. Cells were modified with DSPE-PEG_{2000}-biotin and DSPE-PEG_{2000}-DBCO via one of two methods: (1) through resuspension in phospholipid-containing PBS (*ex vitro*), or (2) through active culture in media supplemented with the phospholipid (*in vitro*).

For the *ex vitro* (buffer) method, cells were harvested from culture, pelleted at 300g for 5 min, and washed with 1 mL PBS. Cells were then resuspended in PBS containing the desired concentration of phospholipid (0-100 µM) at a concentration of $2.5x10^6$ cells/mL. The cell suspension was then placed on a rotating platform and incubated at room

temperature for 1 h. Cells were then pelleted at 300g for 5 min, and washed thrice with 1 mL cold PBS to remove uninserted DSPE-PEG_{2000}-biotin or DSPE-PEG_{2000}-DBCO. Cells were then used directly for subsequent applications.

For the *in vitro* (culture) method, cells were grown in culture media (DMEM or RPMI, as above) supplemented with the desired concentration (0-100 μM) of DSPE-PEG_{2000}-biotin or DSPE-PEG_{2000}-DBCO for 24-48 h. Cells were then harvested from culture (adherent cells were detached with trypsin), pelleted at 300g for 5 min, and washed thrice with 1 mL cold PBS to remove uninserted DSPE-PEG_{2000}-biotin or DSPE-PEG_{2000}-DBCO. Cells were then used directly for subsequent applications.

Following each modification, flow cytometry was used to determine whether the DSPE-PEG_{2000}-biotin or DSPE-PEG_{2000}-DBCO conjugates had inserted into the cell membrane. To probe for the biotin and DBCO moieties on the cell surface, the phospholipid-modified cells were washed as above and resuspended in 50 μL of either streptavidin Alexa Fluor 488 conjugate (Thermo Fisher Scientific, Cat: S32354; 10 μg/mL in PBS) or azide Alexa Fluor 488 conjugate (Thermo Fisher Scientific, Cat: A10266; 5 μM in PBS), respectively. After incubating at 4 ºC for 1 h, the cells were pelleted (500g, 5 min, 4 ºC) and washed thrice with 1 mL cold PBS before the fluorescence was analyzed on an LSR II flow cytometer (BD Biosciences). For data analysis, the maximum mean fluorescence intensity (MFI) obtained within each experimental series is normalized to 1.0, with the other samples in that series scaled relative to this value.

Functionalizing Phospholipid-Modified Cells with CSANs

Cells were cultured, harvested, and modified with 10 μM of either DSPE-PEG_{2000}-biotin or DSPE-PEG_{2000}-DBCO *ex vitro*, as described above. Generally, $0.5x10^6$ cells were

then labeled with 500 µL of 100 nM CSANs of the desired functionality (**Figure 13**) in PBS at 4ºC for 1 h. However, to install the Fn3 CSANs formed with azide-bisMTX onto DBCO-modified Raji cells, 100 µL of 500 nM CSANs in PBS was used and the cells were incubated at 37 ºC for 3 h. After the primary incubation, cells were washed once with 1 mL cold PBS to remove unbound CSANs. The cells were resuspended in 50 µL of either anti-MYC (clone 9E10) Alexa Fluor 647 conjugate (Thermo Fisher Scientific, Cat: MA1-980-A647; 5 µg/mL in PBS) or anti-FLAG PE conjugate (BioLegend, Cat: 637309; 1 µg/mL in PBS) to probe for the MYC epitope tag present on the $DHFR^2$-Fn3 subunits or the FLAG epitope tag present on the mSA-$DHFR^2$ subunits, respectively. After incubating at 4 ºC for 1 h, the cells were pelleted (500g, 5 min, 4 ºC) and washed thrice with 1 mL cold PBS before the fluorescence was analyzed on an LSR II flow cytometer.

Stability Studies

The *in vitro* longevity of the phospholipid-anchored CSANs on the cell surface was assessed by flow cytometry. Briefly, Raji cells were modified with 10 µM DSPE-PEG_{2000}-biotin *in vitro*, labeled with 100 nM "reduced-avidity" mSA CSANs (CSANs formed with a 1:1 ratio of mSA-$DHFR^2$ subunits and non-targeted $DHFR^2$ subunits), and then returned to culture for 0-72 h. At 24 h intervals, an aliquot of $0.5x10^6$cells was taken, labeled with an anti-FLAG PE conjugate (1 µg/mL in PBS) to detect cell surface CSANs, and analyzed on an LSR II flow cytometer, as described above. To compare the surface longevity of the CSANs to that of the individual DSPE-PEG_{2000}-biotin moieties themselves, a separate population of Raji cells was modified with only 10 µM DSPE-PEG_{2000}-biotin *in vitro* (no CSANs) and returned to culture for 0-72 h. An aliquot of these cells was taken, labeled with streptavidin Alexa Fluor 488 conjugate (10 µg/mL in PBS) to detect cell surface biotin moieties, and analyzed on an LSR II flow cytometer in parallel with the CSAN-labeled samples. To determine the number of cell divisions over

the course of the experiment, a third aliquot of Raji cells was labeled with CellTrace Violet (CTV; Thermo Fisher Scientific, Cat: C34571) according to the manufacturer's instructions and cultured/analyzed in parallel with the CSAN and phospholipid samples. For data analysis, the MFI of the samples at t=0 was normalized to 1.0, representing maximum labeling, and the MFI on subsequent days was scaled relative to this value. Because cell division reduces the MFI value through dilution of the CSANs/phospholipids across daughter cell membranes and not due to loss of the constructs, the MFI values of subsequent analyses were corrected for the number of cell divisions, as determined by the CTV labeling.

To ascertain whether the phospholipid-anchored CSANs could "migrate" from the principally modified cell to an unmodified neighbor cell, two populations of Raji cells were prepared. The first population was labeled only with CTV. The second population was modified with 10 μM DSPE-PEG_{2000}-biotin *in vitro* and then labeled with "reduced valency" mSA CSANs (see above). The CTV-labeled and CSAN-labeled Raji cell populations were combined at a 3:7 ratio and co-cultured in RPMI for 72 h; every 24 h, the culture media was refreshed (to partially simulate the effect of clearance) and a $0.5x10^6$ cell sample of the pooled population was analyzed for CTV and CSAN presence by flow cytometry. CSANs were detected by labeling the cells with anti-FLAG PE conjugate (1 μg/mL in PBS), as above. At each time point, the percentage of CTV+/CSAN- (original CTV-modified population), CTV+/CSAN+ (CTV cells that had acquired a "migrating" CSAN), CTV-/CSAN+ (original CSAN-functionalized population), and CTV-/CSAN- (cell that has lost their CSAN functionalization) cells was quantified by flow cytometry. For comparison, the same analysis was performed for a mixed population of CTV-labeled Raji cells and Raji cells modified with only the 10 μM DSPE-PEG_{2000}-biotin (no CSANs).

Trimethoprim-Induced CSAN Dissociation

Raji cells ($0.5x10^6$) were modified with 10 μM DSPE-PEG_{2000}-biotin *ex vitro* and then labeled with 100 nM mSA/Fn3 CSANs, as above. The CSAN-labeled cells were then divided into two equal aliquots, one of which was resuspended in 200 μL of RPMI and the other in 200 μL of RPMI supplemented with 2 μM trimethoprim (Fisher Scientific, Cat: AAJ66646MD). Cells were then incubated at 37 ºC for 1-2 h, labeled with anti-FLAG PE conjugate (1 μg/mL in PBS) to detect cell surface CSANs, and analyzed on an LSR II flow cytometer, as described above. For data analysis, the MFI of the samples in plain RPMI was normalized to 1.0, representing maximum labeling, and the MFI of the samples in RPMI with was scaled relative to this value.

Formation of Intercellular Interactions

To form intercellular interactions between two cell types (**Figure 15**), a monolayer of MCF-7 cells was adhered to glass coverslips (Thermo Scientific, Cat: 12-541-B) via overnight culture in a 6-well plate. Separately, a population of Raji cells was labeled with CFSE (BioLegend, Cat: 423801) according to the manufacturer's protocol and returned to culture overnight. The following day, the CFSE-labeled Raji cells were sequentially modified with 10 μM DSPE-PEG_{2000}-biotin *ex vitro* and 100 nM mSA/Fn3 CSANs, as above. The CSAN-functionalized, and thus EpCAM-targeted, Raji cells were then washed once in 1 mL PBS, resuspended in 1 mL DMEM, and added to the wells containing the MCF-7 cells on the coverslips. The two cell populations were then incubated static at 4 ºC for 1 h. Media and unbound cells were then removed via aspiration, and the cell layers were washed thrice with 1 mL PBS. Then, 1 mL of DMEM with or without 2 μM trimethoprim was added to the wells and the cell layers were incubated for another 1 h at 4 ºC. Media and unbound cells were again removed via

aspiration, and the cell layers were washed thrice with 1 mL PBS. The cell layers were then fixed in 4% paraformaldehyde in PBS at room temperature for 15 min before washing thrice with 1 mL PBS. Coverslips were then rinsed twice in ultrapure water, blotted to remove excess liquid, and mounted on glass coverslips using ProLong Gold Antifade Reagent with DAPI (Thermo Fisher Scientific, Cat: P36935). After curing for ≥24 h in the dark, slides were imaged on an Eclipse Ti-E Wide Field Deconvolution Inverted Microscope (Nikon Instruments, Inc.).

Intercellular interactions between three different cell populations (**Figure 16**) were formed similarly; however, the CFSE-labeled Raji cells were modified with only 50 nM mSA/Fn3 CSANs instead of 100 nM. Then, a third cell population was prepared by sequentially labeling Raji cells with CellTrace Far Red (Thermo Fisher Scientific, Cat: 34572) according to the manufacturer's protocols, 100 μM DSPE-PEG_{2000}-DBCO *ex vitro*, and 500 nM mSA CSANs oligomerized with azide-bisMTX, as above. This population of Raji cells – now capable of targeting the unoccupied biotin moieties on the CFSE-labeled Raji cell layer – was added to the wells after the incubation with the CFSE-labeled Raji cells (but before the addition of the DMEM with trimethoprim). After incubating the cell layers with this third cell population at 4 ºC for 1 h, the coverslips were washed, fixed, mounted, and imaged on an Eclipse Ti-E Wide Field Deconvolution Inverted Microscope, as above.

For the flow cytometry analysis of cell pairing, target MCF-7 cells were labeled with CFSE, cultured for 24 h, and detached, as above. Separately, a population of Raji cells were sequentially labeled with CTV, cultured for 24 h, modified with 10 μM DSPE-PEG_{2000}-biotin, and functionalized with mSA/Fn3 CSANs, as above. The two cell combined at a 1:1 ratio in PBS, and incubated at 4 ºC in the dark with rotation for 1 h.

Cells were pelleted (500 g, 5 min, 4 ºC), washed once with 1 mL cold PBS, and resuspended in PBS with or without 2 μM trimethoprim. After incubating at 4 ºC in the dark with rotation for 1 h, the cells were washed thrice with PBS and analyzed on an LSR II flow cytometer to ascertain the number of CTV+/CFSE+ cell clusters. As controls, unmodified Raji cells, unmodified MCF-7 cells, CTV-labeled Raji cells, CFSE-labeled MCF-7 cells, and CTV-Raji cells modified with only 10 μM DSPE-PEG_{2000}-biotin (no CSANs) plus CFSE-MCF-7 cells were all prepared and analyzed in parallel.

Statistical Considerations

Unless otherwise stated, experiments were performed in triplicate and data is presented as the mean ± standard deviation of three independent trials. Differences between means are compared using a two-tailed Student's t-test, and a p-value <0.05 is denoted in graphics with an (*), $p<0.01$ is denoted with (**), and $p<0.001$ is denoted with (***).

ACKNOWLDEGEMENTS

This work was supported by the National Institutes of Health (NIH) R21 CA185627 (CRW), F30 CA210345 (CMC), T32 GM008244 (CMC), R21 EB019518 (BJH), and the University of Minnesota. Parts of this work were carried out in the Characterization Facility, University of Minnesota, which receives partial support from NSF through the MRSEC program. The authors gratefully acknowledge Dr. Bob Hafner (Characterization Facility, University of Minnesota) for his assistance with the transmission electron microscopy experiments. Microscopy work was performed in the University Imaging Center at the University of Minnesota.

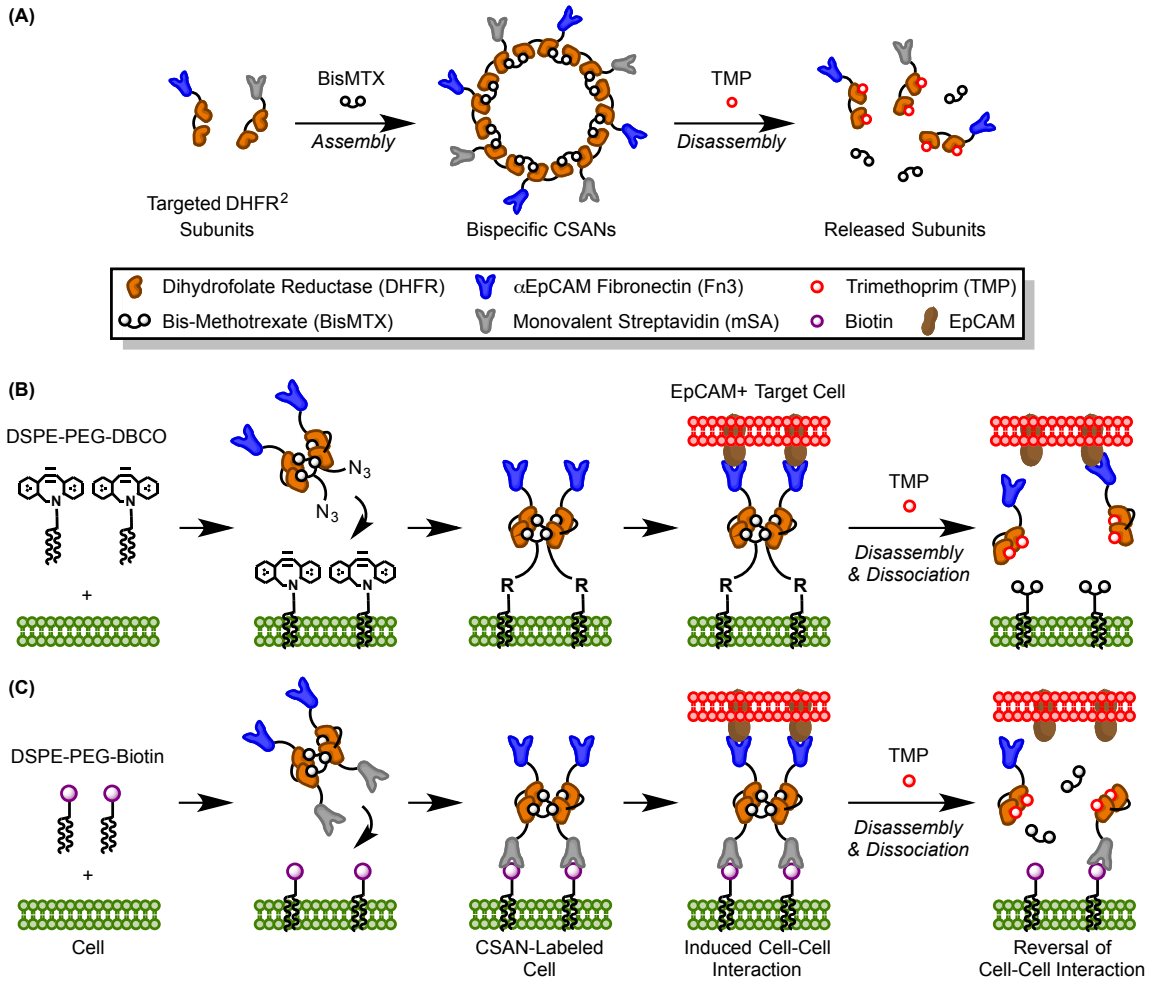

Figure 1. Cell Surface Engineering with Chemically Self-Assembled Nanorings (CSANs). (A) CSANs are composed of targeted-DHFR[2] fusion proteins that are spontaneously oligomerized by the chemical dimerizer, bisMTX; they can be pharmacologically disassembled by the FDA-approved antibiotic trimethoprim. (B) DSPE-PEG_{2000}-DBCO moieties spontaneously insert into cell membranes and are stabilized in the lipid bilayer by the hydrophobic effect.[12] EpCAM-targeted Fn3 CSANs oligomerized with an azide-bisMTX dimerizer are then installed on the cell surface through a copper-free, strain-promoted alkyne/azide cycloaddition. The CSAN-functionalized cells can then form targeted interactions with EpCAM+ cells, and these interactions can be reversed with trimethoprim. (C) Similarly, cells modified with DSPE-

PEG_{2000}-biotin moieties can be functionalized with bispecific mSA/Fn3 CSANs, enabling recognition of EpCAM+ target cells. Trimethoprim-induced disassembly of the CSAN reverses the intercellular interactions.

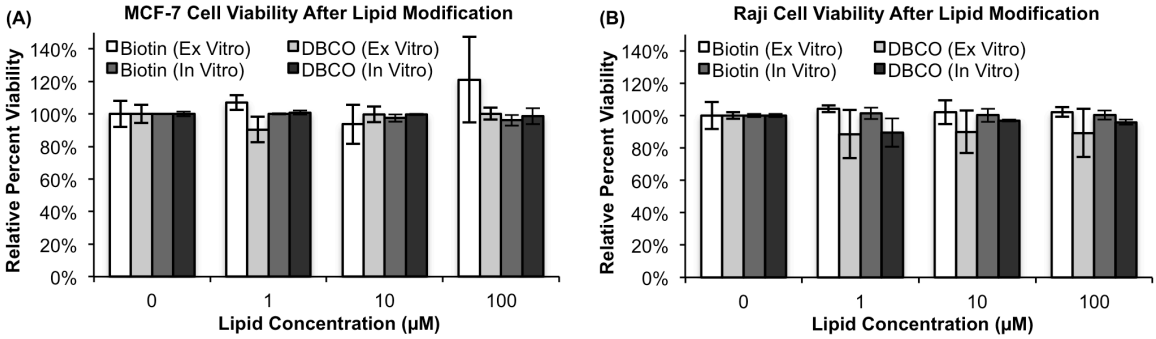

Figure 2. Cell Viability is Not Affected by the Hydrophobic Insertion of Phospholipid Conjugates. MCF-7 and Raji cells were modified with increasing concentrations of DSPE-PEG_{2000}-biotin or DSPE-PEG_{2000}-DBCO through either the *ex vitro* (buffer) or *in vitro* (culture) methods, as described in the methods. Following the phospholipid incubation, cells were pelleted (500g, 5 min, 4 ºC) and washed once in 1 mL PBS. Cell viability was determined via trypan blue exclusion using an automated cell counter. For data analysis, the viability of cells incubated in only PBS (no phospholipids) was normalized to 100%, with all other measurements scaled to this reference. Data is presented as the mean ± standard deviation of three trials.

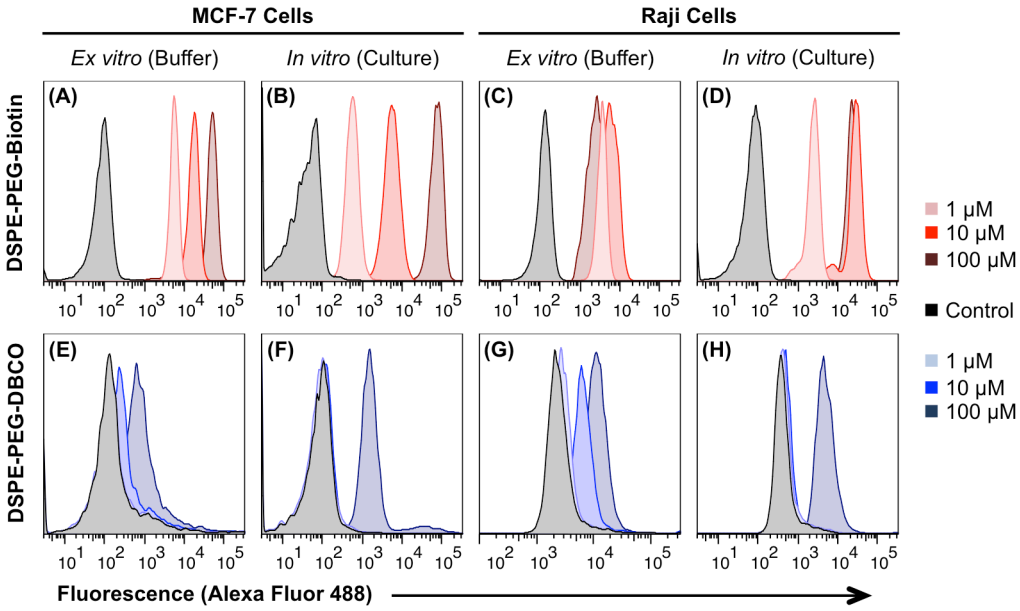

Figure 3. Phospholipid Conjugates Hydrophobically Insert into Cell Membranes. Cells were modified with increasing concentrations of either DSPE-PEG_{2000}-biotin or DSPE-PEG_{2000}-DBCO through one of two methods: (1) resuspension in phospholipid-containing buffer (ex vitro), or (2) active culture in phospholipid-containing media (in vitro). Cells were subsequently analyzed by flow cytometry using streptavidin- or azide-conjugated Alexa Fluor 488 to assess the presence of biotin and DBCO moieties, respectively, on the cell surface. Both adherent MCF-7 cells and suspensive Raji cells can be successfully modified with DSPE-PEG_{2000}-biotin or DSPE-PEG_{2000}-DBCO through both the ex vitro and in vitro approaches. While insertion experiments were performed in triplicate, a representative trial of each condition is shown here. A quantitative analysis of the triplicate data is presented in Figure 4.

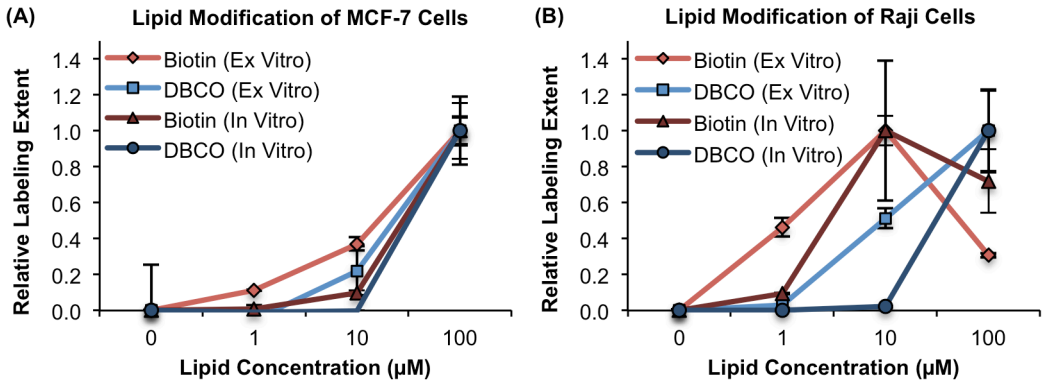

Figure 4. Quantitative Analysis of Phospholipid Conjugate Membrane Insertion. MCF-7 and Raji cells were modified with increasing concentrations of DSPE-PEG_{2000}-biotin or DSPE-PEG_{2000}-DBCO through either the *ex vitro* (buffer) or *in vitro* (culture) methods, as described in the methods. Cells were subsequently analyzed by flow cytometry using streptavidin- or azide-conjugated Alexa Fluor 488 to assess the presence of biotin and DBCO moieties, respectively, on the cell surface. As shown, both (A) adherent MCF-7 cells and (B) suspensive Raji cells can be successfully modified with DSPE-PEG_{2000}-biotin or DSPE-PEG_{2000}-DBCO through both the *ex vitro* and *in vitro* approaches. In an effort to quantitate the results presented in **Figure 3** and more clearly demonstrate the optimal labeling concentration for each scenario, the mean fluorescence intensity (MFI) within each experimental series is scaled such that the maximum labeling obtained under the specified conditions is presented as a labeling extent of 1.0. For example, Raji cells are optimally labeled with DSPE-PEG_{2000}-biotin *ex vitro* at a lipid concentration of 10 μM. Data is presented as the mean ± standard deviation of at least three trials.

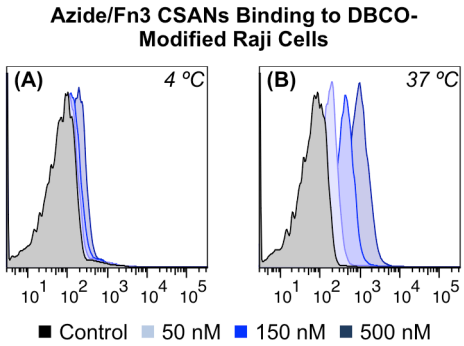

Figure 5. Elevated Temperature Promotes the DBCO/Azide Ligation on the Cell Surface. To explore the role of temperature on the efficiency of the copper-free ligation between membrane-tethered DBCO species and free azide groups, Raji cells modified with 10 μM DSPE-PEG_{2000}-DBCO were resuspended in PBS containing various concentrations of azide/Fn3 CSANs (0-500 nM) and incubated at either 4 ºC or 37 ºC for 3 h. The cells were then pelleted (500g, 5 min, 4 ºC), washed once in 1 mL PBS, and labeled with 50 μL anti-MYC (clone 9E10) Alexa Fluor 647 conjugate (5 μg/mL in PBS) to probe for surface-bound Fn3 CSANs. After incubating at 4 ºC for ≥30 min in the dark, cells were again pelleted and washed thrice with 1 mL cold PBSA before the fluorescence was analyzed on a BD LSR II flow cytometer.

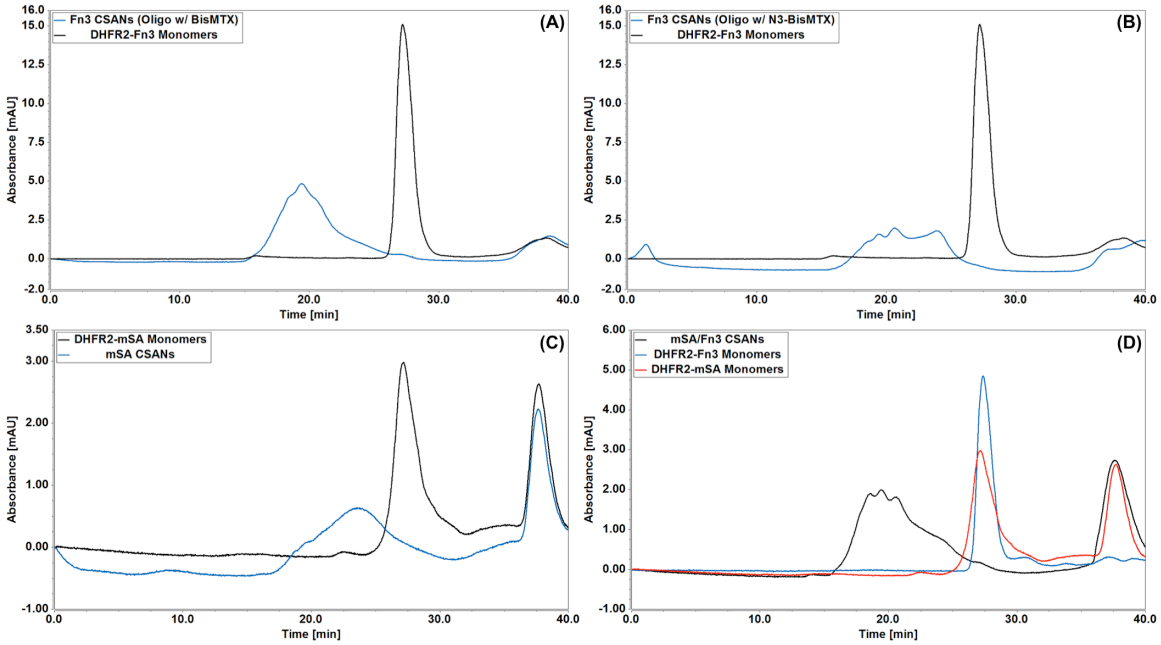

Figure 6. SEC Demonstrates Successful Oligomerization of DHFR^2 Monomers into CSANs. The ability of monomeric DHFR^2 fusion proteins to oligomerize into multimeric CSANs in the presence of a dimerizer (either bisMTX or azide-bisMTX) was assessed by size exclusion chromatography. DHFR^2-Fn3 subunits oligomerize into EpCAM-targeted Fn3 CSANs in the presence of either (A) bisMTX, or (B) azide-bisMTX, demonstrating that both dimerizers effectively oligomerize the subunits. (C) mSA-DHFR^2 subunits oligomerize into mSA CSANs in the presence of bisMTX. (D) DHFR^2-Fn3 subunits and mSA-DHFR^2 subunits can be co-assembled into bispecific mSA/Fn3 CSANs in the presence of bisMTX. Peaks with a retention time of ~38 minutes represent residual buffer from protein purification which, upon mixing with the PBS running buffer, generates a detectable solvent peak on our instrument.

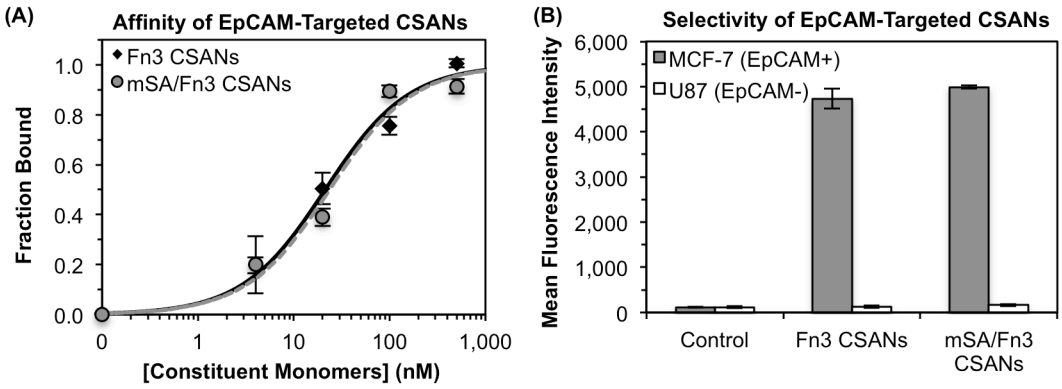

Figure 7. Affinity and Selectivity of EpCAM-Targeted CSANs. The anti-EpCAM affinity and selectivity of monospecific Fn3 and bispecific mSA/Fn3 CSANs was assessed by flow cytometry, as described in the methods. (A) The Fn3 CSANs (black diamonds and solid black line) and mSA/Fn3 CSANs (grey circles and dashed grey line) bind to EpCAM+ MCF-7 cells with apparent K_d values of 21 ± 6 nM and 24 ± 6 nM, respectively. (B) Neither species exhibits significant binding to EpCAM- U87 cells (white bars; $p>0.05$ for U87 MFI compared to control) at 500 nM.

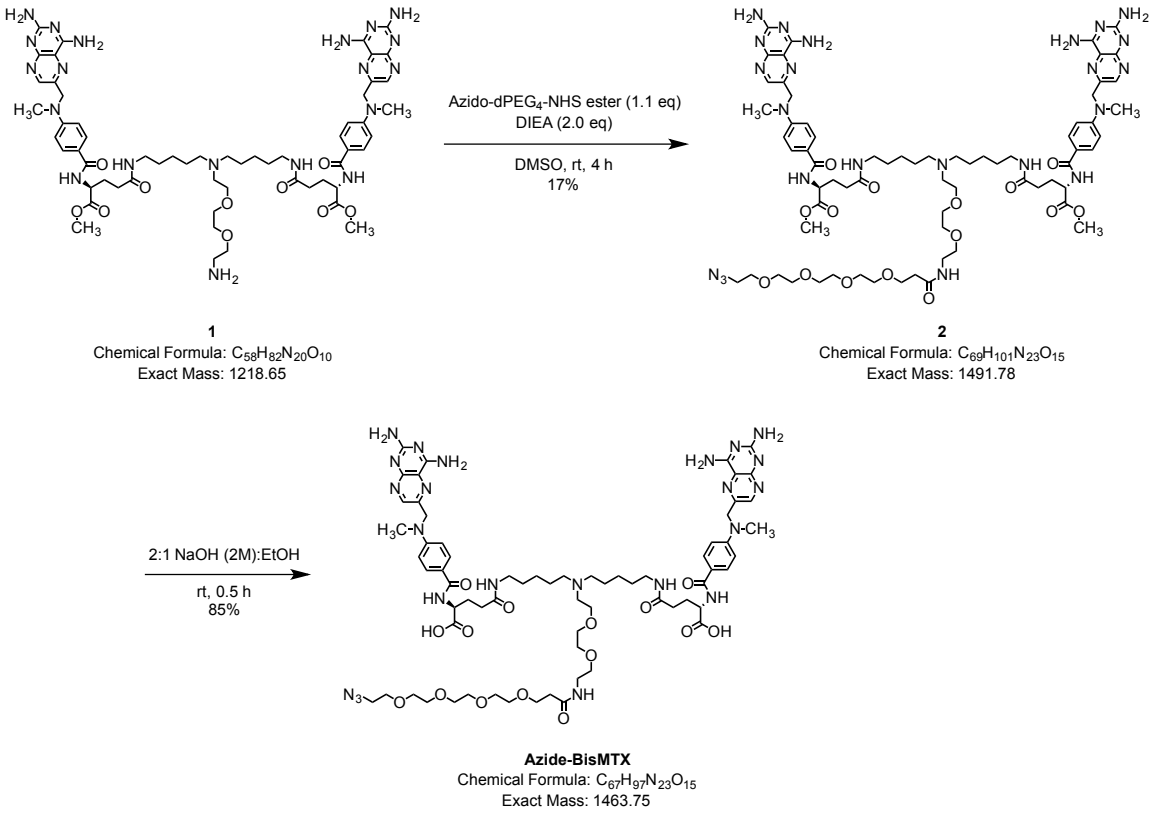

Figure 8A. Synthesis of the Azide-BisMTX Dimerizer. The azide-bisMTX dimerizer was prepared in two steps, starting from the previously-reported compound **1**.[130]

Preparation of 2. Compound **1** (59 mg, 0.048 mmol) and azido-dPEG4-NHS ester (Quanta Biodesign, Cat: 10501; 20 mg, 0.053 mmol) were dissolved in 2.0 mL DMSO and purged under argon. DIEA (20 µL, 0.10 mmol) was added and the solution was stirred for 4 h at rt. The reaction mixture was then purified via reverse-phase chromatography on a 40g C18 column using 25% acetonitrile (0.1% TFA) in water to obtain 12 mg (17%). Low resolution ESI-MS: calculated [$(M+H)^+$] for $C_{69}H_{102}N_{23}O_{15}$ is 1492.8; found 1492.6. Calculated [$(M+2H)^{2+}/2$] $C_{69}H_{103}N_{23}O_{15}$ is 746.9; found 746.8. Calculated [$(M+3H)^{3+}/3$] $C_{69}H_{104}N_{23}O_{15}$ is 498.2; found 498.3.

Preparation of azide-bisMTX. Compound **2** was dissolved in 0.5 mL ethanol followed by 1.0 mL 2 M NaOH. After stirring for 0.5 h, the ethanol was evaporated and the aqueous solution diluted two-fold and neutralized with glacial acetic acid. The mixture was then purified via reverse-phase chromatography using 40% acetonitrile (0.1% TFA) in water to obtain 10 mg (85%). Low resolution ESI-MS: Calculated $[(M+H)^{+}]$ for $C_{67}H_{98}N_{23}O_{15}$ is 1464.8; found 1465.7. Calculated $[(M+2H)^{2+}/2]$ $C_{67}H_{99}N_{23}O_{15}$ is 732.9; found 732.9. Calculated $[(M+3H)^{3+}/3]$ $C_{67}H_{100}N_{23}O_{15}$ is 488.9; found 489.0.

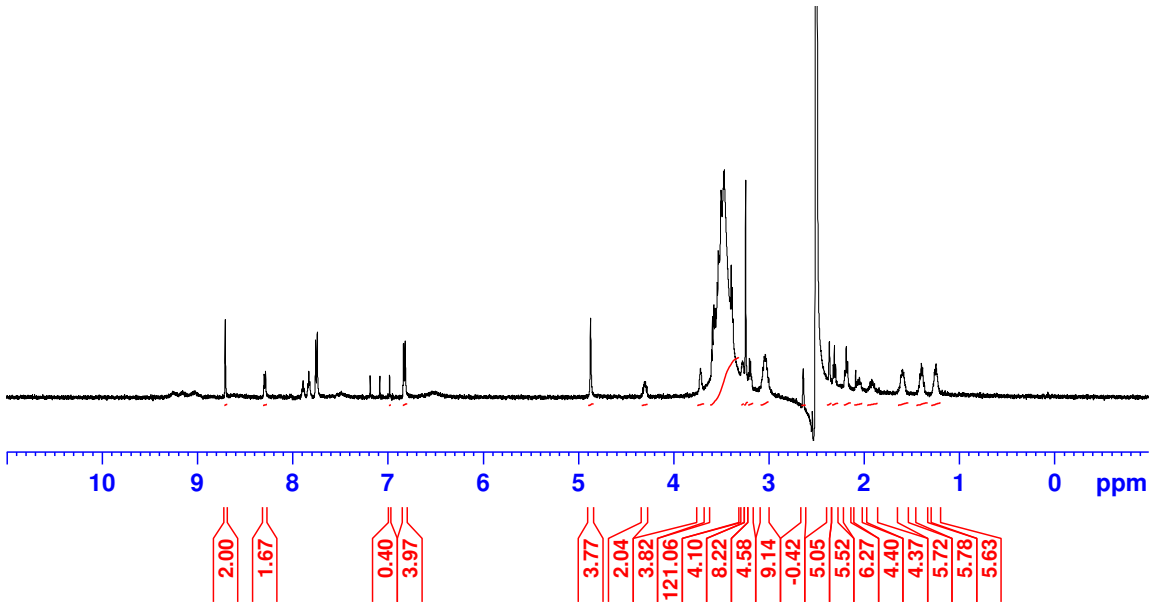

Figure 8B. ^{1}H NMR Spectrum of Azide-BisMTX. Spectrum was collected on a Bruker Ascend 500 NMR in DMSO-*d*^{6}.

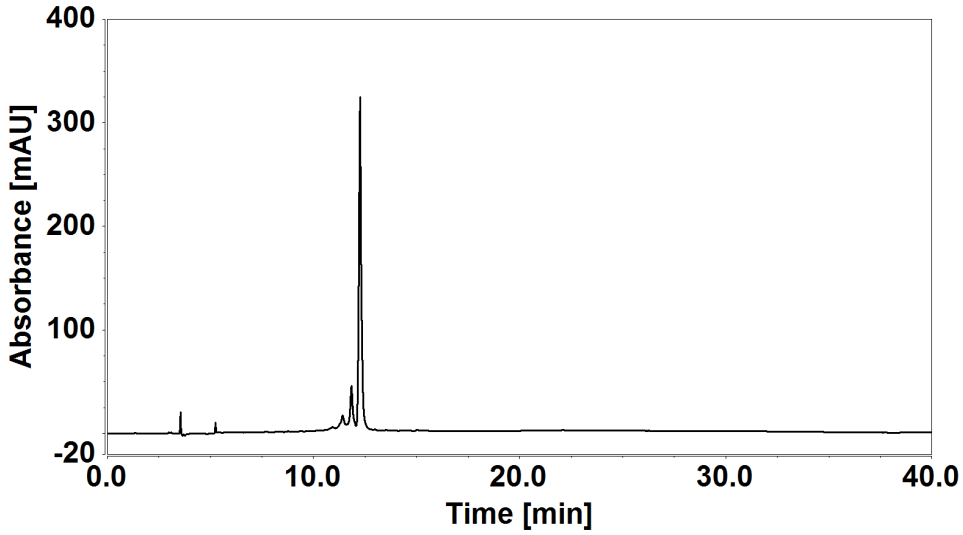

Figure 8C. HPLC Analysis of Azide-BisMTX. Chromatogram was collected on a Thermo Fisher Ultimate 3000 HPLC equipped with a C18 column (Higgins Analytical) in 40% acetonitrile/60% water (with 0.1% TFA).

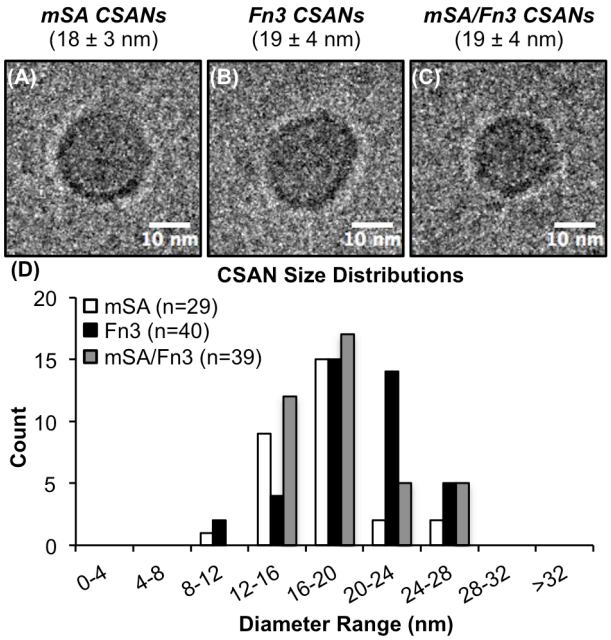

Figure 9. Cryo-EM Characterization of CSAN Species. The formation of (A) mSA CSANs, (B) Fn3 CSANs, and (C) bispecific mSA/Fn3 CSANs was demonstrated by cryo-EM. The values in parentheses represent the mean diameter ± standard deviation of n=29, 40, and 39 nanorings, respectively. (D) The size distribution of mSA, Fn3, and mSA/Fn3 CSANs as assessed by cryo-EM.

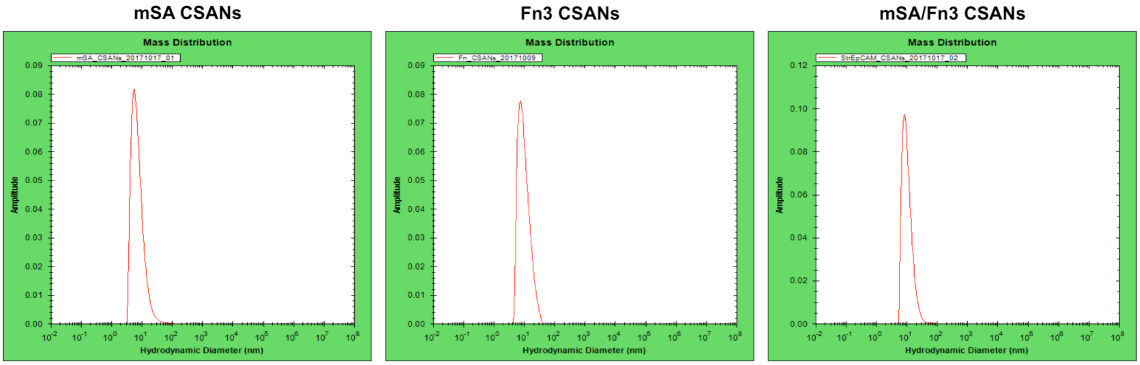

Sample	Hydrodynamic Diameter (nm)	Dispersity
mSA CSANs	17.2 ± 12.4	72.1%
Fn3 CSANs	17.1 ± 10.4	61.0%
mSA/Fn3 CSANs	16.8 ± 12.0	71.5%

Figure 10. DLS Analysis of the Hydrodynamic Diameter of CSAN Species. For analysis, 60 µL of CSANs in PBS was loaded into a cuvette and analyzed on a Punk DLS unit (Unchained Labs). Hydrodynamic diameter values represent the mean ± standard deviation of at least three measurements.

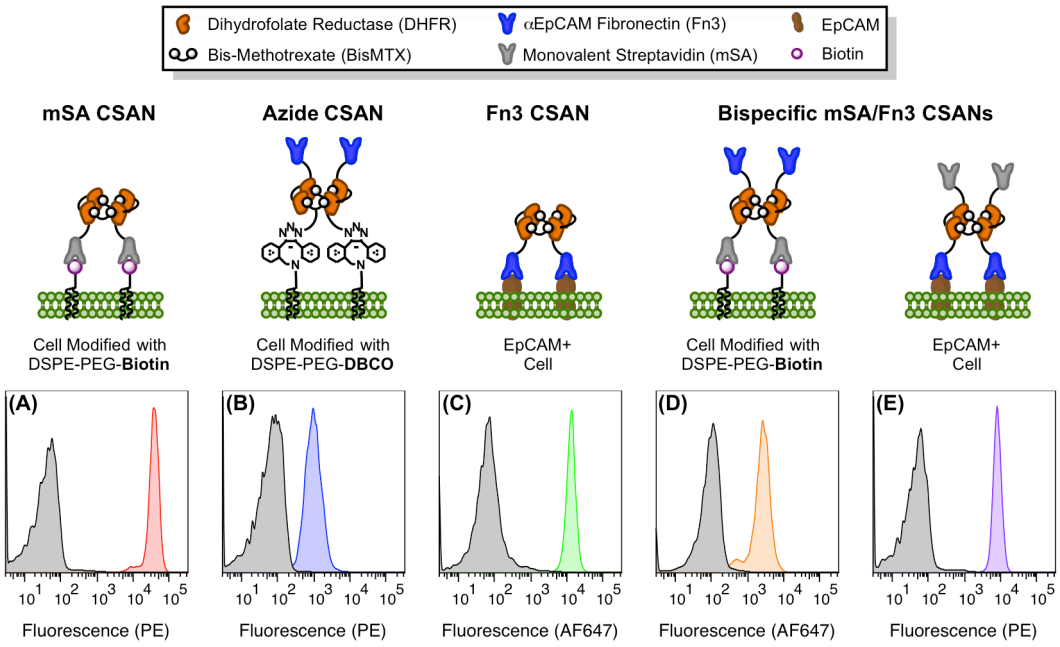

Figure 11. CSANs are Readily Installed on Cells Modified with Phospholipid Conjugates. For all panels, cells were labeled with CSANs through one of several methods and then analyzed by flow cytometry with staining for surface-bound nanorings via either an anti-FLAG phycoerythrin or anti-MYC Alexa Fluor 647 conjugate. The non-specific binding of the antibody-fluorophore conjugate is shown in grey, while the specific detection of the indicated CSAN is shown in color. (A) mSA CSANs bind to MCF-7 cells modified with DSPE-PEG_{2000}-biotin. (B) Fn3 CSANs formed with azide-bisMTX are conjugated to Raji cells modified with DSPE-PEG_{2000}-DBCO. (C) Fn3 CSANs bind to unmodified, EpCAM+ MCF-7 cells. (D) Bispecific mSA/Fn3 CSANs bind to Raji cells modified with DSPE-PEG_{2000}-biotin. (E) Bispecific mSA/Fn3 CSANs bind to unmodified, EpCAM+ MCF-7 cells. All experiments were performed in triplicate, with a representative histogram shown for each scenario.

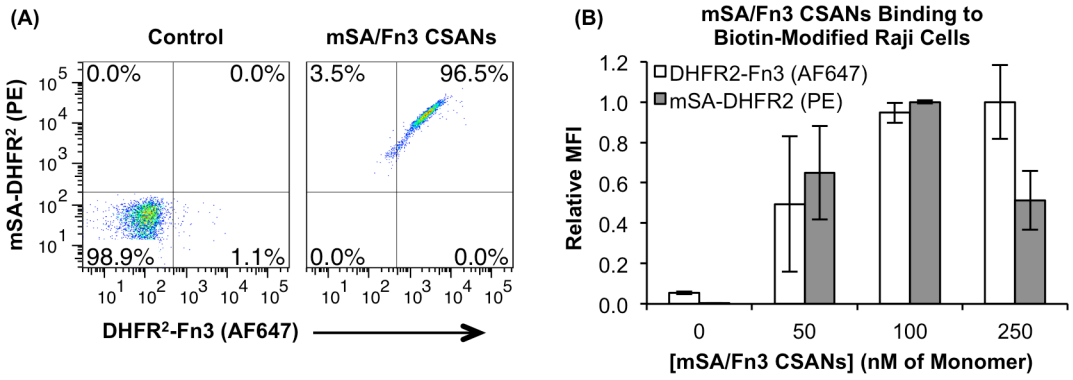

Figure 12. Optimizing the CSAN Labeling Concentration for Biotin-Modified Raji Cells. (A) The presence of both mSA-DHFR^2 and DHFR^2-Fn3 subunits in the CSAN was confirmed via flow cytometry by probing for both the FLAG and MYC epitope tags present on the respective fusion proteins. Briefly, Raji cells were modified with 10 μM DSPE-PEG$_{2000}$-biotin *ex vitro* and labeled with 100 nM mSA/Fn3 CSANs. Cells were then labeled with anti-FLAG PE and anti-MYC (clone 9E10) Alexa Fluor 647 conjugates and analyzed by flow cytometry. As Raji cells do not express EpCAM, the MYC epitope tag would only be present if the DHFR^2-Fn3 subunits were incorporated in the bispecific CSAN (and thereby tethered to the cell surface through the biotin/mSA interaction). (B) Raji cells were modified with 10 μM DSPE-PEG$_{2000}$-biotin *ex vitro*, labeled with various concentrations of mSA/Fn3 CSANs, labeled with anti-FLAG PE and anti-MYC (clone 9E10) Alexa Fluor 647 conjugates, and analyzed by flow cytometry, as described in the methods. Fluorescent signal reached a maximum value at 100 nM of mSA/Fn3 CSANs, with higher concentrations providing the same (or a diminished) signal. This indicates that biotin-modified Raji cell surfaces are saturated with CSANs when labeled with 100 nM of ligand.

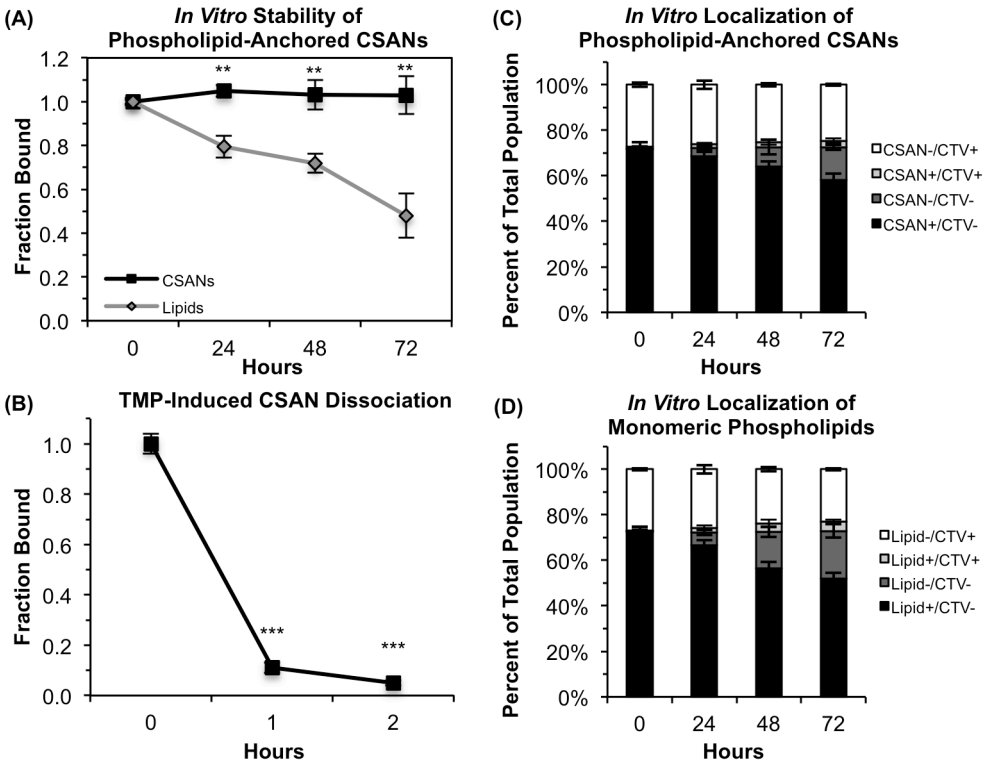

Figure 13. Membrane Stability and Controlled Dissociation of Phospholipid-Anchored CSANs. (A) Biotin-modified Raji cells were labeled with reduced-avidity mSA CSANs and analyzed by flow cytometry every 24 h, staining for either the CSANs (black) or, in the case of the lipid-only control (grey), for biotin. For this analysis, the mean fluorescence intensity (MFI) values are corrected for the number of cell divisions (as determined by CellTrace Violet labeling) and scaled relative to the MFI values obtained at t = 0 h. (B) Biotin-modified Raji cells were labeled with mSA/Fn3 CSANs and then resuspended in culture media with or without 2 μM trimethoprim for 1-2 h at 37 ºC. Cells were then analyzed by flow cytometry to detect the surface-bound CSANs. (C) Biotin-modified Raji cells labeled with reduced-avidity mSA CSANs were pooled with CTV-labeled Raji cells at a 7:3 ratio and co-cultured for 72 h. Cells were analyzed by flow cytometry every 24 h to ascertain whether the lipid-anchored CSANs had migrated onto the membranes of the CTV+ Raji cells. (D) Raji cells modified with only DSPE-PEG_{2000}-biotin (no CSANs) were pooled with CTV-labeled Raji cells at a 7:3 ratio and co-cultured

for 72 h. Cells were analyzed by flow cytometry every 24 h to ascertain whether the phospholipid conjugates had migrated onto the membranes of the CTV+ Raji cells. For all panels, data is presented as the mean ± standard deviation of at least three trials.

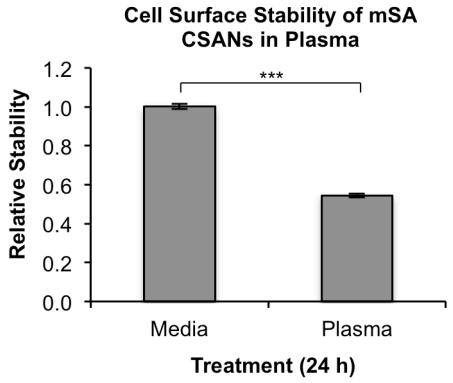

Figure 14. Plasma Stability of Phospholipid-Anchored CSANs. The stability of phospholipid-anchored CSANs in plasma was directly compared to that of media. Raji cells ($2.0x10^6$) were modified with 10 μM DSPE-PEG_{2000}-biotin *in vitro* and labeled with 100 nM "reduced-avidity" mSA CSANs, as described in the methods. The cells were then divided into two aliquots of $1.0x10^6$ cells each; one aliquot was resuspended in 800 μL RPMI while the other was resuspended in 800 μL mouse plasma. The cells were incubated at 37 ºC, 5% CO_2 for 24 h, labeled with anti-FLAG PE conjugate (1 μg/mL in PBS) to detect cell surface CSANs, and analyzed on an LSR II flow cytometer. The MFI of the cells incubated in RPMI was normalized to 1.0 (as the CSANs were shown to be highly stable under these conditions [**Figure 13**]) with the MFI of the cells incubated in mouse plasma scaled accordingly. Compared to 100±1% stability in media, the CSANs exhibited 54±1% stability over 24 h ($p<0.001$). Data is presented as the mean ± standard deviation of three trials.

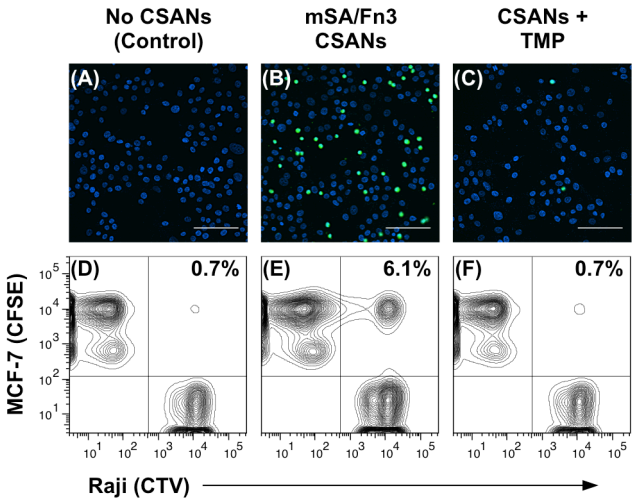

Figure 15. CSANs Direct Reversible Cell-Cell Interactions. For the fluorescence microscopy experiment (top row), Raji cells were sequentially labeled with CFSE, DSPE-PEG_{2000}-biotin and with or without mSA/Fn3 CSANs; they were then incubated with a monolayer of EpCAM+ MCF-7 cells. (A) In the absence of CSANs, the phospholipid-modified Raji cells are unable to interact with the MCF-7 cells. (B) When functionalized with the mSA/Fn3 CSANs, the EpCAM-targeted Raji cells adhere to the MCF-7 cell monolayer. (C) The EpCAM-targeted Raji cells can be dissociated from the MCF-7 cell monolayer by disassembling the CSAN with trimethoprim (TMP). Scale bars in (a-c) represent 100 μm. For the flow cytometry experiment (bottom row), the target MCF-7 cells were labeled with CFSE while the Raji cells were labeled with CTV. Raji cells were again modified with DSPE-PEG_{2000}-biotin and labeled with or without mSA/Fn3 CSANs. (D) In the absence of CSANs, the phospholipid-modified Raji cells are unable to interact with the MCF-7 cells. (E) When functionalized with the mSA/Fn3 CSANs, the EpCAM-targeted Raji cells formed stable clusters with the MCF-7 cells. (F) The Raji/MCF-7 cell clusters were readily dissociated with trimethoprim. Data are representative of replicate (n = 3) experiments.

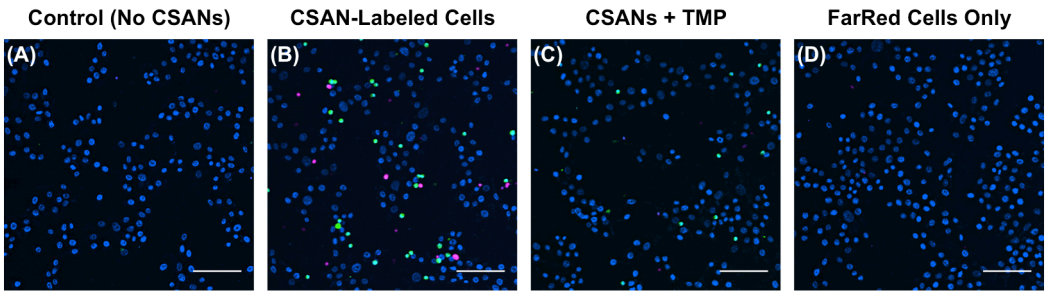

Figure 16. Bioorthogonal CSANs Enable Formation of Multicellular Interactions. For this experiment, three populations of cells were used: (1) EpCAM+ MCF-7 cells adhered to glass coverslips; (2) CFSE-labeled Raji cells sequentially modified with DSPE-PEG_{2000}-biotin and mSA/Fn3 CSANs; and (3) a second population of Raji cells labeled with CellTrace Far Red, DSPE-PEG_{2000}-DBCO, and mSA CSANs oligomerized with azide-bisMTX, granting them the ability to target unoccupied biotin moieties on the CFSE-labeled Raji cells. (A) In the absence of CSANs, neither Raji cell population is able to adhere to the MCF-7 cell monolayer. (B) When functionalized with the CSANs, the two Raji cell populations are able to interact with each other and with the MCF-7 cell monolayer. (C) The cell-cell interactions are largely reversed when the CSAN scaffold is disassembled with trimethoprim. (D) As the Far Red-labeled Raji cells only have the capability of targeting biotin, they are unable to adhere to the MCF-7 cell monolayer in the absence of the CFSE-labeled Raji cells that were modified with DSPE-PEG_{2000}-biotin. Scale bars represent 100 μm.

CHAPTER IV

Assessing the Role of Avidity on Multivalent Ligand Binding to Cell Membrane Antigens

INTRODUCTION

Molecularly targeted agents – including antibodies, bispecific T cell engagers (BiTEs), and chimeric antigen receptor (CAR) T cells – have become a staple of cancer immunotherapy. The therapeutic efficacy of these species is derived from their ability to recognize a specific antigen on the surface of a malignant cell. However, many of the antigens targeted by these agents are not exclusive to the neoplasm, and the recognition of healthy tissue that also expresses the antigen has led to adverse events known as "on-target, off-tumor" toxicities.[59, 122] Such toxicities have both restricted and prevented the clinical use of otherwise promising treatments.

For example, CAR T cells targeting the pan-B cell marker CD19 are remarkably efficacious for certain B cell neoplasms, but the recognition and eradication of healthy B cells leads to aplasia.[124, 137] Furthermore, CAR T cells recognizing ERBB2[138], carbonic anhydrase IX (CAIX)[125], and carcinoembryonic antigen (CEA)[139], yielded potent solid organ toxicities that, in some cases, halted further development. Likewise, BiTEs[140, 141] and antibodies[142, 143] targeting epithelial cell adhesion molecule (EpCAM) produced dose-limiting colitis and hepatotoxicity, respectively. Nevertheless, each of these antigens remains under clinical investigation due to their promise as oncologic targets, provided the tumor specificity profiles can be improved.

Accordingly, many groups have sought strategies to mitigate on-target, off-tumor toxicities. One approach is to reduce the binding affinity of the targeting agent such that there is insufficient avidity to stably recognize the lower level of antigen expression on the healthy tissue.[144, 145] Indeed, CAR T cells utilizing reduced affinity single chain variable fragments (scFvs) targeting ERBB2[145], EGFR[144, 145], ICAM-1[146], CD38[147], and CD123[148] exhibited reduced cytotoxicity towards antigen^{Low} cell lines *in vitro* and

increased therapeutic windows in murine xenograft models. Likewise, enhancements in selectivity have been observed for nanoparticles[149-151] and dendrimers[152-154] when either the affinity or valency of the binding domains are reduced. These studies suggest that avidity optimization may be an effective strategy to reduce on-target, off-tumor recognition by these highly multivalent agents.

Most protein-based scaffolds – such as antibodies and their various formats – present a unique challenge, as the small number of potential ligand/cell interactions limits their avidity for the target cell. Theoretical models[155-159] and analytical experiments[160-162] have indicated that avidity optimization could enhance the selectivity of these species as well; however, there is very limited work demonstrating this phenomenon *in vitro*[163, 164] and *in vivo*[165]. Furthermore, none of these studies have directly examined all facets of avidity (i.e., binding affinity, ligand valency, and antigen expression density) nor have any used non-antibody protein topologies. Thus, the present study aims to translate the theoretical models into both *in vitro* and *in vivo* results using a soluble protein scaffold with variable ligand affinity and valency, plus a small panel of cell lines with different antigen expression densities.

For this, we utilized a protein scaffold previously developed by our group, called the chemically self-assembled nanoring (CSAN; **Figure 1**).[127] CSANs are formed when bivalent dihydrofolate reductase ($DHFR^2$) fusion proteins are spontaneously oligomerized by a chemical dimerizer, bis-methotrexate (bisMTX).[127, 128] CSANs can be further functionalized by fusing various binding entities to the $DHFR^2$ subunits.[29, 131, 166] In this work, human tenth type III fibronectin (Fn3) domains with either no binding efficacy (i.e., a non-targeted control domain) or with engineered specificity for a model antigen, EpCAM[102], were fused. By co-assembling defined, stoichiometric ratios of these targeted

and non-targeted subunits, CSANs with distinct EpCAM-targeting valencies were formed. We hypothesized that by varying the affinity and valency of the Fn3 domains in the CSAN, we could prepare a scaffold capable of binding specifically to cells that overexpress EpCAM but with limited binding to cells expressing low quantities of EpCAM. Accordingly, we titrated a number of these avidity-modulated CSANs against various EpCAM-expressing cell lines, enabling us to quantitate the apparent affinity of the scaffold in the context of variable Fn3 affinities, valencies, and EpCAM-expression densities. These results were then applied to the development of avidity-optimized CSANs capable of performing cellular discrimination both *in vitro* and *in vivo*.

RESULTS AND DISCUSSION

Scaffold Apparent Affinity Varies Quantitatively as a Function of Ligand Valency

We previously reported the development of a panel Fn3 domains with engineered specificity for EpCAM[102], which is overexpressed on a wide range of epithelial malignancies (i.e., carcinomas)[83, 84] and certain cancer stem cell populations.[78, 85] For this work, we fused two of these ligands – the "high-affinity" clone C5 (K_d = 17 ± 1 nM) and the "low-affinity" clone B22 (K_d = 1,100 ± 200 nM) – to our DHFR^2 subunits, enabling the formation of EpCAM-targeted CSANs (**Figure 1**). Similarly, we fused a "non-targeted" Fn3 domain (termed clone NT) with no binding efficacy to serve as a negative control.

Due to the self-assembling nature of the CSANs, bispecific CSANs incorporating two distinct targeting domains can be formed by incubating mixtures of the desired DHFR^2 fusion proteins with bisMTX.[29, 131, 166] Furthermore, our previous characterization of the CSAN platform has demonstrated that, while a narrow distribution of species are formed during the self-assembly process, the most abundant[127] and mass-average[128] moiety is

an octameric nanoring displaying eight targeting domains. Thus, we hypothesized that mixing stoichiometric ratios of an EpCAM-targeted $DHFR^2$-Fn3 fusion protein with the non-targeted $DHFR^2$-Fn3 fusion protein would enable the formation of CSANs exhibiting "reduced valency" of the EpCAM-binding Fn3s, given that the non-binding domains would now occupy a defined number of positions within the predominantly octameric scaffold (**Figure 2A-B**). In turn, these reduced valency CSANs would exhibit a corresponding lower affinity for EpCAM-expressing cells, with a direct correlation between the CSAN's overall apparent affinity and the valency of its EpCAM-binding domains.

To test this hypothesis, we assembled defined ratios of EpCAM-targeted $DHFR^2$-Fn3 subunits (utilizing either clone C5 or B22) and non-targeted $DHFR^2$-Fn3 subunits into CSANs with distinct EpCAM-binding valencies (**Figure 2A-B**). As in our previous work with $DHFR^2$-Fn3 fusion proteins, complete CSAN oligomerization was observed within 30 min of the addition of bisMTX, as demonstrated by size exclusion chromatography (SEC; **Figure 3**).[128, 129] Oligomerized CSANs were further characterized by dynamic light scattering (DLS; **Figure 4**) with results in close agreement to those previously reported for Fn3-targeted CSANs.[29]

We then titrated each of these CSAN species – with targeted:non-targeted (T:NT) domain ratios of either 8:0 (i.e., fully targeted), 4:4, 2:6, or 1:7 (i.e., a single targeting domain) – against the EpCAM-expressing cell line, MCF-7, using flow cytometry. As predicted, the apparent affinity of the CSAN scaffold varied directly with the proportion of EpCAM-binding Fn3 domains incorporated into the nanoring (**Figure 2C-F**). Indeed, this relationship was true for both of the Fn3 clones tested, C5 (**Figure 2C**) and B22 (**Figure 2D**). The apparent $K_{d,N}$ values obtained for each Fn3 clone and valency tested are given

in **Table 1**. For clarity, the abbreviation $K_{d,N}$ will be used throughout the text to distinguish multivalent apparent affinities from true monomeric dissociation constants, depicted as the traditional K_d. That the $K_{d,1}$ values for the monovalent 1:7 T:NT species are higher than those of the parent ligands suggests a thermodynamic penalty for fusing these ligands to DHFR[2] domains and further organizing them into nanorings. Importantly, CSANs composed solely of the non-targeted subunits (i.e., T:NT ratio of 0:8) exhibited no binding to the EpCAM-positive cells (**Figure 5**).

To quantitatively define the effect of a multivalent scaffold's valency on its apparent affinity, the obtained $K_{d,N}$ values were plotted against the number of targeting domains incorporated into the nanoring (**Figure 6**). This analysis yielded a consistent descriptor of how the CSAN's apparent affinity changes as a function of both the singly-targeted ligand's affinity ($K_{d,1}$, units of molarity) and the valency (N, unit-less number of ligands per scaffold) of the binding domains:

(**Eq. 1**) $Apparent\ K_{d,N} = \frac{K_{d,1}}{N^2}$

Note that this equation form is based purely on empiric observations and may not represent the underlying mechanistic relationship. This data can also be considered in terms of the cooperativity parameter, α (***equation 2***), and the enhancement parameter, β (***equation 3***)[167]:

(**Eq. 2**) $K_{d,N} = \left(K_{d,N}\right)^{\alpha N}$

(**Eq. 3**) $K_{d,N} = \beta K_{d,1}$

Multivalent interactions are characterized as positively cooperative when $\alpha > 1$, non-cooperative when $\alpha = 1$, and negatively cooperative when $\alpha < 1$.[152] Like other well-characterized multivalent targeting scaffolds[152, 167], the CSANs exhibit values of $\alpha < 1$, indicating that they, too, are negatively-cooperative (**Table 1**). This negative cooperativity could be a result of steric hindrance that impedes highly multivalent binding in spite of the increased local concentration that results from scaffold tethering to the cell surface. Furthermore, the β values show up to 78-fold enhancement of the binding affinity for fully-targeted CSANs (**Table 1**).

Antigen Expression Density Impacts Scaffold Apparent Affinity

Cellular discrimination based upon antigen expression levels necessitates that antigen quantity be a predictive variable in a multivalent scaffold's apparent affinity calculation. Therefore, we sought to more clearly define the role of EpCAM expression density on the CSANs' cell-binding potential and incorporate this analysis into ***equation 1***.

Using flow cytometry, EpCAM expression was quantitatively defined for a small panel of cell lines, including MDA-MB-231 (5.2×10^4 EpCAMs/cell), SK-OV-3 (2.2×10^5 EpCAMs/cell), LNCaP (2.8×10^6 EpCAMs/cell), and MCF-7 (3.8×10^6 EpCAMs/cell; **Figure 7A-D**, respectively). Fully-targeted CSANs (T:NT 8:0) utilizing the high-affinity Fn3 clone C5 were titrated against each of these cell lines via flow cytometry, yielding apparent $K_{d,N}$ values of 27 ± 2.8 nM, 19 ± 3.4 nM and 7.2 ± 3.7 nM, and 6.9 ± 1.8 nM, respectively. Plotting these $K_{d,N}$ values against the absolute EpCAM expression per cell afforded a local, yet descriptive, model of how the apparent affinity is affected by a reduction in the antigen expression density (**Figure 7E**) within this regime. As expected, minor reductions in expression – for instance, from 3.8×10^6 EpCAMs/cell (MCF-7) to

$2.8x10^6$ EpCAMs/cell (LNCaP) – have an insignificant impact on the CSAN's apparent affinity ($p > 0.8$). However, larger differences in antigen density – from $3.8x10^6$ EpCAMs/cell (MCF-7) to $5.2x10^4$ EpCAMs/cell (MDA-MB-231) – showed a marked reduction (approximately four-fold; $p < 0.001$) in the apparent affinity (**Figure 7E**).

Analogous to biparatopic antibodies[157, 168, 169], this phenomenon is supported by a biophysical model of how CSANs might bind to cell membranes decorated with target antigens (**Figure 8**). Briefly, the known radius of the CSANs[29, 166] permits calculation of the cell surface area and extracellular volume accessible to the nanoring. Having quantitated the EpCAM expression of the various cell lines, both the number (**Figure 7F**) and effective molarity (**Figure 7G**) of EpCAM moieties present in the accessible area and volume, respectively, can be calculated. As shown, the model of EpCAM accessibility supports the trend in cell binding efficacy observed in **Figure 7E**, where similar $K_{d,N}$ values are observed for the high-expressing cell lines (MCF-7 and LNCaP) and reduced affinity is observed for the low-expressing cell lines (MDA-MB-231 and SK-OV-3). Additional details regarding this model (including assumptions and numerical values) are discussed in the **Figure 8** caption.

Combining our observations with the proposed model, we sought to estimate the minimum EpCAM density required to enable fully octavalent binding of a CSAN to a cell membrane. Using ***equation 1***, the observed $K_{d,N}$ values for the fully-targeted CSANs against the MCF-7, LnCAP, SK-OV-3, and MDA-MB-231 cells were converted to estimated binding valencies of N = 8, 8, 5, and 4, respectively. This suggested that the CSANs could bind octavalently to the MCF-7 and LNCaP cells, but only pentavalently to the SK-OV-3 cells and tetravalently to the MDA-MB-231 cells. Per the data in **Figure 7F**, this pattern of binding is most consistent with a threshold number of accessible antigens

between 0.042 – 0.057 EpCAMs, as this "cut off" permits eight binding events for the MCF-7 and LNCaP cells, but only five and three for the SK-OV-3 and MDA-MB-231 cells, respectively. Thus, the threshold is estimated as the midpoint of this range, 0.049 EpCAMs, and that value is represented by the horizontal black dashed line in **Figure 7F**. This corresponds to 7.7×10^5 EpCAMs/cell, as indicated by the red point in **Figure 7E**; likewise, the upper and lower bounds of this range are represented by the projected red dashed lines. See **Figure 8** for further details. Collectively, this data suggests that CSANs are unlikely to discriminate between cells expressing $\geq 7.7 \times 10^5$ antigens/cell. Below this threshold, however, the CSANs are no longer capable of engaging in fully octavalent interactions with the cell surface, thus lowering the avidity for the target cell and decreasing the apparent $K_{d,N}$ value.

Incorporating the antigen expression (*R*, number of receptors/cell) analysis into ***equation 1*** provided an updated view of the holistic relationship:

(**Eq. 4**) $$Apparent\ K_{d,N} = \frac{K_{d,1}}{N^2} \cdot \frac{150}{R^{0.33}} = \frac{150 \cdot K_{d,1}}{N^2 \cdot R^{0.33}}$$

Of note, ***equation 4*** is merely a local empirical model of how the $K_{d,N}$ value changes within this regime of antigen expression densities (*R*). This is highlighted by the fact that, as *R* approaches infinity, the fold-change in $K_{d,N}$ (and thus $K_{d,N}$ itself) approaches zero. Thus, the model may overestimate the apparent affinities of multivalent ligands towards cells with very high numbers of antigens/cell; however, we note such densities are unlikely to be encountered in physiologic settings. For these studies, the $K_{d,N}$ value for the MCF-7 cells was set as the reference point (i.e., fold-change = 1.0) as it was the highest-expressing cell line in our panel, and because the next highest-expressing cell

line (LNCaP) provided a $K_{d,N}$ value that was not significantly different, suggesting the physiologic maximum $K_{d,N}$ had been reached (**Figure 7E**). Finally, because the antigen expression term of ***equation 4*** was constructed using data from only the fully-targeted CSANs (T:NT 8:0) displaying clone C5, we tested the predictive capacity of the equation by calculating the apparent $K_{d,N}$ values for reduced-valency CSANs against the various cell lines. As shown in **Table 2**, ***equation 4*** predicts $K_{d,N}$ values that are within reasonable agreement with the experimentally-determined dissociation constants, suggesting that this is an appropriate model for predicting CSAN apparent affinities based upon the variables that compose the avidity of the scaffold/cell interaction.

Affinity and Valency Tuning Enables Target Discrimination In Vitro

We next explored whether modulating the CSAN's avidity could reduce binding to $EpCAM^{Low}$ cells while maintaining binding to $EpCAM^{High}$ cells. EpCAM-targeted CSANs of different T:NT ratios (either 8:0 or 4:4) were titrated against each of the EpCAM-expressing cell lines in parallel via flow cytometry. A fully-targeted CSAN utilizing the high-affinity Fn3 clone C5 (8:0 C5:NT) bound appreciably to all cell lines (**Figure 9E-H**). However, reducing the valency of the Fn3 in the CSAN (4:4 C5:NT), yielded a construct that still bound well to the MCF-7, LNCaP, and SK-OV-3 cells but exhibited greatly diminished binding to the MDA-MB-231 cells (**Figure 9I-L**). These observations suggest that valency reduction may be a viable strategy for enabling cellular discrimination.

Likewise, a fully-targeted CSAN utilizing the low-affinity Fn3 clone B22 (8:0 B22:NT) bound strongly to both the $EpCAM^{High}$ MCF-7 and LNCaP cells; however, binding was undetectable against the $EpCAM^{Low}$ SK-OV-3 and MDA-MB-231 cells (**Figure 9M-P**), suggesting that affinity reduction – in this case, by a factor of approximately of 65-fold between the parent Fn3 clones – may be sufficient to enable target cell discrimination, at

least *in vitro*. As expected, reducing the valency of Fn3 clone B22 in the CSAN (4:4 B22:NT) marginally reduced the binding to MCF-7 and LNCaP cells, while binding to the SK-OV-3 and MDA-MB-231 cells remained undetectable (**Figure 9Q-T**). Data shown in **Figure 9** represents CSAN binding at 50 nM, though the same trends were observed at all CSAN concentrations tested (i.e., 5, 50, and 500 nM; **Figure 10**).

Notably, the CSANs utilizing the low-affinity Fn3 clone B22 exhibited "switch-like" discrimination between the $EpCAM^{Low}$ ($5.2x10^4$ – $2.2x10^5$ EpCAMs/cell) and $EpCAM^{High}$ ($2.8x10^6$ – $3.8x10^6$ EpCAMs/cell) cell lines, with essentially no binding efficacy towards the MDA-MB-231 and SK-OV-3 cells but robust binding to the LNCaP and MCF-7 cells (**Figure 9U**). This phenomenon was diminished in the CSANs utilizing the high-affinity Fn3 clone C5, and entirely absent in the positive control samples where the antibody bound very well to all cell lines. Theoretical models of "super selectivity" have postulated that this on-off binding pattern can be achieved by multivalent nanoparticles when the affinity of the individual ligand-receptor interactions is low because the number of distinct binding arrangements increases in a non-linear way with respect to antigen density.[156] Indeed, the experimental results in **Figure 9** are in direct agreement with this model.

Collectively, these results demonstrate that the avidity of a multivalent targeting scaffold can be tuned to enable discrimination between cell populations expressing distinct quantities of the cognate antigen. To this end, reducing either the affinity of the binding ligand, the valency of the binding domains, or both are all viable approaches.

Avidity Optimization Yields Tunable Biodistribution In Vivo

Lastly, we evaluated whether the principles of avidity modulation determined *in vitro* would translate to an *in vivo* setting. Four week old, male, athymic nude (NU/J) mice

were xenografted with an EpCAM^{High} MCF-7 tumor ($3.8x10^6$ EpCAMs/cell) on the left flank and an EpCAM^{Low} MDA-MB-231 ($5.2x10^4$ EpCAMs/cell) tumor on the right flank. We hypothesized that high-avidity CSANs (i.e., high affinity and/or valency) would distribute to both tumors regardless of EpCAM expression while low-avidity CSANs (i.e., reduced affinity and/or valency) would preferentially distribute to the high EpCAM-expressing tumor (i.e., MCF-7 tumor).

After two weeks, when tumors had grown to 8-12 mm in diameter, mice were randomly assigned to one of five groups (n = 3 mice/group): (1) 0:8 T:NT CSANs; (2) 8:0 C5:NT CSANs; (3) 4:4 C5:NT CSANs; (4) 8:0 B22:NT CSANs; and (5) 4:4 B22:NT CSANs. For this experiment, the CSANs were oligomerized with a previously-synthesized bisMTX analog that incorporates the copper-64 (^{64}Cu) radiochelator, DOTA[129]; as with our previous work using bisMTX analogs[29, 129, 130], all DHFR^2-Fn3 monomers completely oligomerized into CSANs within 30 min of the addition of the DOTA-bisMTX (**Figure 11**).

Two weeks after tumor engraftment, mice in each group were given an intravenous (tail vein) injection of the indicated CSAN radiolabeled with ^{64}Cu. After 18 h, mice were euthanized and tissues were collected for gamma counting to assess the *in vivo* biodistribution of the CSANs (**Figure 12**). The non-targeted control CSAN (0:8 T:NT) distributed to both tumors equally at a level commensurate with background tissue uptake (**Figures 12 & 13**). The highest avidity CSAN (8:0 C5:NT) exhibited significantly greater uptake in both tumors relative to the control ($p \leq 0.02$). Further, it was unable to effectively discriminate between the tumors, exhibiting similar uptake in both the MCF-7 tumor (5.0 ± 1.8 %ID/g) and MDA-MB-231 tumor (5.3 ± 1.4 %ID/g) regardless of EpCAM expression (**Figure 13**). Reducing the valency of the C5 domain (4:4 C5:NT) did not affect uptake in the MCF-7 tumor (4.2 ± 1.1 %ID/g); however, uptake by the MDA-MB-

231 tumor was reduced (2.5 ± 0.4 %ID/g; $p < 0.03$) though not ablated. Though trending towards a selective preference for the MCF-7 tumor, targeting to the respective tumors was not significantly different ($p = 0.07$) for this construct (**Figure 13**). Reducing only the affinity of the CSAN (8:0 B22:NT) exhibited a similar pattern, again with unchanged MCF-7 tumor uptake (5.0 ± 1.5 %ID/g) and reduced MDA-MB-231 tumor uptake (2.6 ± 0.2 %ID/g; $p < 0.03$). In this case, however, discrimination between the two tumors did reach statistical significance, albeit barely ($p < 0.05$; **Figure 13**). Finally, reducing both the affinity and valency of the CSAN (4:4 B22:NT) provided sustained MCF-7 tumor uptake (3.9 ± 0.8 %ID/g) and statistically insignificant uptake in the MDA-MB-231 tumor (2.0 ± 0.3 %ID/g; $p > 0.07$ relative to control). Accordingly, there was a significant preference for the MCF-7 tumor over the MDA-MB-231 tumor ($p < 0.03$), collectively indicating targeting specificity (**Figure 13**).

All targeted CSANs exhibited significant uptake by the $EpCAM^{High}$ MCF-7 tumor, regardless of their avidity ($p < 0.03$ for all species relative to control). This is similar to the *in vitro* flow cytometry observations where all constructs exhibited robust MCF-7 cell binding. Likewise, a 50% reduction in CSAN valency alone (4:4 C5:NT) was insufficient to ablate binding to the relatively $EpCAM^{Low}$ MDA-MB-231 cells both *in vivo* ($p < 0.01$) and *in vitro*. In contrast, affinity reduction alone (8:0 B22:NT) only eliminated MDA-MB-231 cell binding *in vitro*, whereas the construct still exhibited significant MDA-MB-231 tumor uptake *in vivo* ($p < 0.001$) to a level similar to the 4:4 C5:NT CSAN. Only reduction of both affinity and valency (4:4 B22:NT) yielded durable cellular discrimination both *in vitro* and *in vivo*. The minor discrepancies between the *in vitro* and *in vivo* results indicate that, not unsurprisingly, there are additional factors *in vivo* that will influence the biodistribution of these scaffolds; while *in vitro* work can help design candidate scaffolds,

a small panel of prioritized molecules should be evaluated *in vivo* to identify idiosyncrasies and the most promising targeting construct(s).

Interestingly, the *in vivo* tumor targeting profile correlated with the apparent affinity of the scaffolds. The highest affinity construct (8:0 C5:NT) has a $K_{d,N}$ value on the order of 10^{-9} M and exhibited equivalent uptake by both tumors. The two scaffolds with $K_{d,N}$ values of 10^{-8} M (4:4 C5:NT and 8:0 B22:NT) demonstrated a degree of selectivity, with diminished targeting to the MDA-MB-231 tumor. Finally, the lowest-affinity scaffold with a $K_{d,N}$ of 10^{-7} M (4:4 B22:NT) targeted the high-expressing MCF-7 tumor specifically. This result is consistent with other work highlighting the benefit of low-nanomolar (or subnanomolar) affinities for robust tumor targeting across a range of antigen expression levels.[112, 170-173]

As suggested by the quantitative *in vitro* analyses (***equation 4***), it is possible that further valency reduction alone – e.g., to 2:6 C5:NT – could have also afforded complete tumor discrimination *in vivo*. Indeed, the 2:6 C5:NT CSANs exhibited a similar apparent affinity to the 4:4 B22:NT CSANs when titrated against the MCF-7 cells (140 ± 40 nM vs. 150 ± 80 nM, respectively; **Figure 6**). In the same manner, a further reduction in affinity alone – via the fusion of an even lower affinity parent Fn3 clone (e.g., B17 with a K_d of 3.1 ± 0.8 μM[102]) – may afford discrimination without the need for valency reduction. Finally, while the MDA-MB-231 cells express a relatively low level of EpCAM, it is still a malignant breast cancer cell line that may aberrantly express EpCAM relative to normal, healthy tissue. Therefore, CSANs that distributed to this tumor may or may not be taken up by healthy tissue. However, the use of such a cell line in this discrimination study (and others) may be highly valuable as a "built-in" safety margin, as a lack of binding to the MDA-MB-231 xenograft could be highly predictive of a lack of recognition of normal

epithelium. The results of ongoing studies addressing these numerous possibilities will be reported in due course.

CONCLUSIONS

Using a modular self-assembling protein nanoring, this work demonstrates that the overall, apparent affinity of multivalent targeting scaffolds varies as a function of monomeric ligand affinity, binding domain valency, and cellular antigen expression density. The relationship between these variables was elucidated *in vitro* and then translated *in vivo* to identify scaffolds capable of specifically targeting cells that overexpress the target antigen. Thus, this work provides insight into the future design of multivalent scaffolds that could be used for a host of applications, including therapeutic drug conjugates and diagnostic imaging agents.

The model antigen in these studies, EpCAM, has been extensively explored as a clinical candidate, as its overexpression on carcinomas and presence on several types of CSCs make it a potentially useful target. Unfortunately, on-target, off-tumor toxicities – primarily in colonic and hepatic epithelia[140] – have prevented the FDA approval of EpCAM-directed therapies. Currently, the only clinically-used EpCAM-targeted agent is catumaxomab, a rat/mouse hybrid monoclonal antibody approved in the European Union (EU) for localized treatment of malignant ascites.[142] However, this work suggests that avidity optimization of the binding scaffold may be a viable strategy to enable the clinical targeting of EpCAM and other promising, yet promiscuous, antigens.

Pre-clinical work with CAR T cells has demonstrated that avidity optimization is a viable strategy for reducing on-target, off-tumor toxicities in that platform. Not unsurprisingly,

the same variables identified in those studies – binding affinity, ligand expression/valency, and target density – have been found here to be crucial for soluble, multivalent targeting scaffolds as well. Arcangeli *et al.* suggested that CAR T cells using ligand affinities in the range of 10^{-7} M could offer a better safety profile compared to higher affinity constructs[148]; here, the only CSAN capable of completely discriminating between the EpCAM^{High} and EpCAM^{Low} xenograft tumors had an apparent affinity in this range ($K_{d,N}$ = 1.5x10^{-7} M), while the higher-affinity constructs exhibited measurable uptake by both tumors ($K_{d,N}$ values of 3.3x10^{-8} – 6.9x10^{-9} M). Whether this shared 10^{-7} M affinity threshold is merely a coincidence or represents a meaningful barrier for off-tumor toxicities remains to be seen.

Finally, a limitation of this work is that it was completed using a single scaffold, the CSAN. While the fundamental relationship between affinity, valency, and expression are likely to translate to other scaffolds, we caution that the specific numerical values (i.e., the exponents and numerator constant) in ***equation 4*** may be different for other geometries, such as multi-specific antibodies and linear fusions of tandem alternative protein topologies (e.g., Fn3s, affibodies, designed ankyrin protein repeats, etc.). As other groups with specialties in these ligands and formats explore avidity optimization in their scaffolds, we are enthusiastic that the field as a whole will develop a collective set of design principles and thresholds that will facilitate the clinical use of these unique constructs for the targeting of difficult yet promising tumor associated antigens.

MATERIALS AND METHODS

Cells and Cell Culture

The MCF-7, LNCaP, SK-OV-3, and MDA-MB-231 cell lines were previously purchased from the American Type Culture Collection (ATCC). MCF-7 and MDA-MB-231 cells were

grown at 37 ºC in a humidified atmosphere with 5% CO_2 in Dulbecco's Modified Eagle's Medium (DMEM) with 4.5 g/L glucose, L-glutamine, and supplemented with 10% fetal bovine serum (FBS), 100 U/mL penicillin, and 100 µg/mL streptomycin. LNCaP and SK-OV-3 cells were grown at 37 ºC in a humidified atmosphere with 5% CO_2 in Roswell Park Memorial Institute (RPMI) media with L-glutamine and supplemented with 10% FBS, 100 U/mL penicillin, and 100 µg/mL streptomycin. For passaging, cells were detached via trypsin. Cell count and viability were determined via trypan blue exclusion using a Bio Rad TC20 automated cell counter (Bio Rad Laboratories, Inc.).

Expression Plasmids

A gBlock Gene Fragment coding for the $DHFR^2$-Fn3 clone C5 fusion protein was ordered from Integrated DNA Technologies (IDT) and cloned into the Novagen pET28a(+) vector (EMD Millipore, Cat: 69864-3) via *NcoI* and *XhoI* restriction sites. Separately, Fn3 clones B22 and NT replaced clone C5 using designed *NheI* and *BamHI* restriction sites flanking the Fn3 sequence region. Notably, the $DHFR^2$-Fn3 proteins contain an *N*-terminal MYC epitope tag and *C*-terminal polyhistidine tag to facilitate detection via flow cytometry and purification via immobilized metal affinity chromatography (IMAC), respectively.

Protein Expression and Purification

$DHFR^2$-Fn3 fusion proteins were expressed in *Escherichia coli* (*E. coli*) and purified from the soluble fraction of the cell lysates by IMAC.[29] Purified proteins were analyzed by SEC on a Superdex 200 Increase 10/300 gel filtration column (GE Healthcare Life Sciences, Cat: 28990944) in phosphate buffered saline (PBS, pH 7.4) running buffer. Fusion protein retention times were compared to those of commercial molecular weight standards (Sigma Aldrich, Cat: MWGF1000-1KT).

CSAN Formation and Characterization

CSANs were formed by adding a 3-fold molar excess of the desired chemical dimerizer (either bisMTX or DOTA-bisMTX) to a solution of $DHFR^2$-Fn3 fusion protein monomers in PBS. Consistent with our previous studies, CSAN oligomerization occurred within 30 minutes of adding the dimerizer.[127] Oligomerized CSANs were analyzed by SEC (as described above) and dynamic light scattering (DLS). For DLS, 60 µL of CSANs in PBS was loaded into a cuvette and analyzed on a Punk DLS unit (Unchained Labs). Hydrodynamic diameter values represent the mean ± standard deviation of at least three measurements. SEC and DLS results were consistent with our previous analyses of Fn3-targeted CSANs, including cryo-electron microscopy (cryo-EM) evidence of nanoring formation.[29, 166]

Apparent Affinity Determination of Fn3-Targeted CSANs

The apparent affinity of the Fn3-targeted CSANs was determined by flow cytometry, as previously described.[102] Briefly, EpCAM-expressing cells (MCF-7, LNCaP, MDA-MB-231 lines) were cultured to approximately 80% confluency, detached, and counted, as described above. Aliquots of $5x10^4$ cells were washed with PBSA (PBS with 0.1% w/v bovine serum albumin) and labeled with varying concentrations of Fn3-targeted CSANs for ≥90 min at 4 ºC. Cells were then pelleted (8,000 g, 30 s, 4 ºC) and resuspended in 50 µL anti-His antibody (clone 4E3D10H2/E3) Alexa Fluor 647 conjugate (Thermo Fisher Scientific, Cat: MA1-135-A647; 50 µg/mL in PBSA). After incubating at 4 ºC for ≥30 min in the dark, cells were washed thrice with 1 mL cold PBSA before the fluorescence was analyzed on an LSR II flow cytometer (BD Biosciences). Maximum fluorescence and $K_{d,N}$ values were determined by minimizing the sum of squared errors.

Quantification of EpCAM Expression for Mammalian Cell Lines

Cells were grown to approximately 80% confluence and detached as described above. Cells were aliquoted at $1x10^6$ cells/sample, pelleted (8,000 g, 30 sec, 4 ºC), and washed with 1 mL ice cold PBSA. Cells were labeled with mouse anti-human EpCAM monoclonal antibody (clone 9C4) Alexa Fluor 647 conjugate (BioLegend, Cat: 324212) at 4 ºC for 30 min in the dark. Cells were then washed three times with 1 mL PBSA before immediate analysis on a BD LSR II. To quantify the absolute expression of EpCAM, the fluorescence was compared to a calibration curve prepared from anti-mouse IgG beads (Bangs Laboratories, Inc., Cat: 815). Polystyrene beads with known quantities of immobilized monoclonal anti-mouse IgG were labeled with the same anti-EpCAM Alexa Fluor 647 conjugate as the cells under the same conditions. Beads were washed once with PBSA and pelleted at 2,500g for 2.5 min. The beads were then washed thrice with 1 mL PBSA and analyzed on the flow cytometer in parallel with the cells. The standard curve generated from the bead populations was compared to the fluorescence of the mammalian cells that were labeled with the same mouse anti-EpCAM antibody and used to calculate the cellular EpCAM expression.

Copper Chelation and Purification of ^{64}Cu-Labeled CSANs

$^{64}CuCl_2$ (University of Wisconsin, Madison) was diluted with 100 µL of 100 µM sodium acetate buffer, pH 7.0 and pH adjusted using 1M HCl/NaOH. Approximately 7.9 mCi of the ^{64}Cu solution was added to 40 µL of DOTA-bisMTX (2 mM) in DMSO and the solution was incubated at 50 ºC for 30 min. After cooling to room temperature, the chelated DOTA-bisMTX was combined with the desired mixture of $DHFR^2$-Fn3 monomers at a 3:1 molar ratio in PBS, and the resulting solutions were incubated at room temperature for 30 min to allow for CSAN oligomerization. The ^{64}Cu-labeled

CSANs were then purified using a PD-10 column equilibrated PBS, pH 7.4, to remove excess DOTA-bisMTX and unchelated ^{64}Cu.

Tumor Inoculation

All procedures performed in studies involving animals were in accordance with the ethical standards of the University of Minnesota and approved by the Institutional Animal Care and Use Committee (IACUC). Four-week-old, male, athymic nude (NU/J) mice (Jackson Laboratory) were anesthetized with isofluorane (induced at 5% and maintained at 2% in 1 mL/min O_2) and inoculated with $2.5x10^6$ $EpCAM^{High}$ MCF-7 cells on the left shoulder and $2.5x10^6$ $EpCAM^{Low}$ MDA-MB-231 cells on the right shoulder, each as a 50% v/v suspension in Matrigel Matrix (Corning, Cat: 354248). Xenografts were allowed to grow for two weeks, yielding tumors of 8-12 mm in diameter. To support MCF-7 cell growth, the mice's water supply was supplemented with 500 μM 17-β-estradiol valerate.

Biodistribution Analysis

All procedures performed in studies involving animals were in accordance with the ethical standards of the University of Minnesota and approved by the Institutional Animal Care and Use Committee (IACUC). Mice were anesthetized with isofluorane (induced at 5% and maintained at 2% in 1 mL/min O_2) and tail vein injected with approximately 70-100 μCi of ^{64}Cu-labeled CSANs, as measured by an Atomlab 100 Dosimeter with a setting of 50.2. After 18 h, mice were euthanized via gentle CO_2 asphyxiation. Blood, bone, brain, heart, intestine, kidneys, liver, lungs, muscle, pancreas, skin, spleen, stomach, tail and tumors were resected, weighed, and had their radioactivity measured by a Hidex Automated Gamma Counter (Hidex) with counts averaged over 60 sec.

Statistical Considerations

Unless otherwise stated, experiments were performed in triplicate and data is presented as the mean ± standard deviation of three independent trials. Differences between means are compared using a two-tailed Student's t-test or a one-way analysis of variance (ANOVA), as appropriate. A p-value <0.05 is deemed to be statistically significant, and is denoted in graphics with an (*), $p<0.01$ is denoted with (**), and $p<0.001$ is denoted with (***).

ACKNOWLDEGEMENTS

This work was supported by the National Institutes of Health (NIH) R21 CA185627 (CRW), F30 CA210345 (CMC), T32 GM008244 (CMC), and the University of Minnesota, including an endowed fellowship on behalf of Dr. and Mrs. Bighley (CMC). Flow cytometry work was performed in the University Flow Cytometry Resource core facility at the University of Minnesota. The biodistribution work was performed in the University Imaging Center at the University of Minnesota.

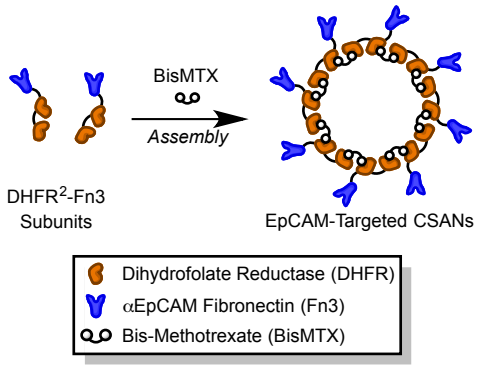

Figure 1. Chemically Self-Assembled Nanorings (CSANs). Bivalent $DHFR^2$ proteins fused to a targeting domain are spontaneously oligomerized into CSANs via the chemical dimerizer, bisMTX. In this work, a fibronectin domain with engineered specificity for epithelial cell adhesion molecule (EpCAM)[102] was fused, enabling the formation of EpCAM-targeted CSANs.

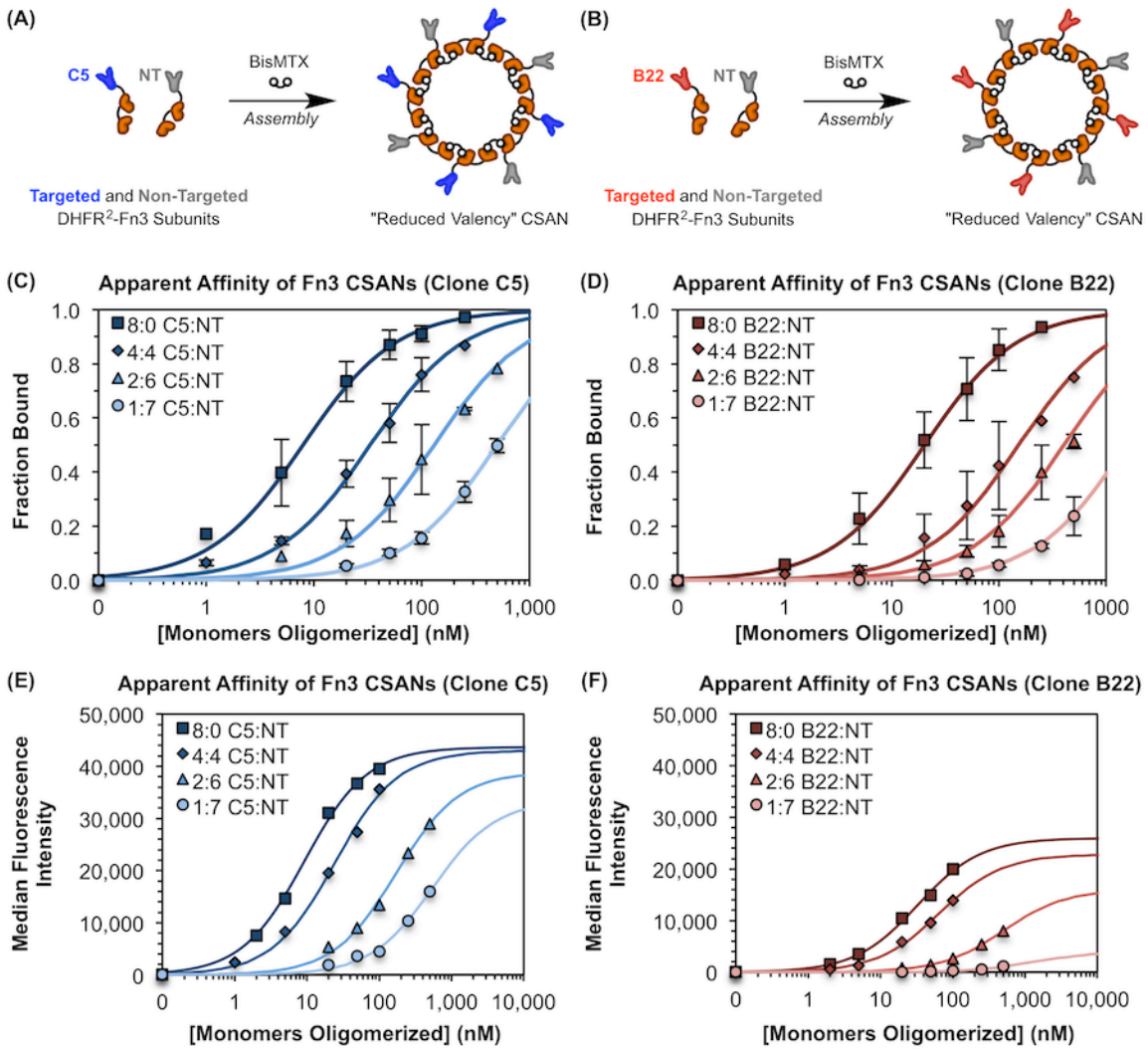

Figure 2. Modular Assembly of CSANs Enables Affinity Tuning. (A-B) CSANs with a reduced valency of EpCAM-binding Fn3 domains can be formed by co-assembling defined ratios of targeted and non-targeted DHFR^2-Fn3 fusion proteins using the chemical dimerizer, bisMTX. This was done for both the “high-affinity” Fn3 clone C5 and the “low-affinity” Fn3 clone B22. (C&D) CSANs of distinct average valencies were titrated against MCF-7 cells via flow cytometry to determine their apparent affinity for cellular EpCAM, as previously described.[29, 102] The apparent affinity of both scaffolds, (C) C5-targeted CSANs and (D) B22-targeted CSANs, varied directly with the proportion of binding domains in the CSAN. The legends give the ratio of targeted to non-targeted (T:NT) subunits incorporated into each CSAN. The x-axis provides the total

concentration of $DHFR^2$-Fn3 monomers that were oligomerized into CSANs using bisMTX. Each sample is normalized to the fitted maximum fluorescence intensity for that sample, enabling determination of the fraction of bound ligand at each concentration and facilitating the direct comparison of replicate titrations. Each titration was performed at least three independent times, and data is presented as the mean ± standard deviation of these trials. (E-F) Un-normalized binding isotherms, where the median fluorescence intensity (MFI) values are directly plotted against the ligand concentration without any normalization to the theoretical maximum of the binding isotherm. For clarity, data from a single representative titration is shown for each sample.

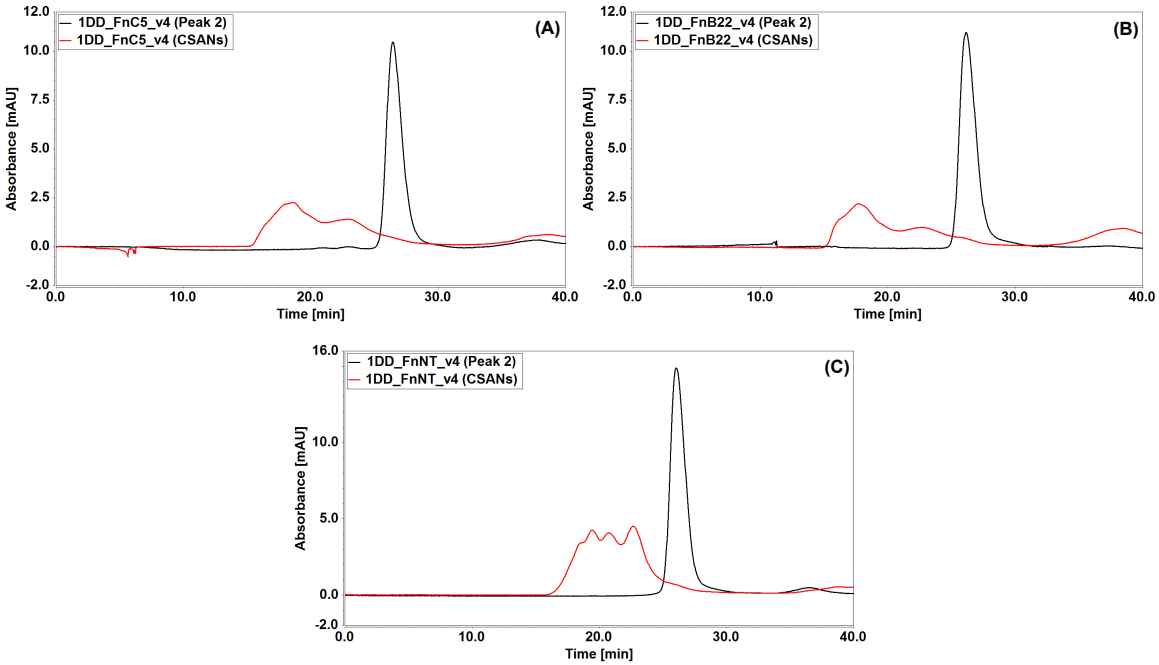

Figure 3. SEC Demonstrates Complete Oligomerization of DHFR^2-Fn3 Monomers into CSANs. Purified DHFR^2-Fn3 monomers were analyzed by SEC, as described above. For oligomerization, a 3-fold molar excess of bisMTX was added to a solution of monomeric protein and, after ≥30 min incubation at room temperature, analyzed via SEC in identical fashion. As shown, all three constructs (A) DHFR^2-Fn3 C5, (B) DHFR^2-Fn3 B22, and (C) DHFR^2-Fn3 NT all completely oligomerized into CSANs with no residual monomeric species detected. Previous cryo-EM analyses of these oligomerized species provided direct evidence of nanoring formation.[29, 166]

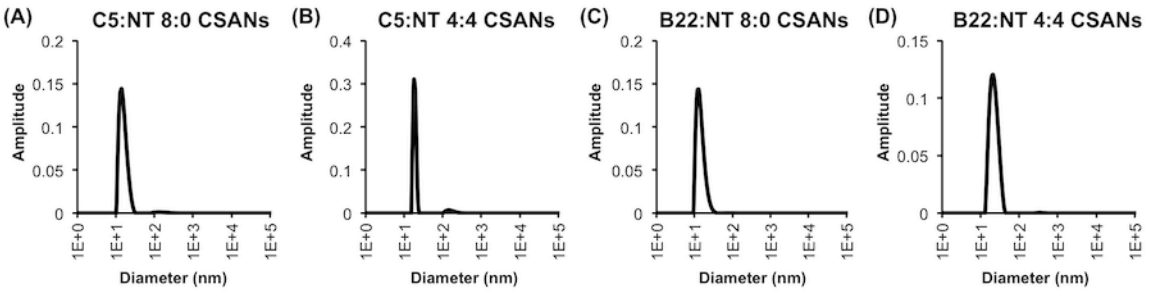

Entry	Targeting Ligand	T:NT Ratio	Hydrodynamic Diameter (nm)	Dispersity
(A)	C5	8:0	17 ± 6.8	40%
(B)	C5	4:4	19 ± 4.9	26%
(C)	B22	8:0	18 ± 6.6	38%
(D)	B22	4:4	19 ± 14	72%

Figure 4. DLS Characterization of Key CSAN Species. For analysis, 60 µL of CSANs in PBS was loaded into a cuvette and analyzed on a Punk DLS unit (Unchained Labs). Hydrodynamic diameter values represent the mean ± standard deviation of at least three measurements. These results compare favorably with our previously-reported DLS analysis of other Fn3-targeted CSANs.[29]

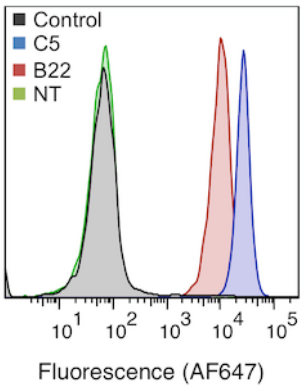

Figure 5. Selectivity of Fibronectin Functionalized CSANs. Separately, the $DHFR^2$-C5, $DHFR^2$-B22, and $DHFR^2$-NT subunits were oligomerized into CSANs and assessed to their binding to EpCAM-positive cells via flow cytometry, as described above. Briefly, $5x10^4$ EpCAM-expressing MCF-7 cells were washed with PBSA and labeled with 100 nM CSANs for 90 min at 4 ºC. Cells were then pelleted (8,000 g, 30 s, 4 ºC) and resuspended in 50 µL anti-His antibody (clone 4E3D10H2/E3) Alexa Fluor 647 conjugate (50 µg/mL in PBSA). After incubating at 4 ºC for ≥30 min in the dark, cells were washed thrice with 1 mL cold PBSA before the fluorescence was analyzed on an LSR II flow cytometer (BD Biosciences). As shown, the EpCAM targeted CSANs utilizing either Fn3 clone C5 (blue) or clone B22 (red) exhibit robust binding to the MCF-7 cells, with fluorescent signals directly proportional to their respective apparent affinities. In contrast, the CSANs displaying the non-targeted Fn3 clone NT (green) produce no appreciable fluorescent signal compared to the secondary-only control (black), indicative of a lack of binding.

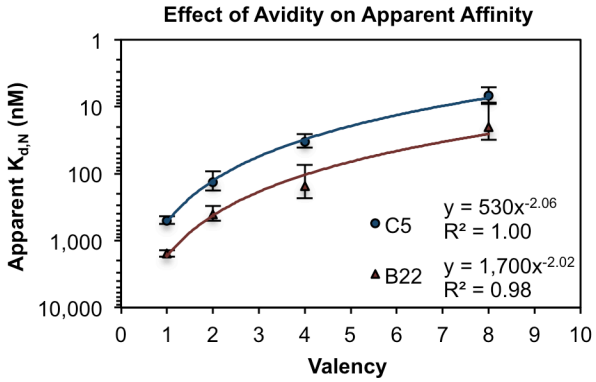

Figure 6. Apparent Affinity Varies with Binding Domain Valency. CSANs composed of different valencies of EpCAM-binding Fn3 domains (either clone C5 or B22) were titrated against EpCAM-expressing MCF-7 cells via flow cytometry. The resulting $K_{d,N}$ values were plotted against the valency of the binding domains, and the correlation was fit to a power regression curve, as this model provided the best coefficient of determination (R^2 value) for both Fn3 clones. Each titration was performed at least three times, and data is presented as the mean ± standard deviation of the $K_{d,N}$ values resulting from these independent trials. Apparent dissociation constants are given in **Table 1**.

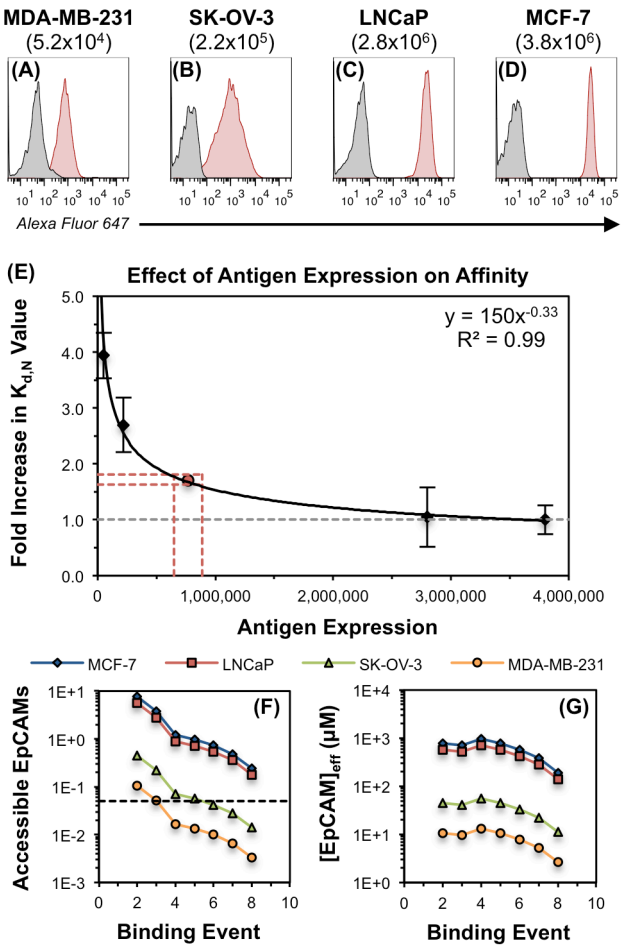

Figure 7. Apparent Affinity Varies with Antigen Expression Density. (A-D) The absolute EpCAM expression of four cell lines was quantitated via flow cytometry by comparing the mean fluorescence intensity of the cellular samples to those of standard calibration beads. (E) To isolate the effect of EpCAM expression density on the apparent affinity of the CSAN scaffold, fully-targeted CSANs utilizing clone C5 (8:0 C5:NT) were titrated against the same four EpCAM-expressing cell lines shown in panels A-D. The minimum apparent $K_{d,N}$ value (6.9 ± 1.8 nM) was obtained when the CSANs were bound to the MCF-7 cells; therefore, this value was chosen as the baseline (i.e., value of 1.0) and is represented by the dashed grey line. The apparent $K_{d,N}$ values obtained for the LNCaP (7.2 ± 3.7 nM), SK-OV-3 (19 ± 3.4 nM), and MDA-MB-231 (27 ± 2.8 nM) were scaled relative to the MCF-7 $K_{d,N}$ value to provide the fold by which the apparent $K_{d,N}$

had been increased. This “fold increase in $K_{d,N}$ value” is plotted against the quantitated number of EpCAMs/cell, providing a local fit within the confines of this data set. The relationship was fit to a power regression curve, as this model provided the best coefficient of determination (R^2 value). Each titration was performed at least three times, and data is presented as the mean ± standard deviation of the fold increase in the apparent $K_{d,N}$ values resulting from these independent trials. The red lines and dot indicate the threshold number of EpCAMs/cell needed to permit theoretical octavalent CSAN binding to the cells, per the model proposed above. (F) The theoretical number of EpCAMs accessible to the CSAN at each of the eight binding events. The black dashed line indicates the threshold number of accessible EpCAMs needed to permit octavalent CSAN binding to the cells. (G) The theoretical effective molarity of EpCAMs accessible to the CSAN at each of the eight binding events. See **Figure 8** for additional details regarding the model used to produce panels (F-G) and the associated threshold values.

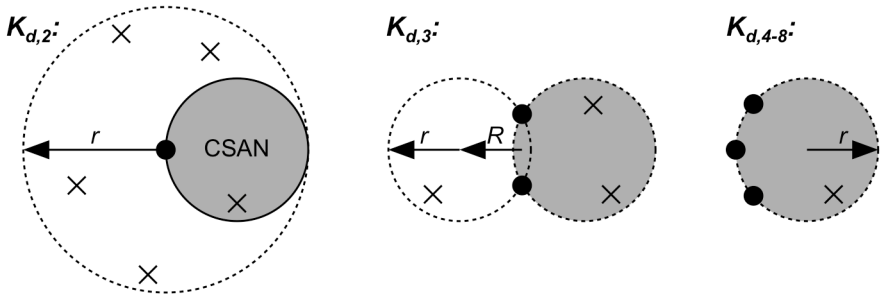

Figure 8. Model of Antigen Accessibility. The number of antigens (i.e., EpCAMs) accessible to the CSAN was modeled for each possible binding event (up to eight for the fully octavalent CSANs). Considering the second binding event ($K_{d,2}$), once the CSAN (grey circle) binds to the first EpCAM (black dot), it can rotate about that binding interaction and access the circular area indicated by the dashed line. The area of this circle can be calculated from the known diameter of the CSAN (~$20x10^{-9}$ m).[29, 166] Assuming an average diameter of $14x10^{-6}$ m for mammalian cells in suspension[174], the number of EpCAMs (cross marks) present in this area can be calculated using the experimental number of EpCAMs/cell (**Figure 7A-D**). Provided that the CSAN can access the hemispheric volume above this cell surface area, the effective molarity of EpCAMs in this region can be determined. A similar analysis can be performed for the third binding event ($K_{d,3}$); now that the CSAN is tethered by two ligand/receptor interactions, it is less free to rotate. Making the most generous assumuption about the conformational flexibility of this arrangement, the CSAN can now occupy the area indicated by the partially overlapping circles; likewise, it can access the volume of the corresponding half spindle torus. For the subsequent binding events ($K_{d,4-8}$), the CSAN is very likely anchored in its orientation, and the remaining ligands bind to any accessible EpCAMs in the circular area (smaller hemispheric volume). The calculated EpCAM numbers and effective molarities are presented in **Figure 7F-G**.

Assumptions and Approximations. This model makes a number of additional assumptions, including: (1) the radius of the cell is much greater than the radius of the CSAN, such that the surface of the cell is approximated as a planar surface with respect to the CSAN; (2) EpCAM moieties are homogenously distributed across the surface of the cell; (3) the CSAN scaffold itself occupies no space; (4) the linkers that tether the binding domains to the CSAN are sufficiently long and flexible such that the conformational flexibility of the Fn3s is essentially infinite and they can sample the area of the CSAN itself (as opposed to a defined area along the periphery), and (5) each ligand has an equal probability of binding to a cell surface antigen. While these assumptions may or may not be valid, we note that the model derived under these constraints does offer reasonable correlation to the experimental results.

Estimation of Antigen Thresholds. We sought to estimate the minimum EpCAM density required to enable fully octavalent binding of a CSAN to a cell membrane. Using ***equation 1***, the observed $K_{d,N}$ values for fully-targeted (i.e., 8:0 C5:NT) CSANs against the MCF-7 (6.9 ± 1.8 nM), LnCAP (7.2 ± 3.7 nM), SK-OV-3 (19 ± 3.4 nM), and MDA-MB-231 (27 ± 2.8 nM) cells (**Figure 7E**) were converted to estimated binding valencies of *N* = 8, 8, 5, and 4, respectively. This suggested that the CSANs could bind octavalently to the MCF-7 and LNCaP cells, but only pentavalently to the SK-OV-3 cells and tetravalently to the MDA-MB-231 cells. Per **Figure 7F** and the model of EpCAM accessibility discussed above, this pattern of binding is most consistent with a treshold number of accessible antigens between 0.042 – 0.057 EpCAMs, as this “cut off” permits eight binding events for the MCF-7 and LNCaP cells but only five and three for the SK-OV-3 and MDA-MB-231 cells, respectively. Essentially, the threshold may fall anywhere between the fourth and fifth point on the SK-OV-3 curve (green) in **Figure 7F**, which have the respective calculated values of 0.042 and 0.057 EpCAMs. Thus, we estimate

the threshold as the midpoint of this range, 0.049 accessible EpCAMs, and represent that value by the horizontal black dashed line in **Figure 7F**. These numbers of accessible EpCAMs (**Figure 7F**) were calculated using the general equation:

$$(\textbf{Eq. S1})\ R_A = \frac{R}{4\pi r_{cell}^2} \cdot A_L$$

Where R_A is the number of accessible receptors (in this case, EpCAM), R is the number of receptors/cell, r_{cell} is the radius of the cell, and A_L is the area accesible to the ligand (in this case, the CSAN). Note that (1) the A_L term will vary according to the model discussed above, and (2) division of R_A by the volume accessible to the ligand provides the effective concentration of receptors (i.e., $[EpCAM]_{eff}$ in **Figure 7G**).

Using the form of A_L for the eighth binding event ($K_{d,8}$) and rearranging ***equation S1*** enabled conversion of the accessible EpCAM thresholds (R_A = 0.042 – 0.057) to EpCAM/cell values of R = 6.5 – 8.9x10^5 EpCAMs/cell. Via the relationship elucidated in **Figure 7E**, this indicates a 1.6 – 1.8 fold (39 – 45%) reduction in $K_{d,N}$. The midpoint of this threshold region is depicted as the red point in **Figure 7E**, with the upper and lower bounds represented by the projected red dashed lines. A summary of estimated threshold bounds are provided in the table below:

	Accessible EpCAMs	$[EpCAM]_{eff}$ (μM)	EpCAMs/Cell	Fold $K_{d,N}$ Reduction	% $K_{d,N}$ Reduction	Representation in Figure 4E
Upper Estimate	0.057	45	8.9x10^5	1.6	39%	Dashed red lines
Median Estimate	0.049	39	7.7x10^5	1.7	42%	Solid red point
Lower Estimate	0.042	33	6.5x10^5	1.8	45%	Dashed red lines

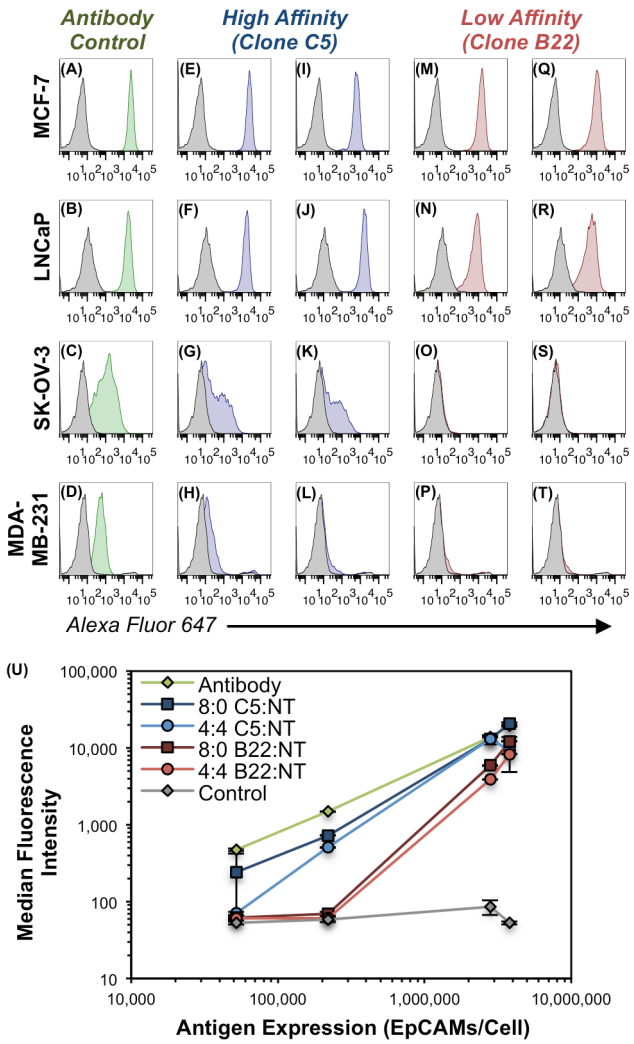

Figure 9. Avidity Modulation Enables Cellular Discrimination *In Vitro*. Flow cytometry histogram plots depicting the binding of various constructs to EpCAM-expressing cell lines. (A-D) Qualitative EpCAM expression of indicated cell lines using a commercially-available antibody-fluorophore conjugate. The same cells were labeled with Fn3-targeted CSANs (50 nM) composed of T:NT ratios of (E-H) 8:0 C5:NT, (I-L) 4:4 C5:NT, (M-P) 8:0 B22:NT, or (Q-T) 4:4 B22:NT. In all panels, the background fluorescence of the negative control sample is shown by the gray histograms, (A-D) binding of the positive-control antibody is shown by the green histograms, (E-L) binding of CSANs utilizing clone C5 is shown by the blue histograms, and (M-T) binding of Fn3 CSANs utilizing clone B22 is shown by the red histograms. Triplicate experiments were

performed as described in the methods, and the histogram plots for one representative trial are shown. Histograms for the full-range of CSAN concentrations tested (i.e., 5, 50, and 500 nM) are shown in **Figure 10**. (U) Quantitative depiction of avidity-modulated CSANs (50 nM) binding to EpCAM+ cells, as in panels A-T. Median fluorescence intensity values are plotted against the EpCAM expression of each of the four cell lines. Data is presented as the mean ± standard deviation of three independent trials.

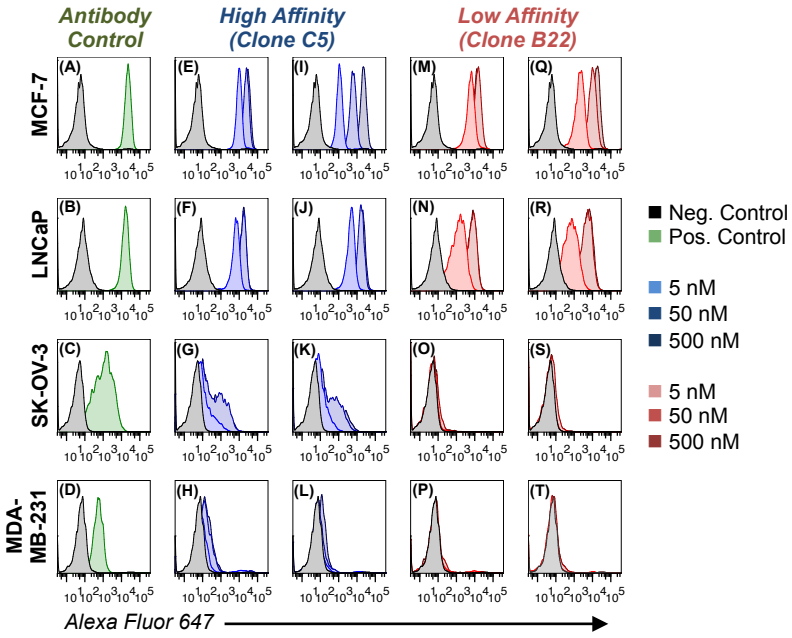

Figure 10. Target Discrimination Across a Range of Ligand Concentrations. Companion data for **Figure 9**, where the flow cytometry histogram plots depict CSAN binding capability across a 2-log range of concentrations (i.e., 5, 50, and 500 nM).

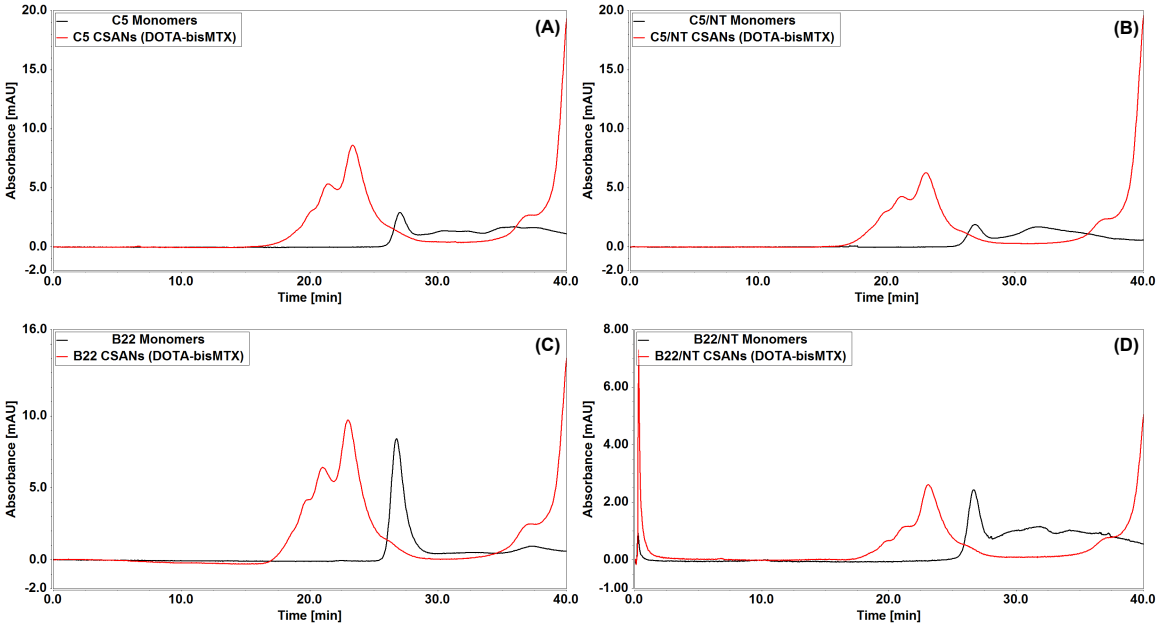

Figure 11. Oligomerization of DHFR^2-Fn3 Monomers into CSANs using DOTA-bisMTX. Purified DHFR^2-Fn3 monomers were analyzed by SEC, as described above. For oligomerization, a 3-fold molar excess of DOTA-bisMTX was added to a solution of monomeric protein and, after ≥30 min incubation at room temperature, analyzed via SEC in identical fashion. As shown, all constructs (A) DHFR^2-Fn3 C5, (B) a 1:1 mixture of DHFR^2-Fn3 C5 and DHFR^2-Fn3 NT, (C) DHFR^2-Fn3 B22, and (D) a 1:1 mixture of DHFR^2-Fn3 B22 and DHFR^2-Fn3 NT all completely oligomerized into CSANs with no residual monomeric species detected.

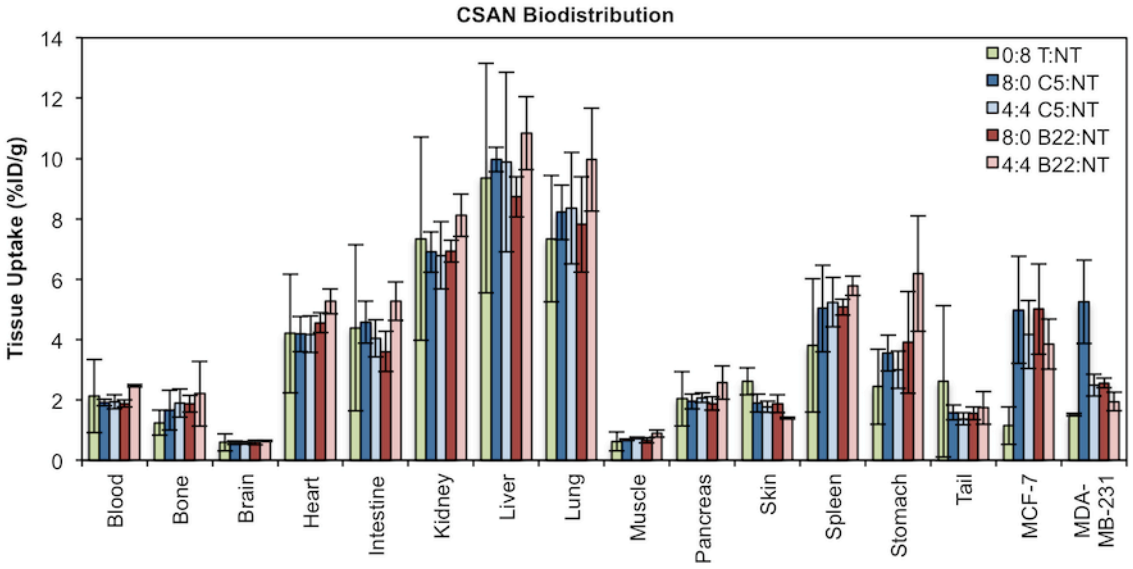

Figure 12. Biodistribution of Avidity-Modulated CSANs. Eighteen hours after the IV infusion of avidity-modulated CSANs, mice were euthanized and tissues were resected, weighed, and measured for activity. Activity values were time-corrected to 18 h to account for continued decay during the weighing/counting process. Data is presented as the mean ± standard deviation of the mice (n = 3) in each treatment group.

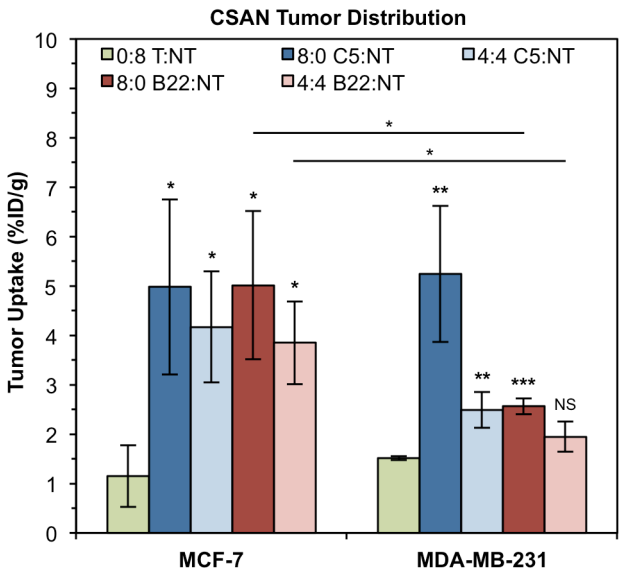

Figure 13. Xenograft Tumor Distribution of Avidity-Modulated CSANs. EpCAM^{High} MCF-7 and EpCAM^{Low} MDA-MB-231 xenograft tumors were resected, weighed, and counted for activity 18 h after IV infusion of avidity modulated CSANs. Activity values were time-corrected to 18 h to account for continued decay during the weighing/counting process. Data is presented as the mean ± standard deviation of the mice (n = 3) in each treatment group. Unless specified otherwise, statistical relevance marks comparison of the indicated sample to the 0:8 T:NT sample for that tumor, as determined by a two-tailed Student's t-test. For clarity, intertumoral comparisons that failed to reach statistical significance are not marked.

Clone	Valency (N)	$K_{d,N}$ (nM)	α	$1/\beta$
C5	1	500 ± 60	1.0	1.0
	2	140 ± 40	2.9×10^{-1}	3.7
	4	33 ± 8	2.9×10^{-2}	15
	8	6.9 ± 1.8	3.0×10^{-4}	72
B22	1	1,600 ± 200	1.0	1.0
	2	400 ± 100	2.6×10^{-1}	3.9
	4	150 ± 80	2.1×10^{-2}	10
	8	20 ± 11	1.2×10^{-4}	78

Table 1. Apparent Affinity, Cooperativity, and Enhancement Parameters of Multivalent CSANs. Apparent $K_{d,N}$ values (nM) for the data presented in **Figure 6** are provided. Each titration was performed at least three times, and data is presented as the mean ± standard deviation of the $K_{d,N}$ values resulting from these independent trials. The cooperativity (α) of the CSANs was calculated using ***equation 2***; values <1 indicate the CSANs are negatively-cooperative. Enhancement factors (β) were calculated using ***equation 3***; values are presented as $1/\beta$ to enable direct interpretation as the fold improvement in the multivalent $K_{d,N}$ value over that of the singly-targeted $K_{d,1}$ value.

#	Valency	Fn3 Clone	Target Cell	Predicted $K_{d,N}$ (nM)	Experimental $K_{d,N}$ (nM)
1	4	C5	MDA-MB-231	125	150
2	4	C5	LNCaP	32	34
3	4	B22	LNCaP	103	74
4	8	B22	LNCaP	26	21

Table 2. Comparison of Predicted and Experimental Dissociation Constants. The accuracy of ***equation 2*** was tested by comparing predicted $K_{d,N}$ values to experimentally determined values. Notably, these experimental values were not used to create ***equation 2*** and thus comprise a unique set of conditions suitable for testing the equation's predictive capacity. Affinity titrations were performed once and are presented as estimated values without error.

CHAPTER V

Conclusions and Future Prospects

This thesis broadly describes the development of a diverse toolkit suitable for the study of interactions between binding ligands and cell membrane antigens. While this work focuses on epithelial cell adhesion molecule (EpCAM) as a model antigen, the principles elucidated herein are directly applicable to the molecular recognition of other membrane-anchored proteins, especially those that are slowly- or non-internalizing. Likewise, the use of chemically self-assembled nanorings (CSANs) as a prototypical scaffold has yielded concrete design implications that may prove useful for the engineering of other multivalent targeting scaffolds. Emphasis is placed on using these tools to direct specific and reversible interactions between cells.

In *Chapter I*, we review the current landscape of non-genetic approaches to cell membrane engineering. While genetically-encoded artificial receptors have proven clinically efficacious, inherent limitations in the creation of these modified cells have thus far restricted the scope of this technology. Accordingly, a number of alternative methods have emerged in an effort to expand the use of membrane-engineered cells, particularly in the context of directing cell-cell interactions. The introductory chapter highlights these techniques – namely, hydrophobic membrane insertion, chemical modification, liposome fusion, metabolic engineering, and enzymatic remodeling – and summarizes their major applications. Based on this analysis, perspective is provided on the ideal features of these systems with an emphasis on the potential for clinical translation. We conclude that future work in this arena should focus on the development of approaches that are rapid, stable, universal, innocuous, and reversible.

Chapter II details the development of the first ligands based upon the human tenth type III fibronectin domain (Fn3) that bind to the carcinoma and cancer stem cell marker, EpCAM. This was accomplished by sorting a meticulously designed library of Fn3 clones

displayed on the surface of yeast against EpCAM in a variety of contexts, including recombinant antigen adhered to magnetic beads and cellular antigen natively expressed on mammalian cell monolayers. Instrumental in this work was our collaborators' development of a novel approach for isolating high-affinity ligands from the cell panning selections. These EpCAM-binding Fn3s were further engineered to include a single cysteine mutation that was found suitable for the site-specific conjugation of a variety of chemical matter without detrimental effects to the biophysical properties of the protein. Future work in this area should be focused on the continued development of these soluble ligands for several applications, especially imaging agents for the detection and staging of epithelial malignancies. Furthermore, effort should be undertaken to map the specific epitope to which these ligands bind, perhaps through crystallography or high-throughput methods for screening competition with known monoclonal antibodies.

These anti-EpCAM Fn3 domains were subsequently incorporated into CSANs for use as a cell-directing protein scaffold, as described in *Chapter III*. To install the CSAN on a cell surface, phospholipids conjugated to either biotin or dibenzocyclooctyne (DBCO) were hydrophobically inserted into the membrane. Heterobifunctional CSANs displaying the Fn3's and either monovalent streptavidin (mSA) domains or free azide groups were then bound to the biotin or DBCO moieties, respectively, and remained stably present on the cell surface for ≥72 h *in vitro*. These CSAN-labeled cells were capable of recognizing EpCAM-expressing target cells, forming intercellular interactions that were subsequently reversed by disassembling the nanoring with the FDA-approved antibiotic, trimethoprim. This work demonstrated the use of this system to engineer cell surfaces with prosthetic receptors capable of directing specific and reversible cell-cell interactions. Moving forward, this system should be optimized for the formation of stable interactions between multiple distinct cell types, thus enabling *in vitro* tissue engineering. Furthermore, the

rapid and non-genetic nature of the membrane modification opens the door to the functionalization of certain stem cell populations, particularly mesenchymal stem cells (MSCs). This could be useful for tissue regeneration applications, especially myocardial repair following acute ischemia.

Finally, *Chapter IV* takes advantage of the modularity of the CSAN to quantitatively probe the importance of binding affinity, ligand valency, and antigen expression density on cellular recognition. We found that the apparent affinity of the CSAN as a whole predictably varies as a function of these variables, and these lessons were applied to the development of scaffolds that could selectively bind only to cells that grossly over-express EpCAM. This potential for cell selectivity was then demonstrated *in vivo* using murine xenografts of EpCAM-positive breast cancer cell lines. This work demonstrates that avidity optimization is a viable strategy for designing discriminatory targeting scaffolds. Because many current immunotherapies exhibit “on-target, off-tumor” toxicities that result from the recognition of healthy tissue expressing low, physiologic levels of the cognate antigen, these results may inform the development of next-generation therapies with greater therapeutic windows. Furthermore, avidity optimization may permit the clinical targeting of solid tumor antigens previously thought to be too toxic for therapeutic intervention, thereby resurrecting these otherwise promising markers.

Collectively, this work makes significant strides in the disciplines of protein and cell membrane engineering, with future applications ranging from foundational basic science to translational medicine, including diagnostic imaging, tissue engineering, regenerative medicine, and cancer immunotherapy.

BIBLIOGRAPHY

1. Barbash, I. M.; Chouraqui, P.; Baron, J.; Feinberg, M. S.; Etzion, S.; Tessone, A.; Miller, L.; Guetta, E.; Zipori, D.; Kedes, L. H.; Kloner, R. A.; Leor, J., Systemic delivery of bone marrow-derived mesenchymal stem cells to the infarcted myocardium: feasibility, cell migration, and body distribution. *Circulation* **2003,** *108* (7), 863-8.
2. Cheng, Z.; Ou, L.; Zhou, X.; Li, F.; Jia, X.; Zhang, Y.; Liu, X.; Li, Y.; Ward, C. A.; Melo, L. G.; Kong, D., Targeted migration of mesenchymal stem cells modified with CXCR4 gene to infarcted myocardium improves cardiac performance. *Mol Ther* **2008,** *16* (3), 571-9.
3. Kuehn, B. M., The Promise and Challenges of CAR-T Gene Therapy. In *Jama*, United States, 2017; Vol. 318, pp 2167-2169.
4. Sadelain, M.; Rivière, I.; Riddell, S., Therapeutic T cell engineering. *Nature* **2017,** *545* (7655), 423-431.
5. Curran, K. J.; Pegram, H. J.; Brentjens, R. J., Chimeric antigen receptors for T cell immunotherapy: current understanding and future directions. *J Gene Med* **2012,** *14* (6), 405-15.
6. Bonifant, C. L.; Jackson, H. J.; Brentjens, R. J.; Curran, K. J., Toxicity and management in CAR T-cell therapy. *Mol Ther Oncolytics* **2016,** *3*, 16011.
7. Huehls, A. M.; Coupet, T. A.; Sentman, C. L., Bispecific T-cell engagers for cancer immunotherapy. *Immunology And Cell Biology* **2014,** *93*, 290.
8. Mullard, A., FDA approves first bispecific. *Nature Reviews Drug Discovery* **2014,** *14*, 7.
9. Garber, K., Bispecific antibodies rise again. *Nat Rev Drug Discov* **2014,** *13* (11), 799-801.

10. White, S. H.; von Heijne, G., Transmembrane helices before, during, and after insertion. *Curr Opin Struct Biol* **2005,** *15* (4), 378-86.

11. Simons, K.; Sampaio, J. L., Membrane organization and lipid rafts. *Cold Spring Harb Perspect Biol* **2011,** *3* (10), a004697.

12. Jeong, J. H.; Schmidt, J. J.; Kohman, R. E.; Zill, A. T.; DeVolder, R. J.; Smith, C. E.; Lai, M. H.; Shkumatov, A.; Jensen, T. W.; Schook, L. G.; Zimmerman, S. C.; Kong, H., Leukocyte-mimicking stem cell delivery via in situ coating of cells with a bioactive hyperbranched polyglycerol. *J Am Chem Soc* **2013,** *135* (24), 8770-3.

13. Fernandez-Vidal, M.; White, S. H.; Ladokhin, A. S., Membrane partitioning: "classical" and "nonclassical" hydrophobic effects. *J Membr Biol* **2011,** *239* (1-2), 5-14.

14. Gorfe, A. A.; Baron, R.; McCammon, J. A., Water-membrane partition thermodynamics of an amphiphilic lipopeptide: an enthalpy-driven hydrophobic effect. *Biophys J* **2008,** *95* (7), 3269-77.

15. Kean, T. J.; Duesler, L.; Young, R. G.; Dadabayev, A.; Olenyik, A.; Penn, M.; Wagner, J.; Fink, D. J.; Caplan, A. I.; Dennis, J. E., Development of a peptide-targeted, myocardial ischemia-homing, mesenchymal stem cell. *J Drug Target* **2012,** *20* (1), 23-32.

16. Hamdy, N.; Goustin, A. S.; Desaulniers, J. P.; Li, M.; Chow, C. S.; Al-Katib, A., Sheep red blood cells armed with anti-CD20 single-chain variable fragments (scFvs) fused to a glycosylphosphatidylinositol (GPI) anchor: a strategy to target CD20-positive tumor cells. *J Immunol Methods* **2005,** *297* (1-2), 109-24.

17. Ko, I. K.; Kean, T. J.; Dennis, J. E., Targeting mesenchymal stem cells to activated endothelial cells. *Biomaterials* **2009,** *30* (22), 3702-10.

18. Won, Y. W.; Patel, A. N.; Bull, D. A., Cell surface engineering to enhance mesenchymal stem cell migration toward an SDF-1 gradient. *Biomaterials* **2014,** *35* (21), 5627-35.

19. Lu, L.; Gao, J.; Guo, Z., Labeling Cell Surface GPIs and GPI-Anchored Proteins through Metabolic Engineering with Artificial Inositol Derivatives. *Angew Chem Int Ed Engl* **2015,** *54* (33), 9679-82.

20. de Kruif, J.; Tijmensen, M.; Goldsein, J.; Logtenberg, T., Recombinant lipid-tagged antibody fragments as functional cell-surface receptors. *Nat Med* **2000,** *6* (2), 223-7.

21. Altman, M. O.; Chang, Y. M.; Xiong, X.; Tan, W., Modifying cellular properties using artificial aptamer-lipid receptors. *Sci Rep* **2013,** *3*, 3343.

22. Xiong, X.; Liu, H.; Zhao, Z.; Altman, M. B.; Lopez-Colon, D.; Yang, C. J.; Chang, L.-J.; Liu, C.; Tan, W., DNA Aptamer-Mediated Cell Targeting. *Angewandte Chemie International Edition* **2013,** *52* (5), 1472-1476.

23. Lim, K. S.; Lee, D. Y.; Valencia, G. M.; Won, Y. W.; Bull, D. A., Cell surface-engineering to embed targeting ligands or tracking agents on the cell membrane. *Biochem Biophys Res Commun* **2017,** *482* (4), 1042-1047.

24. Kim, S. A.; Peacock, J. S., The use of palmitate-conjugated protein A for coating cells with artificial receptors which facilitate intercellular interactions. *J Immunol Methods* **1993,** *158* (1), 57-65.

25. Lo, C. Y.; Antonopoulos, A.; Dell, A.; Haslam, S. M.; Lee, T.; Neelamegham, S., The use of surface immobilization of P-selectin glycoprotein ligand-1 on mesenchymal stem cells to facilitate selectin mediated cell tethering and rolling. *Biomaterials* **2013,** *34* (33), 8213-22.

26. Todhunter, M. E.; Jee, N. Y.; Hughes, A. J.; Coyle, M. C.; Cerchiari, A.; Farlow, J.; Garbe, J. C.; LaBarge, M. A.; Desai, T. A.; Gartner, Z. J.,

Programmed synthesis of three-dimensional tissues. *Nat Methods* **2015,** *12* (10), 975-81.

27. Selden, N. S.; Todhunter, M. E.; Jee, N. Y.; Liu, J. S.; Broaders, K. E.; Gartner, Z. J., Chemically programmed cell adhesion with membrane-anchored oligonucleotides. *J Am Chem Soc* **2012,** *134* (2), 765-8.
28. Gabrielse, K.; Gangar, A.; Kumar, N.; Lee, J. C.; Fegan, A.; Shen, J. J.; Li, Q.; Vallera, D.; Wagner, C. R., Reversible re-programing of cell-cell interactions. *Angew Chem Int Ed Engl* **2014,** *53* (20), 5112-6.
29. Csizmar, C. M.; Petersburg, J. R.; Hendricks, A.; Stern, L. A.; Hackel, B. J.; Wagner, C. R., Engineering Reversible Cell-Cell Interactions with Lipid Anchored Prosthetic Receptors. *Bioconjug Chem* **2018,** *29* (4), 1291-1301.
30. Takeo, M.; Li, C.; Matsuda, M.; Nagai, H.; Hatanaka, W.; Yamamoto, T.; Kishimura, A.; Mori, T.; Katayama, Y., Optimum design of amphiphilic polymers bearing hydrophobic groups for both cell surface ligand presentation and intercellular cross-linking. *J Biomater Sci Polym Ed* **2015,** *26* (6), 353-68.
31. Zhao, W.; Loh, W.; Droujinine, I. A.; Teo, W.; Kumar, N.; Schafer, S.; Cui, C. H.; Zhang, L.; Sarkar, D.; Karnik, R.; Karp, J. M., Mimicking the inflammatory cell adhesion cascade by nucleic acid aptamer programmed cell-cell interactions. *Faseb j* **2011,** *25* (9), 3045-56.
32. Sarkar, D.; Spencer, J. A.; Phillips, J. A.; Zhao, W.; Schafer, S.; Spelke, D. P.; Mortensen, L. J.; Ruiz, J. P.; Vemula, P. K.; Sridharan, R.; Kumar, S.; Karnik, R.; Lin, C. P.; Karp, J. M., Engineered cell homing. *Blood* **2011,** *118* (25), e184-91.
33. Koyfman, A. Y.; Braun, G. B.; Reich, N. O., Cell-targeted self-assembled DNA nanostructures. *J Am Chem Soc* **2009,** *131* (40), 14237-9.

34. Gong, P.; Zheng, W.; Huang, Z.; Zhang, W.; Xiao, D.; Jiang, X., A Strategy for the Construction of Controlled, Three-Dimensional, Multilayered, Tissue-Like Structures. *Advanced Functional Materials* **2013,** *23* (1), 42-46.

35. Cheng, H.; Byrska-Bishop, M.; Zhang, C. T.; Kastrup, C. J.; Hwang, N. S.; Tai, A. K.; Lee, W. W.; Xu, X.; Nahrendorf, M.; Langer, R.; Anderson, D. G., Stem cell membrane engineering for cell rolling using peptide conjugation and tuning of cell-selectin interaction kinetics. *Biomaterials* **2012,** *33* (20), 5004-12.

36. Chiarantini, L.; Droleskey, R.; Magnani, M.; DeLoach, J. R., In vitro targeting of erythrocytes to cytotoxic T-cells by coupling of Thy-1.2 monoclonal antibody. *Biotechnol Appl Biochem* **1992,** *15* (2), 171-84.

37. Amaral, A. J.; Pasparakis, G., Macromolecular cell surface engineering for accelerated and reversible cellular aggregation. *Chem Commun (Camb)* **2015,** *51* (99), 17556-9.

38. Sarkar, D.; Vemula, P. K.; Zhao, W.; Gupta, A.; Karnik, R.; Karp, J. M., Engineered mesenchymal stem cells with self-assembled vesicles for systemic cell targeting. *Biomaterials* **2010,** *31* (19), 5266-74.

39. Dutta, D.; Pulsipher, A.; Luo, W.; Mak, H.; Yousaf, M. N., Engineering cell surfaces via liposome fusion. *Bioconjug Chem* **2011,** *22* (12), 2423-33.

40. Dutta, D.; Pulsipher, A.; Luo, W.; Yousaf, M. N., Synthetic chemoselective rewiring of cell surfaces: generation of three-dimensional tissue structures. *J Am Chem Soc* **2011,** *133* (22), 8704-13.

41. O'Brien, P. J.; Luo, W.; Rogozhnikov, D.; Chen, J.; Yousaf, M. N., Spheroid and Tissue Assembly via Click Chemistry in Microfluidic Flow. *Bioconjug Chem* **2015,** *26* (9), 1939-49.

42. Rogozhnikov, D.; O'Brien, P. J.; Elahipanah, S.; Yousaf, M. N., Scaffold Free Bio-orthogonal Assembly of 3-Dimensional Cardiac Tissue via Cell Surface Engineering. *Sci Rep* **2016,** *6*, 39806.

43. Kayser, H.; Geilen, C. C.; Paul, C.; Zeitler, R.; Reutter, W., Incorporation of N-acyl-2-amino-2-deoxy-hexoses into glycosphingolipids of the pheochromocytoma cell line PC 12. *FEBS Lett* **1992,** *301* (2), 137-40.

44. Gartner, Z. J.; Bertozzi, C. R., Programmed assembly of 3-dimensional microtissues with defined cellular connectivity. *Proc Natl Acad Sci U S A* **2009,** *106* (12), 4606-10.

45. Shi, P.; Ju, E.; Yan, Z.; Gao, N.; Wang, J.; Hou, J.; Zhang, Y.; Ren, J.; Qu, X., Spatiotemporal control of cell-cell reversible interactions using molecular engineering. *Nat Commun* **2016,** *7*, 13088.

46. Sugimoto, S.; Moriyama, R.; Mori, T.; Iwasaki, Y., Surface engineering of macrophages with nucleic acid aptamers for the capture of circulating tumor cells. *Chem Commun (Camb)* **2015,** *51* (98), 17428-30.

47. Capicciotti, C. J.; Zong, C.; Sheikh, M. O.; Sun, T.; Wells, L.; Boons, G.-J., Cell-Surface Glyco-Engineering by Exogenous Enzymatic Transfer Using a Bifunctional CMP-Neu5Ac Derivative. *Journal of the American Chemical Society* **2017,** *139* (38), 13342-13348.

48. Swee, L. K.; Lourido, S.; Bell, G. W.; Ingram, J. R.; Ploegh, H. L., One-Step Enzymatic Modification of the Cell Surface Redirects Cellular Cytotoxicity and Parasite Tropism. *ACS Chemical Biology* **2015,** *10* (2), 460-465.

49. Merzaban, J. S.; Imitola, J.; Starossom, S. C.; Zhu, B.; Wang, Y.; Lee, J.; Ali, A. J.; Olah, M.; Abuelela, A. F.; Khoury, S. J.; Sackstein, R., Cell surface glycan engineering of neural stem cells augments neurotropism and improves

recovery in a murine model of multiple sclerosis. *Glycobiology* **2015,** *25* (12), 1392-409.

50. Wang, Q.; Cheng, H.; Peng, H.; Zhou, H.; Li, P. Y.; Langer, R., Non-genetic engineering of cells for drug delivery and cell-based therapy. *Advanced Drug Delivery Reviews* **2015,** *91* (Supplement C), 125-140.

51. Luo, W.; Pulsipher, A.; Dutta, D.; Lamb, B. M.; Yousaf, M. N., Remote Control of Tissue Interactions via Engineered Photo-switchable Cell Surfaces. **2014,** *4*, 6313.

52. Pulsipher, A.; Dutta, D.; Luo, W.; Yousaf, M. N., Cell-surface engineering by a conjugation-and-release approach based on the formation and cleavage of oxime linkages upon mild electrochemical oxidation and reduction. *Angew Chem Int Ed Engl* **2014,** *53* (36), 9487-92.

53. Luo, W.; Westcott, N.; Dutta, D.; Pulsipher, A.; Rogozhnikov, D.; Chen, J.; Yousaf, M. N., A Dual Receptor and Reporter for Multi-Modal Cell Surface Engineering. *ACS Chem Biol* **2015,** *10* (10), 2219-26.

54. Ko, I. K.; Kim, B. G.; Awadallah, A.; Mikulan, J.; Lin, P.; Letterio, J. J.; Dennis, J. E., Targeting improves MSC treatment of inflammatory bowel disease. *Mol Ther* **2010,** *18* (7), 1365-72.

55. Allen, T. A.; Gracieux, D.; Talib, M.; Tokarz, D. A.; Hensley, M. T.; Cores, J.; Vandergriff, A.; Tang, J.; de Andrade, J. B.; Dinh, P. U.; Yoder, J. A.; Cheng, K., Angiopellosis as an Alternative Mechanism of Cell Extravasation. *Stem Cells* **2017,** *35* (1), 170-180.

56. Cheng, K.; Shen, D.; Xie, Y.; Cingolani, E.; Malliaras, K.; Marbán, E., Brief report: Mechanism of extravasation of infused stem cells. *Stem Cells* **2012,** *30* (12), 2835-42.

57. Paszek, M. J.; DuFort, C. C.; Rossier, O.; Bainer, R.; Mouw, J. K.; Godula, K.; Hudak, J. E.; Lakins, J. N.; Wijekoon, A. C.; Cassereau, L.; Rubashkin, M. G.; Magbanua, M. J.; Thorn, K. S.; Davidson, M. W.; Rugo, H. S.; Park, J. W.; Hammer, D. A.; Giannone, G.; Bertozzi, C. R.; Weaver, V. M., The cancer glycocalyx mechanically primes integrin-mediated growth and survival. *Nature* **2014,** *511* (7509), 319-25.

58. Woods, E. C.; Kai, F.; Barnes, J. M.; Pedram, K.; Pickup, M. W.; Hollander, M. J.; Weaver, V. M.; Bertozzi, C. R., A bulky glycocalyx fosters metastasis formation by promoting G1 cell cycle progression. *Elife* **2017,** *6*.

59. Jackson, H. J.; Rafiq, S.; Brentjens, R. J., Driving CAR T-cells forward. *Nat Rev Clin Oncol* **2016,** *13* (6), 370-83.

60. Palte, M. J.; Raines, R. T., Interaction of nucleic acids with the glycocalyx. *J Am Chem Soc* **2012,** *134* (14), 6218-23.

61. Weber, R. J.; Liang, S. I.; Selden, N. S.; Desai, T. A.; Gartner, Z. J., Efficient targeting of fatty-acid modified oligonucleotides to live cell membranes through stepwise assembly. *Biomacromolecules* **2014,** *15* (12), 4621-6.

62. Rabuka, D.; Forstner, M. B.; Groves, J. T.; Bertozzi, C. R., Noncovalent cell surface engineering: incorporation of bioactive synthetic glycopolymers into cellular membranes. *J Am Chem Soc* **2008,** *130* (18), 5947-53.

63. Woods, E. C.; Yee, N. A.; Shen, J.; Bertozzi, C. R., Glycocalyx Engineering with a Recycling Glycopolymer that Increases Cell Survival In Vivo. *Angew Chem Int Ed Engl* **2015,** *54* (52), 15782-8.

64. Rombouts, W. J.; Ploemacher, R. E., Primary murine MSC show highly efficient homing to the bone marrow but lose homing ability following culture. *Leukemia* **2003,** *17* (1), 160-70.

65. Dennis, J. E.; Cohen, N.; Goldberg, V. M.; Caplan, A. I., Targeted delivery of progenitor cells for cartilage repair. *J Orthop Res* **2004,** *22* (4), 735-41.

66. Du, J.; Yarema, K. J., Carbohydrate engineered cells for regenerative medicine. *Adv Drug Deliv Rev* **2010,** *62* (7-8), 671-82.

67. Carter, P. J.; Lazar, G. A., Next generation antibody drugs: pursuit of the 'high-hanging fruit'. *Nature Reviews Drug Discovery* **2017,** *17*, 197.

68. Binz, H. K.; Amstutz, P.; Pluckthun, A., Engineering novel binding proteins from nonimmunoglobulin domains. *Nat Biotech* **2005,** *23* (10), 1257-1268.

69. Banta, S.; Dooley, K.; Shur, O., Replacing antibodies: engineering new binding proteins. *Annu Rev Biomed Eng* **2013,** *15*, 93-113.

70. Skrlec, K.; Strukelj, B.; Berlec, A., Non-immunoglobulin scaffolds: a focus on their targets. *Trends Biotechnol* **2015,** *33* (7), 408-18.

71. Kruziki, M. A.; Bhatnagar, S.; Woldring, D. R.; Duong, V. T.; Hackel, B. J., A 45-Amino-Acid Scaffold Mined from the PDB for High-Affinity Ligand Engineering. *Chem Biol* **2015,** *22* (7), 946-56.

72. Smith, G. P., Filamentous fusion phage: novel expression vectors that display cloned antigens on the virion surface. *Science* **1985,** *228* (4705), 1315-7.

73. Hanes, J.; Pluckthun, A., In vitro selection and evolution of functional proteins by using ribosome display. *Proc Natl Acad Sci U S A* **1997,** *94* (10), 4937-42.

74. Roberts, R. W.; Szostak, J. W., RNA-peptide fusions for the in vitro selection of peptides and proteins. *Proc Natl Acad Sci U S A* **1997,** *94* (23), 12297-302.

75. Wentzel, A.; Christmann, A.; Adams, T.; Kolmar, H., Display of passenger proteins on the surface of Escherichia coli K-12 by the enterohemorrhagic E. coli intimin EaeA. *J Bacteriol* **2001,** *183* (24), 7273-84.

76. Chao, G.; Lau, W. L.; Hackel, B. J.; Sazinsky, S. L.; Lippow, S. M.; Wittrup, K. D., Isolating and engineering human antibodies using yeast surface display. *Nat Protoc* **2006,** *1* (2), 755-68.

77. Vazquez-Lombardi, R.; Phan, T. G.; Zimmermann, C.; Lowe, D.; Jermutus, L.; Christ, D., Challenges and opportunities for non-antibody scaffold drugs. *Drug Discov Today* **2015,** *20* (10), 1271-83.

78. Patriarca, C.; Macchi, R. M.; Marschner, A. K.; Mellstedt, H., Epithelial cell adhesion molecule expression (CD326) in cancer: a short review. *Cancer Treat Rev* **2012,** *38* (1), 68-75.

79. Balzar, M.; Prins, F. A.; Bakker, H. A.; Fleuren, G. J.; Warnaar, S. O.; Litvinov, S. V., The structural analysis of adhesions mediated by Ep-CAM. *Exp Cell Res* **1999,** *246* (1), 108-21.

80. Litvinov, S. V.; Velders, M. P.; Bakker, H. A.; Fleuren, G. J.; Warnaar, S. O., Ep-CAM: a human epithelial antigen is a homophilic cell-cell adhesion molecule. *J Cell Biol* **1994,** *125* (2), 437-46.

81. Litvinov, S. V.; Bakker, H. A.; Gourevitch, M. M.; Velders, M. P.; Warnaar, S. O., Evidence for a role of the epithelial glycoprotein 40 (Ep-CAM) in epithelial cell-cell adhesion. *Cell Adhes Commun* **1994,** *2* (5), 417-28.

82. Pavsic, M.; Guncar, G.; Djinovic-Carugo, K.; Lenarcic, B., Crystal structure and its bearing towards an understanding of key biological functions of EpCAM. *Nat Commun* **2014,** *5*, 4764.

83. Went, P. T.; Lugli, A.; Meier, S.; Bundi, M.; Mirlacher, M.; Sauter, G.; Dirnhofer, S., Frequent EpCam protein expression in human carcinomas. *Hum Pathol* **2004,** *35* (1), 122-8.

84. Baeuerle, P. A.; Gires, O., EpCAM (CD326) finding its role in cancer. *Br J Cancer* **2007,** *96* (3), 417-23.

85. Gires, O.; Klein, C. A.; Baeuerle, P. A., On the abundance of EpCAM on cancer stem cells. In *Nat Rev Cancer*, England, 2009; Vol. 9, p 143; author reply 143.

86. Munz, M.; Baeuerle, P. A.; Gires, O., The emerging role of EpCAM in cancer and stem cell signaling. *Cancer Res* **2009,** *69* (14), 5627-9.

87. Ruf, P.; Kluge, M.; Jager, M.; Burges, A.; Volovat, C.; Heiss, M. M.; Hess, J.; Wimberger, P.; Brandt, B.; Lindhofer, H., Pharmacokinetics, immunogenicity and bioactivity of the therapeutic antibody catumaxomab intraperitoneally administered to cancer patients. *Br J Clin Pharmacol* **2010,** *69* (6), 617-25.

88. Simon, M.; Stefan, N.; Pluckthun, A.; Zangemeister-Wittke, U., Epithelial cell adhesion molecule-targeted drug delivery for cancer therapy. *Expert Opin Drug Deliv* **2013,** *10* (4), 451-68.

89. Zielonka, S.; Weber, N.; Becker, S.; Doerner, A.; Christmann, A.; Christmann, C.; Uth, C.; Fritz, J.; Schafer, E.; Steinmann, B.; Empting, M.; Ockelmann, P.; Lierz, M.; Kolmar, H., Shark Attack: high affinity binding proteins derived from shark vNAR domains by stepwise in vitro affinity maturation. *J Biotechnol* **2014,** *191*, 236-45.

90. Zielonka, S.; Empting, M.; Konning, D.; Grzeschik, J.; Krah, S.; Becker, S.; Dickgiesser, S.; Kolmar, H., The Shark Strikes Twice: Hypervariable Loop 2 of Shark IgNAR Antibody Variable Domains and Its Potential to Function as an Autonomous Paratope. *Mar Biotechnol (NY)* **2015,** *17* (4), 386-92.

91. Martin-Killias, P.; Stefan, N.; Rothschild, S.; Pluckthun, A.; Zangemeister-Wittke, U., A novel fusion toxin derived from an EpCAM-specific designed ankyrin repeat protein has potent antitumor activity. *Clin Cancer Res* **2011,** *17* (1), 100-10.

92. Stefan, N.; Martin-Killias, P.; Wyss-Stoeckle, S.; Honegger, A.; Zangemeister-Wittke, U.; Pluckthun, A., DARPins recognizing the tumor-associated antigen

EpCAM selected by phage and ribosome display and engineered for multivalency. *J Mol Biol* **2011,** *413* (4), 826-43.

93. Iwasaki, K.; Goto, Y.; Katoh, T.; Yamashita, T.; Kaneko, S.; Suga, H., A Fluorescent Imaging Probe Based on a Macrocyclic Scaffold That Binds to Cellular EpCAM. *J Mol Evol* **2015,** *81* (5-6), 210-7.

94. Koide, A.; Bailey, C. W.; Huang, X.; Koide, S., The fibronectin type III domain as a scaffold for novel binding proteins. *J Mol Biol* **1998,** *284* (4), 1141-51.

95. Lipovsek, D., Adnectins: engineered target-binding protein therapeutics. *Protein Eng Des Sel* **2011,** *24* (1-2), 3-9.

96. Chen, T. F.; de Picciotto, S.; Hackel, B. J.; Wittrup, K. D., Engineering fibronectin-based binding proteins by yeast surface display. *Methods Enzymol* **2013,** *523*, 303-26.

97. Hackel, B. J.; Kapila, A.; Wittrup, K. D., Picomolar affinity fibronectin domains engineered utilizing loop length diversity, recursive mutagenesis, and loop shuffling. *J Mol Biol* **2008,** *381* (5), 1238-52.

98. Hackel, B. J.; Sathirachinda, A.; Gambhir, S. S., Designed hydrophilic and charge mutations of the fibronectin domain: towards tailored protein biodistribution. *Protein Eng Des Sel* **2012,** *25* (10), 639-47.

99. Hackel, B. J.; Neil, J. R.; White, F. M.; Wittrup, K. D., Epidermal growth factor receptor downregulation by small heterodimeric binding proteins. *Protein Eng Des Sel* **2012,** *25* (2), 47-57.

100. Woldring, D. R.; Holec, P. V.; Zhou, H.; Hackel, B. J., High-Throughput Ligand Discovery Reveals a Sitewise Gradient of Diversity in Broadly Evolved Hydrophilic Fibronectin Domains. *PLoS One* **2015,** *10* (9), e0138956.

101. Stern, L. A.; Schrack, I. A.; Johnson, S. M.; Deshpande, A.; Bennett, N. R.; Harasymiw, L. A.; Gardner, M. K.; Hackel, B. J., Geometry and expression

enhance enrichment of functional yeast-displayed ligands via cell panning. *Biotechnol Bioeng* **2016,** *113* (11), 2328-41.

102. Stern, L. A.; Csizmar, C. M.; Woldring, D. R.; Wagner, C. R.; Hackel, B. J., Titratable Avidity Reduction Enhances Affinity Discrimination in Mammalian Cellular Selections of Yeast-Displayed Ligands. *ACS Combinatorial Science* **2017,** *19* (5), 315-323.

103. Porebski, B. T.; Conroy, P. J.; Drinkwater, N.; Schofield, P.; Vazquez-Lombardi, R.; Hunter, M. R.; Hoke, D. E.; Christ, D.; McGowan, S.; Buckle, A. M., Circumventing the stability-function trade-off in an engineered FN3 domain. *Protein Eng Des Sel* **2016**.

104. Koide, A.; Wojcik, J.; Gilbreth, R. N.; Hoey, R. J.; Koide, S., Teaching an old scaffold new tricks: monobodies constructed using alternative surfaces of the FN3 scaffold. *J Mol Biol* **2012,** *415* (2), 393-405.

105. Tsuchikama, K.; An, Z., Antibody-drug conjugates: recent advances in conjugation and linker chemistries. *Protein Cell* **2018,** *9* (1), 33-46.

106. Ghanemi, M.; Pourshohod, A.; Ghaffari, M. A.; Kheirollah, A.; Amin, M.; Zeinali, M.; Jamalan, M., Specific targeting of HER2-positive head and neck squamous cell carcinoma line HN5 by Idarubicin-ZHER2 affibody conjugate. *Curr Cancer Drug Targets* **2017**.

107. Martins, C. D.; Da Pieve, C.; Burley, T. A.; Smith, R.; Ciobota, D. M.; Allott, L.; Harrington, K. J.; Oyen, W. J. G.; Smith, G.; Kramer-Marek, G., HER3-Mediated Resistance to Hsp90 Inhibition Detected in Breast Cancer Xenografts by Affibody-Based PET Imaging. *Clin Cancer Res* **2018,** *24* (8), 1853-1865.

108. Oroujeni, M.; Andersson, K. G.; Steinhardt, X.; Altai, M.; Orlova, A.; Mitran, B.; Vorobyeva, A.; Garousi, J.; Tolmachev, V.; Lofblom, J., Influence of composition

of cysteine-containing peptide-based chelators on biodistribution of (99m)Tc-labeled anti-EGFR affibody molecules. *Amino Acids* **2018**.

109. Sochaj-Gregorczyk, A. M.; Serwotka-Suszczak, A. M.; Otlewski, J., A Novel Affibody-Auristatin E Conjugate With a Potent and Selective Activity Against HER2+ Cell Lines. *J Immunother* **2016,** *39* (6), 223-32.

110. Mamluk, R.; Carvajal, I. M.; Morse, B. A.; Wong, H.; Abramowitz, J.; Aslanian, S.; Lim, A. C.; Gokemeijer, J.; Storek, M. J.; Lee, J.; Gosselin, M.; Wright, M. C.; Camphausen, R. T.; Wang, J.; Chen, Y.; Miller, K.; Sanders, K.; Short, S.; Sperinde, J.; Prasad, G.; Williams, S.; Kerbel, R.; Ebos, J.; Mutsaers, A.; Mendlein, J. D.; Harris, A. S.; Furfine, E. S., Anti-tumor effect of CT-322 as an adnectin inhibitor of vascular endothelial growth factor receptor-2. *MAbs* **2010,** *2* (2), 199-208.

111. Goldberg, S. D.; Cardoso, R. M.; Lin, T.; Spinka-Doms, T.; Klein, D.; Jacobs, S. A.; Dudkin, V.; Gilliland, G.; O'Neil, K. T., Engineering a targeted delivery platform using Centyrins. *Protein Eng Des Sel* **2016,** *29* (12), 563-572.

112. Stern, L. A.; Case, B. A.; Hackel, B. J., Alternative Non-Antibody Protein Scaffolds for Molecular Imaging of Cancer. *Curr Opin Chem Eng* **2013,** *2* (4).

113. Schjoeth-Eskesen, C.; Nielsen, C. H.; Heissel, S.; Hojrup, P.; Hansen, P. R.; Gillings, N.; Kjaer, A., [(64) Cu]-labelled trastuzumab: optimisation of labelling by DOTA and NODAGA conjugation and initial evaluation in mice. *J Labelled Comp Radiopharm* **2015,** *58* (6), 227-33.

114. Ghosh, S. C.; Pinkston, K. L.; Robinson, H.; Harvey, B. R.; Wilganowski, N.; Gore, K.; Sevick-Muraca, E. M.; Azhdarinia, A., Comparison of DOTA and NODAGA as chelators for (64)Cu-labeled immunoconjugates. *Nucl Med Biol* **2015,** *42* (2), 177-83.

115. Yona, S.; Gordon, S., From the Reticuloendothelial to Mononuclear Phagocyte System - The Unaccounted Years. *Front Immunol* **2015,** *6*, 328.

116. Lim, K. H.; Huang, H.; Pralle, A.; Park, S., Stable, high-affinity streptavidin monomer for protein labeling and monovalent biotin detection. *Biotechnol Bioeng* **2013,** *110* (1), 57-67.

117. Schlapschy, M.; Binder, U.; Borger, C.; Theobald, I.; Wachinger, K.; Kisling, S.; Haller, D.; Skerra, A., PASylation: a biological alternative to PEGylation for extending the plasma half-life of pharmaceutically active proteins. *Protein Eng Des Sel* **2013,** *26* (8), 489-501.

118. Feldhaus, M. J.; Siegel, R. W.; Opresko, L. K.; Coleman, J. R.; Feldhaus, J. M.; Yeung, Y. A.; Cochran, J. R.; Heinzelman, P.; Colby, D.; Swers, J.; Graff, C.; Wiley, H. S.; Wittrup, K. D., Flow-cytometric isolation of human antibodies from a nonimmune Saccharomyces cerevisiae surface display library. *Nat Biotechnol* **2003,** *21* (2), 163-70.

119. Zaccolo, M.; Williams, D. M.; Brown, D. M.; Gherardi, E., An approach to random mutagenesis of DNA using mixtures of triphosphate derivatives of nucleoside analogues. *J Mol Biol* **1996,** *255* (4), 589-603.

120. Kruziki, M. A.; Case, B. A.; Chan, J. Y.; Zudock, E. J.; Woldring, D. R.; Yee, D.; Hackel, B. J., (64)Cu-Labeled Gp2 Domain for PET Imaging of Epidermal Growth Factor Receptor. *Mol Pharm* **2016,** *13* (11), 3747-3755.

121. Sadelain, M.; Rivière, I.; Riddell, S., Therapeutic T cell engineering. *Nature* **2017,** *545*, 423.

122. Fesnak, A. D.; June, C. H.; Levine, B. L., Engineered T cells: the promise and challenges of cancer immunotherapy. *Nat Rev Cancer* **2016,** *16* (9), 566-81.

123. Nowakowski, A.; Andrzejewska, A.; Janowski, M.; Walczak, P.; Lukomska, B., Genetic engineering of stem cells for enhanced therapy. *Acta Neurobiol Exp (Wars)* **2013,** *73* (1), 1-18.

124. Maude, S. L.; Frey, N.; Shaw, P. A.; Aplenc, R.; Barrett, D. M.; Bunin, N. J.; Chew, A.; Gonzalez, V. E.; Zheng, Z.; Lacey, S. F.; Mahnke, Y. D.; Melenhorst, J. J.; Rheingold, S. R.; Shen, A.; Teachey, D. T.; Levine, B. L.; June, C. H.; Porter, D. L.; Grupp, S. A., Chimeric Antigen Receptor T Cells for Sustained Remissions in Leukemia. *New England Journal of Medicine* **2014,** *371* (16), 1507-1517.

125. Lamers, C. H.; Sleijfer, S.; van Steenbergen, S.; van Elzakker, P.; van Krimpen, B.; Groot, C.; Vulto, A.; den Bakker, M.; Oosterwijk, E.; Debets, R.; Gratama, J. W., Treatment of metastatic renal cell carcinoma with CAIX CAR-engineered T cells: clinical evaluation and management of on-target toxicity. *Mol Ther* **2013,** *21* (4), 904-12.

126. Gust, J.; Hay, K. A.; Hanafi, L. A.; Li, D.; Myerson, D.; Gonzalez-Cuyar, L. F.; Yeung, C.; Liles, W. C.; Wurfel, M.; Lopez, J. A.; Chen, J.; Chung, D.; Harju-Baker, S.; Ozpolat, T.; Fink, K. R.; Riddell, S. R.; Maloney, D. G.; Turtle, C. J., Endothelial Activation and Blood-Brain Barrier Disruption in Neurotoxicity after Adoptive Immunotherapy with CD19 CAR-T Cells. *Cancer Discov* **2017**.

127. Carlson, J. C. T.; Jena, S. S.; Flenniken, M.; Chou, T.-f.; Siegel, R. A.; Wagner, C. R., Chemically Controlled Self-Assembly of Protein Nanorings. *Journal of the American Chemical Society* **2006,** *128* (23), 7630-7638.

128. Li, Q.; So, C. R.; Fegan, A.; Cody, V.; Sarikaya, M.; Vallera, D. A.; Wagner, C. R., Chemically Self-Assembled Antibody Nanorings (CSANs): Design and Characterization of an Anti-CD3 IgM Biomimetic. *Journal of the American Chemical Society* **2010,** *132* (48), 17247-17257.

129. Shah, R.; Petersburg, J.; Gangar, A. C.; Fegan, A.; Wagner, C. R.; Kumarapperuma, S. C., In Vivo Evaluation of Site-Specifically PEGylated Chemically Self-Assembled Protein Nanostructures. *Mol Pharm* **2016,** *13* (7), 2193-203.

130. Fegan, A.; Kumarapperuma, S. C.; Wagner, C. R., Chemically Self-Assembled Antibody Nanostructures as Potential Drug Carriers. *Molecular Pharmaceutics* **2012,** *9* (11), 3218-3227.

131. Shen, J.; Vallera, D. A.; Wagner, C. R., Prosthetic Antigen Receptors. *J Am Chem Soc* **2015,** *137* (32), 10108-11.

132. Srisa-Art, M.; Dyson, E. C.; deMello, A. J.; Edel, J. B., Monitoring of Real-Time Streptavidin−Biotin Binding Kinetics Using Droplet Microfluidics. *Analytical Chemistry* **2008,** *80* (18), 7063-7067.

133. Karver, M. R.; Weissleder, R.; Hilderbrand, S. A., Bioorthogonal Reaction Pairs Enable Simultaneous, Selective, Multi-Target Imaging. *Angewandte Chemie (International ed. in English)* **2012,** *51* (4), 920-922.

134. Eatman, F. B.; Maggio, A. C.; Pocelinko, R.; Boxenbaum, H. G.; Geitner, K. A.; Glover, W.; Macasieb, T.; Holazo, A.; Weinfeld, R. E.; Kaplan, S. A., Blood and salivary concentrations of sulfamethoxazole and trimethoprim in man. *Journal of Pharmacokinetics and Biopharmaceutics* **1977,** *5* (6), 615-624.

135. Watson, I. D.; Stewart, M. J., Trimethoprim: Prediction of serum concentrations from saliva measurements. *European Journal of Clinical Pharmacology* **1986,** *30* (4), 457-461.

136. Li, Q.; Hapka, D.; Chen, H.; Vallera, D. A.; Wagner, C. R., Self-assembly of antibodies by chemical induction. *Angew Chem Int Ed Engl* **2008,** *47* (52), 10179-82.

137. Maude, S. L.; Laetsch, T. W.; Buechner, J.; Rives, S.; Boyer, M.; Bittencourt, H.; Bader, P.; Verneris, M. R.; Stefanski, H. E.; Myers, G. D.; Qayed, M.; De Moerloose, B.; Hiramatsu, H.; Schlis, K.; Davis, K. L.; Martin, P. L.; Nemecek, E. R.; Yanik, G. A.; Peters, C.; Baruchel, A.; Boissel, N.; Mechinaud, F.; Balduzzi, A.; Krueger, J.; June, C. H.; Levine, B. L.; Wood, P.; Taran, T.; Leung, M.; Mueller, K. T.; Zhang, Y.; Sen, K.; Lebwohl, D.; Pulsipher, M. A.; Grupp, S. A., Tisagenlecleucel in Children and Young Adults with B-Cell Lymphoblastic Leukemia. *N Engl J Med* **2018,** *378* (5), 439-448.

138. Morgan, R. A.; Yang, J. C.; Kitano, M.; Dudley, M. E.; Laurencot, C. M.; Rosenberg, S. A., Case report of a serious adverse event following the administration of T cells transduced with a chimeric antigen receptor recognizing ERBB2. *Mol Ther* **2010,** *18* (4), 843-51.

139. Parkhurst, M. R.; Yang, J. C.; Langan, R. C.; Dudley, M. E.; Nathan, D. A.; Feldman, S. A.; Davis, J. L.; Morgan, R. A.; Merino, M. J.; Sherry, R. M.; Hughes, M. S.; Kammula, U. S.; Phan, G. Q.; Lim, R. M.; Wank, S. A.; Restifo, N. P.; Robbins, P. F.; Laurencot, C. M.; Rosenberg, S. A., T cells targeting carcinoembryonic antigen can mediate regression of metastatic colorectal cancer but induce severe transient colitis. *Mol Ther* **2011,** *19* (3), 620-6.

140. Fiedler, W. M.; Wolf, M.; Kebenko, M.; Goebeler, M.-E.; Ritter, B.; Quaas, A.; Vieser, E.; Hijazi, Y.; Patzak, I.; Friedrich, M.; Kufer, P.; Frankel, S.; Seggewiss-Bernhardt, R.; Kaubitzsch, S., A phase I study of EpCAM/CD3-bispecific antibody (MT110) in patients with advanced solid tumors. *Journal of Clinical Oncology* **2012,** *30* (15_suppl), 2504-2504.

141. Klinger, M.; Benjamin, J.; Kischel, R.; Stienen, S.; Zugmaier, G., Harnessing T cells to fight cancer with BiTE(R) antibody constructs--past developments and future directions. *Immunol Rev* **2016,** *270* (1), 193-208.

142. Seimetz, D.; Lindhofer, H.; Bokemeyer, C., Development and approval of the trifunctional antibody catumaxomab (anti-EpCAM x anti-CD3) as a targeted cancer immunotherapy. *Cancer Treat Rev* **2010,** *36* (6), 458-67.

143. Mau-Sorensen, M.; Dittrich, C.; Dienstmann, R.; Lassen, U.; Buchler, W.; Martinius, H.; Tabernero, J., A phase I trial of intravenous catumaxomab: a bispecific monoclonal antibody targeting EpCAM and the T cell coreceptor CD3. *Cancer Chemother Pharmacol* **2015,** *75* (5), 1065-73.

144. Caruso, H. G.; Hurton, L. V.; Najjar, A.; Rushworth, D.; Ang, S.; Olivares, S.; Mi, T.; Switzer, K.; Singh, H.; Huls, H.; Lee, D. A.; Heimberger, A. B.; Champlin, R. E.; Cooper, L. J., Tuning Sensitivity of CAR to EGFR Density Limits Recognition of Normal Tissue While Maintaining Potent Antitumor Activity. *Cancer Res* **2015,** *75* (17), 3505-18.

145. Liu, X.; Jiang, S.; Fang, C.; Yang, S.; Olalere, D.; Pequignot, E. C.; Cogdill, A. P.; Li, N.; Ramones, M.; Granda, B.; Zhou, L.; Loew, A.; Young, R. M.; June, C. H.; Zhao, Y., Affinity-Tuned ErbB2 or EGFR Chimeric Antigen Receptor T Cells Exhibit an Increased Therapeutic Index against Tumors in Mice. *Cancer Res* **2015,** *75* (17), 3596-607.

146. Park, S.; Shevlin, E.; Vedvyas, Y.; Zaman, M.; Hsu, Y. S.; Min, I. M.; Jin, M. M., Micromolar affinity CAR T cells to ICAM-1 achieves rapid tumor elimination while avoiding systemic toxicity. *Sci Rep* **2017,** *7* (1), 14366.

147. Drent, E.; Themeli, M.; Poels, R.; de Jong-Korlaar, R.; Yuan, H.; de Bruijn, J.; Martens, A. C. M.; Zweegman, S.; van de Donk, N.; Groen, R. W. J.; Lokhorst, H. M.; Mutis, T., A Rational Strategy for Reducing On-Target Off-Tumor Effects

of CD38-Chimeric Antigen Receptors by Affinity Optimization. *Mol Ther* **2017,** *25* (8), 1946-1958.

148. Arcangeli, S.; Rotiroti, M. C.; Bardelli, M.; Simonelli, L.; Magnani, C. F.; Biondi, A.; Biagi, E.; Tettamanti, S.; Varani, L., Balance of Anti-CD123 Chimeric Antigen Receptor Binding Affinity and Density for the Targeting of Acute Myeloid Leukemia. *Mol Ther* **2017,** *25* (8), 1933-1945.

149. Calderon, A. J.; Bhowmick, T.; Leferovich, J.; Burman, B.; Pichette, B.; Muzykantov, V.; Eckmann, D. M.; Muro, S., Optimizing endothelial targeting by modulating the antibody density and particle concentration of anti-ICAM coated carriers. *J Control Release* **2011,** *150* (1), 37-44.

150. Zern, B. J.; Chacko, A. M.; Liu, J.; Greineder, C. F.; Blankemeyer, E. R.; Radhakrishnan, R.; Muzykantov, V., Reduction of nanoparticle avidity enhances the selectivity of vascular targeting and PET detection of pulmonary inflammation. *ACS Nano* **2013,** *7* (3), 2461-9.

151. Aires, A.; Cadenas, J. F.; Guantes, R.; Cortajarena, A. L., An experimental and computational framework for engineering multifunctional nanoparticles: designing selective anticancer therapies. *Nanoscale* **2017,** *9* (36), 13760-13771.

152. Hong, S.; Leroueil, P. R.; Majoros, I. J.; Orr, B. G.; Baker, J. R., Jr.; Banaszak Holl, M. M., The binding avidity of a nanoparticle-based multivalent targeted drug delivery platform. *Chem Biol* **2007,** *14* (1), 107-15.

153. Silpe, J. E.; Sumit, M.; Thomas, T. P.; Huang, B.; Kotlyar, A.; van Dongen, M. A.; Banaszak Holl, M. M.; Orr, B. G.; Choi, S. K., Avidity modulation of folate-targeted multivalent dendrimers for evaluating biophysical models of cancer targeting nanoparticles. *ACS Chem Biol* **2013,** *8* (9), 2063-71.

154. van Dongen, M. A.; Silpe, J. E.; Dougherty, C. A.; Kanduluru, A. K.; Choi, S. K.; Orr, B. G.; Low, P. S.; Banaszak Holl, M. M., Avidity mechanism of dendrimer-folic acid conjugates. *Mol Pharm* **2014,** *11* (5), 1696-706.

155. Huskens, J.; Mulder, A.; Auletta, T.; Nijhuis, C. A.; Ludden, M. J.; Reinhoudt, D. N., A model for describing the thermodynamics of multivalent host-guest interactions at interfaces. *J Am Chem Soc* **2004,** *126* (21), 6784-97.

156. Martinez-Veracoechea, F. J.; Frenkel, D., Designing super selectivity in multivalent nano-particle binding. *Proc Natl Acad Sci U S A* **2011,** *108* (27), 10963-8.

157. Rhoden, J. J.; Dyas, G. L.; Wroblewski, V. J., A Modeling and Experimental Investigation of the Effects of Antigen Density, Binding Affinity, and Antigen Expression Ratio on Bispecific Antibody Binding to Cell Surface Targets. *J Biol Chem* **2016,** *291* (21), 11337-47.

158. De Michele, C.; De Los Rios, P.; Foffi, G.; Piazza, F., Simulation and Theory of Antibody Binding to Crowded Antigen-Covered Surfaces. *PLoS Comput Biol* **2016,** *12* (3), e1004752.

159. Curk, T.; Dobnikar, J.; Frenkel, D., Optimal multivalent targeting of membranes with many distinct receptors. *Proc Natl Acad Sci U S A* **2017,** *114* (28), 7210-7215.

160. Dubacheva, G. V.; Curk, T.; Mognetti, B. M.; Auzely-Velty, R.; Frenkel, D.; Richter, R. P., Superselective targeting using multivalent polymers. *J Am Chem Soc* **2014,** *136* (5), 1722-5.

161. Dubacheva, G. V.; Curk, T.; Auzely-Velty, R.; Frenkel, D.; Richter, R. P., Designing multivalent probes for tunable superselective targeting. *Proc Natl Acad Sci U S A* **2015,** *112* (18), 5579-84.

162. Hadzhieva, M.; Pashov, A. D.; Kaveri, S.; Lacroix-Desmazes, S.; Mouquet, H.; Dimitrov, J. D., Impact of Antigen Density on the Binding Mechanism of IgG Antibodies. *Sci Rep* **2017,** *7* (1), 3767.

163. Mazor, Y.; Oganesyan, V.; Yang, C.; Hansen, A.; Wang, J.; Liu, H.; Sachsenmeier, K.; Carlson, M.; Gadre, D. V.; Borrok, M. J.; Yu, X. Q.; Dall'Acqua, W.; Wu, H.; Chowdhury, P. S., Improving target cell specificity using a novel monovalent bispecific IgG design. *MAbs* **2015,** *7* (2), 377-89.

164. Mazor, Y.; Hansen, A.; Yang, C.; Chowdhury, P. S.; Wang, J.; Stephens, G.; Wu, H.; Dall'Acqua, W. F., Insights into the molecular basis of a bispecific antibody's target selectivity. *MAbs* **2015,** *7* (3), 461-9.

165. Mazor, Y.; Sachsenmeier, K. F.; Yang, C.; Hansen, A.; Filderman, J.; Mulgrew, K.; Wu, H.; Dall'Acqua, W. F., Enhanced tumor-targeting selectivity by modulating bispecific antibody binding affinity and format valence. *Sci Rep* **2017,** *7*, 40098.

166. Petersburg, J.; Shen, J.; Csizmar, C. M.; Murphy, K. A.; Spanier, J.; Gabrielse, K.; Griffith, T. S.; Fife, B.; Wagner, C. R., Eradication of Established Tumors by Chemically Self-Assembled Nanoring (CSAN) Targeted T-cells. *ACS Nano* **2018**.

167. Mammen, M.; Choi, S. K.; Whitesides, G. M., Polyvalent Interactions in Biological Systems: Implications for Design and Use of Multivalent Ligands and Inhibitors. *Angew Chem Int Ed Engl* **1998,** *37* (20), 2754-2794.

168. Jencks, W. P., On the attribution and additivity of binding energies. *Proc Natl Acad Sci U S A* **1981,** *78* (7), 4046-50.

169. Kaufman, E. N.; Jain, R. K., Effect of bivalent interaction upon apparent antibody affinity: experimental confirmation of theory using fluorescence photobleaching

and implications for antibody binding assays. *Cancer Res* **1992,** *52* (15), 4157-67.

170. Friedman, M.; Orlova, A.; Johansson, E.; Eriksson, T. L.; Hoiden-Guthenberg, I.; Tolmachev, V.; Nilsson, F. Y.; Stahl, S., Directed evolution to low nanomolar affinity of a tumor-targeting epidermal growth factor receptor-binding affibody molecule. *J Mol Biol* **2008,** *376* (5), 1388-402.

171. Tolmachev, V.; Tran, T. A.; Rosik, D.; Sjoberg, A.; Abrahmsen, L.; Orlova, A., Tumor targeting using affibody molecules: interplay of affinity, target expression level, and binding site composition. *J Nucl Med* **2012,** *53* (6), 953-60.

172. Hackel, B. J.; Kimura, R. H.; Gambhir, S. S., Use of (64)Cu-labeled fibronectin domain with EGFR-overexpressing tumor xenograft: molecular imaging. *Radiology* **2012,** *263* (1), 179-88.

173. Zahnd, C.; Kawe, M.; Stumpp, M. T.; de Pasquale, C.; Tamaskovic, R.; Nagy-Davidescu, G.; Dreier, B.; Schibli, R.; Binz, H. K.; Waibel, R.; Pluckthun, A., Efficient tumor targeting with high-affinity designed ankyrin repeat proteins: effects of affinity and molecular size. *Cancer Res* **2010,** *70* (4), 1595-605.

174. Sulzer, B.; Perelson, A. S., Equilibrium binding of multivalent ligands to cells: effects of cell and receptor density. *Math Biosci* **1996,** *135* (2), 147-85.

APPENDIX 1

Fusion Protein Sequences

Chapter III

DHFR^2-Fn3 *(467 amino acids; calculated MW 51.0kDa)*

MGEQKLISEEDLGGSGGGSGGGISLIAALAVDRVIGMENAMPWNLPADLAWFKRNTLN
KPVIMGRHTWESIGRPLPGRKNIILSSQPGTDDRVTWVKSVDEAIAAAGDVPEIMVIGG
GRVYEQFLPKAQKLYLTHIDAEVEGDTHFPDYEPDDWESVFSEFHDADAQNSHSYSFE
ILERRGGISLIAALAVDRVIGMENAMPWNLPADLAWFKRNTLNKPVIMGRHTWESIGRP
LPGRKNIILSSQPGTDDRVTWVKSVDEAIAAAGDVPEIMVIGGGRVYEQFLPKAQKLYLT
HIDAEVEGDTHFPDYEPDDWESVFSEFHDADAQNSHSYSFEILERRGELGGGGSGGG
GSGGGGSASSSDSPRNLEVTNATPNSLTISWDNSNYASYYRITYGETGGNSPSQELTV
PGSTYNATISGLKPGQDYIITVYAVTYRDNYSYSNLISINYRSEIDKPSQGSHHHHHH

mSA-DHFR^2 *(471 amino acids; calculated MW 51.4 kDa)*

MAEAGITGTWYNQSGSTFTVTAGADGNLTGQYENRAQGTGCQNSPYTLTGRYNGTKL
EWRVEWNNSTENCHSRTEWRGQYQGGAEARINTQWNLTYEGGSGPATEQGQDTFT
KVKELGGSGGGSGGGSGGMISLIAALAVDRVIGMENAMPWNLPADLAWFKRNTLNKP
VIMGRHTWESIGRPLPGRKNIILSSQPGTDDRVTWVKSVDEAIAAAGDVPEIMVIGGGR
VYEQFLPKAQKLYLTHIDAEVEGDTHFPDYEPDDWESVFSEFHDADAQNSHSYSFEILE
RRGMISLIAALAVDRVIGMENAMPWNLPADLAWFKRNTLNKPVIMGRHTWESIGRPLP
GRKNIILSSQPGTDDRVTWVKSVDEAIAAAGDVPEIMVIGGGRVYEQFLPKAQKLYLTHI
DAEVEGDTHFPDYEPDDWESVFSEFHDADAQNSHSYSFEILERRGGSGGGSGGGSG
GDYKDDDDK

Chapter IV

DHFR^2-Fn3 (C5) *(497 amino acids; calculated MW 52.9 kDa)*

MGEQKLISEEDLGGSGGGSGGGISLIAALAVDRVIGMENAMPWNLPADLAWFKRNTLN
KPVIMGRHTWESIGRPLPGRKNIILSSQPGTDDRVTWVKSVDEAIAAAGDVPEIMVIGG
GRVYEQFLPKAQKLYLTHIDAEVEGDTHFPDYEPDDWESVFSEFHDADAQNSHSYSFE
ILERRGGISLIAALAVDRVIGMENAMPWNLPADLAWFKRNTLNKPVIMGRHTWESIGRP
LPGRKNIILSSQPGTDDRVTWVKSVDEAIAAAGDVPEIMVIGGGRVYEQFLPKAQKLYLT
HIDAEVEGDTHFPDYEPDDWESVFSEFHDADAQNSHSYSFEILERRGELGGSGGGGS
GGGGSGGGGSGGGGSGGGGSGGGGSGGGGSGGGGSGGASSSDSPRNLEVTNAT
PNSLTISWDNSNYASYYRITYGETGGNSPSQELTVPGSTYNATISGLKPGQDYIITVYAV
TYRDNYSYSNLISINYRSEIDKPSQGSHHHHHH

DHFR^2-Fn3 (B22) *497 amino acids; calculated MW 53.0 kDa)*

MGEQKLISEEDLGGSGGGSGGGISLIAALAVDRVIGMENAMPWNLPADLAWFKRNTLN
KPVIMGRHTWESIGRPLPGRKNIILSSQPGTDDRVTWVKSVDEAIAAAGDVPEIMVIGG
GRVYEQFLPKAQKLYLTHIDAEVEGDTHFPDYEPDDWESVFSEFHDADAQNSHSYSFE
ILERRGGISLIAALAVDRVIGMENAMPWNLPADLAWFKRNTLNKPVIMGRHTWESIGRP
LPGRKNIILSSQPGTDDRVTWVKSVDEAIAAAGDVPEIMVIGGGRVYEQFLPKAQKLYLT
HIDAEVEGDTHFPDYEPDDWESVFSEFHDADAQNSHSYSFEILERRGELGGSGGGGS
GGGGSGGGGSGGGGSGGGGSGGGGSGGGGSGGGGSGGASSSDSPRNLEVTNAT
PNSLTISWDDYTSASYYRITYGETGGNSPSQEFTVPGNTYNATVSGLRPGQDYIITVYA
VTYRDNYSYSNPISINYRTEIDKPSQGSHHHHHH

DHFR^2-Fn3 (NT) *(499 amino acids; calculated MW 52.7 kDa)*

MGEQKLISEEDLGGSGGGSGGGISLIAALAVDRVIGMENAMPWNLPADLAWFKRNTLN
KPVIMGRHTWESIGRPLPGRKNIILSSQPGTDDRVTWVKSVDEAIAAAGDVPEIMVIGG

GRVYEQFLPKAQKLYLTHIDAEVEGDTHFPDYEPDDWESVFSEFHDADAQNSHSYSFE

ILERRGGISLIAALAVDRVIGMENAMPWNLPADLAWFKRNTLNKPVIMGRHTWESIGRP

LPGRKNIILSSQPGTDDRVTWVKSVDEAIAAAGDVPEIMVIGGGRVYEQFLPKAQKLYLT

HIDAEVEGDTHFPDYEPDDWESVFSEFHDADAQNSHSYSFEILERRGELGGSGGGGS

GGGGSGGGGSGGGGSGGGGSGGGGSGGGGSGGGGSGGASSSDSPRNLEVTNAT

PNSLTISWDAPAVTVRYYRITYGETGGNSPSQEFTVPGSKSTATISGLKPGQDYTITVYA

VTGRDGSPASSKPISINYRTEIDKPSQGSHHHHHH